Master's thesis

NTNU
Norwegian University of Science and Technology
Faculty of Information Technology and Electrical Engineering
Department of Engineering Cybernetics

Brede Severin Paulsen

State-space modelling and small-signal analysis of a hybrid ships AC distributed power system with a Virtual Synchronous Machine

Master's thesis in Cybernetics and Robotics
Supervisor: Jon Are Wold Suul
July 2021

NTNU
Norwegian University of Science and Technology

Brede Severin Paulsen

State-space modelling and small-signal analysis of a hybrid ships AC distributed power system with a Virtual Synchronous Machine

Master's thesis in Cybernetics and Robotics
Supervisor: Jon Are Wold Suul
July 2021

Norwegian University of Science and Technology
Faculty of Information Technology and Electrical Engineering
Department of Engineering Cybernetics

NTNU
Norwegian University of
Science and Technology

Summary

The virtual synchronous machine (VSM) has been developed as an approach to provide flexible control of power electronic converters with energy storage systems (ESSs) to power systems. By providing ancillary services of the synchronous machine (SM), it can support power system operation and transition seamlessly between grid-connected and islanded operation. In this thesis, an analytical study of a hybrid ship power system using a VSM for power control has been conducted. Small-signal modeling and analysis with the support of an electrical simulation have been used for the analytical study of the power system.

Ship hybrid architecture has shown the capabilities of reducing emissions and fuel consumption by up to 30% to 50%. Load leveling, peak shaving, spinning reserve, zero-emission operation, and strategic loading are all operating modes that can contribute to the reduction of fuel consumption. The VSM in conjunction with an ESS can provide the benefits of the hybrid architecture and at the same time provide flexible distributed control of power electronic converter, by imitating the behavior of the SM.

In general, the applied approach based on linearization has proven to be very effective for assessing of the stability of the system. For small perturbations, the linearized state-space representation closely matches the electrical model that includes the non-linearities of the system. The presented numerical results verified the small-signal stability over the entire designated operating range of the system. Through parametric sweep analysis it has been observed that the placement of the system's critical modes can be affected by increasing the virtual inertia constant, T_a, and the damping coefficient $k_{d,vsm}$. A more desirable frequency response for the system has been achieved by increasing the initial values of the mentioned parameters.

Sammendrag

Den virtuelle synkronmaskinen er utviklet som en tilnærming for å gi fleksibel kontroll av omformere for energilagringssystemer koblet til kraftsystemer. Ved å etterligne driftstjenestene som en synkronmaskinen kan tilby, kan den virtuelle synkronmaskinene støtte driften av et kraftsystemet, samt bytte sømløst mellom nettilkobling og øydrift. I denne oppgaven er det gjennomført et analytiskstudie av et hybrid skipskraftsystem ved bruk av en virtuell synkronmaskin implantasjon for kraftkontroll. Små signal modellering og analyse med støtte fra en elektrisk simulering har blitt brukt til de analytiske studien av kraftsystemet.

Hybridarkitektur i skip har vist mulighetene for å redusere utslipp og drivstofforbruk med opptil 30% til 50%. Lastutjevning, toppbarbering, sentrifugeringsreserve, nullutslippsdrift og strategisk belastning er alle driftsmåter som kan bidra til redusert drivstofforbruk i skip. Bruk av en virtuell synkronmaskin koblet til et energilagringssystem kan gi de nevnte fordelene til hybridarkitekturen, samt gi en fleksibel distribuert kontroll av den kraftelektronisk omformer ved å imitere oppførselen til en synkronmaskin.

Tilnærmingen av kraftsystemet har vært basert på linearisering, og har vist seg å være svært effektiv for å vurdere systemets stabilitet. For små forstyrrelser samsvarer den lineariserte tilstands-romrepresentasjonen tett med den elektriske modellen som inkluderer systemets ulinearіteter. De presenterte numeriske resultatene bekreftet stabiliteten for små signal-modellen over hele det angitte driftsområdet til systemet. Gjennom parametrisk følsomhet er det observert at plasseringen av systemets kritiske egenverdier kan påvirkes ved å øke den virtuelle treghetskonstanten, T_a, og dempningskoeffisienten $k_{d,vsm}$. En mer ønskelig frekvensrespons for systemet er oppnådd ved å øke initialverdiene til de nevnte parameterne.

Preface

This report represents my master thesis for the degree of Master of Science in Cybernetics and Robotics at The Norwegian University of Science and Technology (NTNU). The thesis is a part of the specialization program in Energy and Process Cybernetics. The groundwork for this thesis was done in my specialization project during the autumn semester of 2020, while the work for this thesis was carried out during the spring semester of 2021.

The basis for this thesis originated from my interest in power electronics, power system analysis, and sustainability. The proposal for the specialization project was from my supervisor and together have formed the objective of the master thesis to what it is today.

It has been a challenge to complete this thesis, but at the same time, I have learned a lot during the work. I would not have been able to complete this thesis without the help of my supervisor, Associate Professor Jon Are Wold Suul. Thank you for your support. I would also like to thank my parents for all their support during my five years at NTNU.

Contents

List of Figures

List of Tables

Nomenclature

$\mathbf{A}_{load}$	Active load state-space model state matrix
$\mathbf{A}_{sm}$	Synchronous machine state-space model state matrix
$\mathbf{A}_{sys}$	Hybrid ship power system state-space model state matrix
$\mathbf{A}_{vsm}$	Virtual synchronous machine state-space model state matrix
$\mathbf{B}_{load}$	Active load state-space model input matrix
$\mathbf{B}_{sm}$	Synchronous machine state-space model input matrix
$\mathbf{B}_{sys}$	Hybrid ship power system state-space model input matrix
$\mathbf{B}_{vsm}$	Virtual synchronous machine state-space model input matrix
d-axis	Direct axis
q-axis	Quadrature axis
c_f	Per unit filter capacitance
c_l	Per unit static load capacitance
AC	Alternating current
AVR	Automtaic voltage regulator
BESS	Battery energy storage system
DC	Direct current
ESS	Energy storage system
$\mathbf{\Delta u}_{load}$	Active load small-signal state-space model input vector
$\mathbf{\Delta u}_{sm}$	Synchronous machine small-signal state-space model input vector
$\mathbf{\Delta u}_{sys}$	Hybrid ship power system small-signal state-space model input vector

$\mathbf{\Delta u}_{vsm}$ Virtual synchronous machine small-signal state-space model input vector

$\mathbf{\Delta x}_{load}$ Active load small-signal state-space model state vector

$\mathbf{\Delta x}_{sm}$ Synchronous machine small-signal state-space model state vector

$\mathbf{\Delta x}_{sys}$ Hybrid ship power system small-signal state-space model state vector

$\mathbf{\Delta x}_{vsm}$ Virtual synchronous machine small-signal state-space model state vector

$\delta\theta_{pll,load}$ Active load machine phase locked loop phase displacement

$\delta\theta_{pll,vsm}$ Virtual synchronous machine phase locked loop phase displacement

$\delta\theta_{sm}$ Synchronous machine rotor phase displacement

$\delta\theta_{vsm}$ Virtual synchronous machine virtual internal voltage phase displacement

$\delta\omega_{pll,vsm}$ Virtual synchronous machine phase locked loop speed deviation

$\varepsilon_{pll,load}$ Active load per unit phase locked loop controller integrator state

$\varepsilon_{pll,vsm}$ Virtual synchronous machine per unit phase locked loop controller integrator state

$\boldsymbol{\gamma}_{load}$ Active load per unit current controller integrate states

$\boldsymbol{\gamma}_{vsm}$ Virtual synchronous machine per unit current controller integrate states

i_{1d} Synchronous machine per unit first direct axis damper circuit current

i_{1q} Synchronous machine per unit first quadrature axis damper circuit current

$\mathbf{i}_{cv,load}$ Active load per unit filter inductors current

$\mathbf{i}_{cv,vsm}$ Virtual synchronous machine per unit filter inductors current

$\mathbf{i}^*_{cv,load}$ Active load per unit current controller reference

$\mathbf{i}^*_{cv,vsm}$ Virtual synchronous machine per unit current controller reference

i_{fd} Synchronous machine per unit field circuit current

$\mathbf{i}_{o,load}$ Active load per unit filter currents into the grid

$\mathbf{i}_{o,vsm}$ Virtual synchronous machine per unit filter currents into the grid

$\mathbf{i}_{sm}$ Synchronous machine per unit armature currents

$k_{ad,load}$ Active load active damping gain

$k_{ad,vsm}$ Virtual synchronous machine active damping gain

$k_{d,sm}$ Synchronous machine damping factor

$k_{d,vsm}$ Virtual synchronous machine damping factor

k_{ffc} Current feed-forward gain

k_{ffe} Voltage feed-forward gain

$k_{ic,load}$ Active load current controller integral gain

$k_{ic,vsm}$ Virtual synchronous machine current controller integral gain

$k_{i,ex}$ Synchronous machine exciter controller integral gain

$k_{i,pll,load}$ Active load phase locked loop controller integral gain

$k_{i,pll,vsm}$ Virtual synchronous machine phase locked loop controller integral gain

$k_{\omega,sm}$ Synchronous machine active power-frequency droop gain

$k_{pc,load}$ Active load current controllers proportional gain

$k_{pc,vsm}$ Virtual synchronous machine current controllers proportional gain

$k_{p,ex}$ Synchronous machine exciter controller proportional gain

$k_{p,pll,load}$ Active load machine phase locked loop controller proportional gain

$k_{p,pll,vsm}$ Virtual synchronous machine phase locked loop controller proportional gain

k_{iv} Virtual synchronous machine voltage controllers integral gain

k_{pv} Virtual synchronous machine voltage controllers proportional gain

$k_{q,sm}$ Synchronous machine reactive power-voltage droop gain

$k_{q,vsm}$ Virtual synchronous machine reactive power-voltage droop gain

l_{11d} Synchronous machine per unit direct axis damper winding self-inductance

l_{11q} Synchronous machine per unit quadrature axis damper winding self-inductance

l_{1d} Synchronous machine per unit direct axis damper winding leakage inductance

l_{1q} Synchronous machine per unit quadrature axis damper winding leakage inductance

l_{ad} Synchronous machine per unit armature direct axis mutual inductance

l_{aq} Synchronous machine per unit armature quadrature axis mutual inductance

l_f Virtual synchronous machine per unit filter inductors inductance

l_{f1d} Synchronous machine per unit mutual inductance between the field and direct axis damper circuits

l_{fd} Synchronous machine per unit field circuit leakage inductance

l_{ffd} Synchronous machine per unit field circuit self-inductance

l_g Per unit grid equivalent inductance

l_l Synchronous machine per unit armature leakage inductance

λ_i i-th eigenvalue

$\mathbf{m}_{load}$ Active load machine modulation index

$\mathbf{m}_{vsm}$ Virtual synchronous machine modulation index

ω^*_{sm} Synchronous machine per unit angular frequency reference (set-point)

ω^*_{vsm} Virtual synchronous machine per unit angular frequency reference (set-point)

$\omega_{ad,load}$ Active load active damping low-pass filters cut-off angular frequency

$\omega_{ad,vsm}$ Virtual synchronous machine active damping low-pass filters cut-off angular frequency

ω_b angular frequency/speed base value

$\omega_{f,sm}$ Synchronous machine reactive power measurement low-pass filter cut-off angular frequency

ω_g Per unit grid angular frequency

$\omega_{lp,pll}$ Phase locked loop high-pass filter cut-off angular frequency

$\omega_{lp,pll}$ Virtual synchronous machine Phase locked loop low-pass filters cut-off angular frequency

$\omega_{pll,load}$ Active load per unit estimated grid angular frequency (Phase locked loop output signal)

ω_{qf} Virtual synchronous machine reactive power measurement low-pass filter cut-off angular frequency

ω_{sm} Synchronous machine per unit rotor angular speed

ω^*_{sm} Synchronous machine per unit (external) angular frequency/speed reference (set-point)

ω_{vsm} Virtual synchronous machine per unit virtual rotor angular spee

$p_{m,sm}$ Synchronous machine per unit mechanical input power output

$p_{o,vsm}$ Virtual synchronous machine per unit active power output (measurement)

$\boldsymbol{\varphi}_{load}$ Active load per unit low-pass filtered $\mathbf{v}_{o,loadd}$ measurement

$\boldsymbol{\varphi}_{vsm}$ Virtual synchronous machine per unit low-pass filtered $\mathbf{v}_{o,vsm}$ measurement

PLL Phase Locked Loop

ψ_d Synchronous machine per unit armature flux linkages direct axis component

ψ_q Synchronous machine per unit armature flux linkages quadrature axis component

$q_{m,vsm}$ Virtual synchronous machine per unit reactive power measurement

r_{1d} Synchronous machine per unit damper direct axis resistance

r_{1q} Synchronous machine per unit damper quadrature resistance

r_a Static load per unit resistance

r_a Synchronous machine per unit armature resistance

r_{fd} Synchronous machine per unit field resistance

r_f Per unit filter resistance

r_g Grid filter resistance

S_{rated} Rated (apparent) power

SRRF Synchronously Rotating Reference Frame

T_a Virtual synchronous machine virtual inertia time constant

T_{ex} Synchronous machine exciter time constant

T_{gt} Synchronous machine governor and turbine time constant

T_M Synchronous machine inertia time constant

$\tau_{,sm}$ Synchronous machine per unit input torque

$\tau_{e,sm}$ Synchronous machine per unit electromagnetic torque

θ_{load} Active load phase angle

$\theta_{pll,load}$ Active load phase locked loop phase angle

$\theta_{pll,vsm}$ Virtual synchronous machine phase locked loop phase angle

θ_{sm} Synchronous machine rotor phase angle

θ_{vsm} Virtual synchronous machine phase angle

$\mathbf{u}_{load}$ Active load state-space model input vector

$\mathbf{u}_{sm}$ Synchronous machine state-space model input vector

$\mathbf{u}_{sys}$ Hybrid ship power system state-space model input vector

$\mathbf{u}_{vsm}$ Virtual synchronous machine state-space model input vector

$\hat{v}^*_{sm}$ Synchronous machine per unit voltage amplitude reference

$\hat{v}^*_{vsm}$ Virtual synchronous machine per unit voltage amplitude reference

$\mathbf{v}_{cv,load}$ Active load per unit output voltage

$\mathbf{v}_{cv,vsm}$ Virtual synchronous machine per unit output voltage

$\mathbf{v}_m$ Virtual synchronous machine per unit filtered output voltage for electrical model

$\mathbf{v}_{o,load}$ Active load per unit output voltage

$\mathbf{v}_{o,vsm}$ Virtual synchronous machine per unit output voltage

$\mathbf{v}_{pll,load}$ Active load per phase locked loop voltage

$\mathbf{v}_{pll,vsm}$ Virtual synchronous machine per phase locked loop voltage

$\mathbf{v}_{sm}$ Synchronous machine per unit armature voltage

$v_{o,vsm}^{pll}$ Virtual synchronous machine per unit voltage in PLL SRRF

$v_{o,vsm}^{vsm}$ Virtual synchronous machine per unit voltage in VSM SRRF

V_{rated} Rated (apparent) voltage

$v_{DC,load}$ Active load per unit DC link voltage (measured)

$v_{DC,vsm}$ Virtual synchronous machine per unit DC link voltage (measured)

v_{fd} Synchronous machine per unit field voltage

v_{fd}^{*} Synchronous machine per unit field voltage reference

$v_{o,load}$ Active load synchronous machine per unit output

$\mathbf{v}_{ad,vsm}^{*}$ Virtual synchronous machine per unit active damping term

$\hat{\mathbf{v}}_g$ Grid per unit voltage

$\hat{v}_{g,d}$ Grid per unit direct axis voltage

$\hat{v}_{g,q}$ Grid per unit quadrature axis voltage

VSC Voltage Source Converter

VSM Virtual Synchronous machine

$\mathbf{x}_{load}$ Active load state-space model state vector

$\mathbf{x}_{sm}$ Synchronous machine state-space model state vector

$\mathbf{x}_{sys}$ Hybrid ship power system state-space model state vector

$\mathbf{x}_{vsm}$ Virtual synchronous machine state-space model state vector

ξ Virtual synchronous machine per unit controllers integrators states

ζ Synchronous machine per unit exciter controller integrator state

Chapter 1

Introduction

1.1 Motivation

The International Maritime Organization (IMO) has proposed stringent regulations to reduce emissions and improve energy efficiency from the marine industry. New technologies are being investigated to comply with these regulations, such as all electrical ships and hybrid-electrical ships. Energy storage systems (ESSs), with zero-emission, are still challenging for all types of marine vessels due to their low energy density[8, 35]. The low energy density in ESS can be compensated by the conventional engine in the marine hybrid power system. Hybridization of vessels is therefore for complying with these methods while giving better energy-efficiency, flexibility, and reliability [2]. Moreover, it helps to reduce fuel consumption and environmental impacts. In addition, cycle assessment shows that it is more environment friendly compared with conventional power systems [31].

Hybrid architecture and advanced control systems can reduce emissions and fuel consumption up to 30% to 50% [21]. Load leveling, peak shaving, spinning reserve, zero-emission operation, and strategic loading are all operating modes that can contribute to the reduction of fuel consumption in hybrid power systems [45]. However, the hybridization of the power system also increases its complexity. Nevertheless, the hybridization of AC distributed power systems has allowed for the use of well-developed control, safety, and voltage transformation systems when compared to DC systems. Utilizing an AC distributed power system also allows for the use of a Virtual Synchronous Machine (VSM) for power conversion for the ESS.

The concept of VSM is emerging as a flexible approach for controlling power electronic converters in grid-connected as well as stand-alone applications. There are several VSM implementations and what they all have in common is the emulation of inertia and damping of a traditional Synchronous Machine (SM). The VSM shows the capability to operate in both grid-connected and islanded operations, as well as operate in isolated

power systems [13, 16]. The VSM has proven its capabilities to control power systems in all-electric operation but is the capabilities to operate in a hybrid ship power system with SMs and large dynamic loads have yet to be investigated.

1.2 Objective

This thesis should include a review of the performance of a power electronic converter controlled as a VSM when operated in a typical hybrid ship AC distributed power system. A state-space model for the investigated power system should be developed for analytical purposes, as well as a Simulink model for time-domain simulations used to verify the developed state-space model. The small-signal model should be validated against the detailed time-domain simulation by evaluating the time-response to small perturbations. Further on, establish tools for linear system analysis to be applied to the validated model to analyze how the use of the VSM can influence the small-signal dynamics of the hybrid ship AC distributed power system under various system operating conditions.

1.3 Approach

To achieve the objective of the thesis, relevant functions and programs have been developed in Matlab programming language, and models have been created in Simulink. Programs have been developed to simulate and analyze the behavior of the studied system. Time-domain simulations have been done in Simulink, while the algebraic matrix manipulation and small-signal analysis have been carried out in Matlab.

A nonlinear state-space model for the SM, active load and VSM each connected to a stiff-grid has been developed. The three models were verified with the electrical models made in Simulink. Eventually, the three components were modeled together to complete the hybrid ship power system. The nonlinear state-space model of the power system was also verified with an electrical model in Simulink.

For a given set of system parameters and steady-state inputs, the eigenvalues and vectors functions have been made in Matlab. This was done for the purpose to calculate the steady-state conditions, the small-signal participation factors, and parametric sensitivity has been investigated. The developed model has then been used to analyze the small-signal stability characteristics of the studied system.

1.4 Scope and limitations

The aim of this thesis has been to develop a hybrid ship power system model with a VSM and analyze the small-signal stability of the model. The component of the system has been modeled separately and verified before combined. Component-level considerations, such as design, sizing, manufacturing, extensive modeling, and tuning, were initially left out, and only grid-connected operation was taken into account.

In the modeling of the SM, the windings of the SM stator are presumed to be distributed sinusoidally through the air gap. Magnetic hysteresis and stator slot-induced differences in rotor inductances with rotor position have been ignored. Similarly, mechanical losses have been ignored in the damping of the rotor [33]. The effect of magnetic saturation is also ignored, thus all circuits are assumed to be linearly coupled (linear flux-current relationship) [38]. For the sake of simplicity, a simple model has been used to express the dynamic characteristics of the governor, turbine and exciter.

When modeling the electronic power conversion, it was assumed that the switching frequency is high enough that the switching action does not affect the progress of the state. As a result, switching effects and any delay caused by the implementation of pulse-width modulation (PWM) were ignored, and an ideal average model was assumed [34]. Assuming that the PWM does not affect the dynamics of the control scheme within the normal operating range, the restrictions required for the safe operation of the electronic power converter, the controlled output saturation, and the anti-windup function are excluded from the model [34].

For the DC side of the power electronic converter, no application-specific constraints have been considered, so modeling and regulation of the energy resources on the DC side have been ruled out. In addition, the requested AC power has been presumed to be available on the DC side [34]. Moreover, the dynamics of the DC side are not included so that decoupling between the dynamics of the AC- and DC-side can be achieved.

1.5 Report outline

In *Chapter 1, Introduction*, the work of the thesis was introduced, including the motivation, problem description, scopes and limitations.

In *Chapter 2, Background*, the fundamentals for the thesis are explained and methods used for the study are presented.

In *Chapter 3, Modelling*, the main components and controllers of each of the three units are defined before the modeling of the *hybrid ship power system* is presented, as a basis for developing a state-space-model for the *hybrid ship power system*

In *Chapter 4, Model verification*, the state-space models for the SM, active load, VSM, and the *hybrid ship power system* are verified with the simulated models.

In *Chapter 5, Eigenvalue analysis*, the small-signal model of the hybrid power system is used to validate the operating range, inspect system dynamics to load change, calculate participation factors and investigate parametric sensitivity.

In *Chapter 6, Conclusion and future work*, the results are summarized and the outcome of the thesis discussed. Some suggestions for what can be done in future work are also presented.

Chapter 2

Background

This chapter presents background for the principles and research that the work of this thesis is based on. The chapter is divided into four sections

- 2.1 covers the developments in the maritime sector and where it is heading;
- 2.2 covers the the relevance of power system stability, including voltage, frequency and phase angle stability
- 2.3 covers small signal-stability and concepts that are relevant, such as eigenvalue analysis, participation factor and state-space representation
- 2.4 covers the history and development of the VSM

2.1 Marine power systems

Electrical installations are present in any ship, from powering of equipment for communication and navigation, alarms and monitoring systems, running motors for pumps, fans, and winches, to large-scale dynamic loads. The concept of high power electrical propulsion dates back more than 100 years [40]. Electrical propulsion systems are found to be beneficial in several ship applications of varying sizes, such as cruise liners, supply vessels, drill-ships, ice-breakers, shuttle-tankers, naval ships, and floating production vessels [23].

The concept of electrical propulsion replaces the main diesel or crude oil propulsion engines with electric motors that splits the power production into several smaller generators. Compared to diesel engines, with peak efficiency near the rated operating point, an electric motor can be designed to have very high efficiency over the entire operating range of speed and power output. By selecting the optimal power output from the generators to supply the demanded power, a ship will be able to operate with high efficiency for the whole range of operation [23]. Alongside the introduction of electrical propulsion comes the need for ensuring power system stability. Both stability and control of generation,

frequency, and voltage must meet the requirement of both performance and ability to optimize the longevity of system components.

2.1.1 Electrification of marine vessels

Due to regulatory demands for a cleaner ship industry, more and more vessels are being fitted with diesel-electric solutions. Diesel generators in ships are known to contribute substantially to greenhouse gas emissions. With the extensive development of battery technologies, weight and limited capacity are slowly becoming an issue of the past. The shift towards an all electrical ship industry is however slow. Retrofitting older vessels with battery solutions is therefore a practical way of meeting new regulatory energy and emission standards. As a result, several companies are specializing in retrofitting exciting vessels. Examples are Seam, ESR-Floattech, The Explorer, DNV GL and ABB [1, 17, 22, 4, 19].

With regards to operational benefits, electric and hybrid electrical-powered ships can minimize noise and vibrations, optimize onboard generators, enhance vessel responsiveness and safety, and most importantly, reduce fuel consumption [30]. Compared to heavy fuel oil and marine diesel; electric and hybrid-electrical ships are cleaner, more efficient, and have a lower energy cost of distance traveled. All these factors are expected to drive the adoption of hybrid and pure electric boats for the foreseeable future. Not only that, according to the Business Fortune insight, the global electric ships market size was 5.50 billion us dollars in 2019, and is estimated to reach an estimated 10.82 billion us dollars by 2027 [18].

2.1.2 Hybrid ships

When designing a new hybrid ship or retrofitting an older vessel, many suitable energy storage systems (ESSs) technologies are available. Energy density, cost, size, weight, lifetime expectancy, charge, and charge/discharge rates are all things that need to be considered. ESS can contribute with *load shaving*, *peak shaving*, *frequency* and *voltage control*, or serve as a *backup generator*[44]. Even though the advantages of ESS in power systems are many, it does not come without challenges. Many of the available and suitable ESS technologies are expensive solutions and are dependent on power conversion devices relative to AC or DC power systems.

Figure 2.1 shows the single line diagram of a typical AC hybrid ship power system, with a battery EES (BESS). To satisfy the power supply reliability and economical efficiency, the power systems are incorporated with several generators connected to the AC bus. The batteries are connected to the AC bus using DC/AC converters and the motors are connected using motor drives. The AC/DC converter of the marine power system topology is commonly implemented as three-phase voltage source converters (VSCs). The dynamics of this hybrid system are dictated by the power generating units and loads of the system, and for that reason their controllers are tightly integrated and coordinated, having a large impact on the stability of the power system.

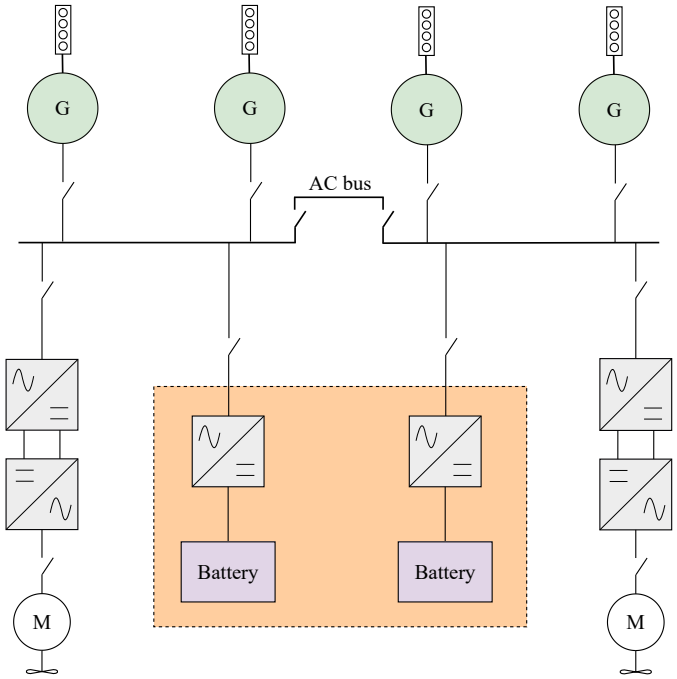

Figure 2.1: Example of a single line diagram of AC distributed hybrid marine power system

2.1.3 Isolated power systems

The hybrid ship power system has a lot in common with isolated onshore power systems; the control strategies, design principles and components are mostly the same [48]. Examples are voltage and frequency control schemes, power-sharing methods, strategies for power quality improvement and energy managements systems [3, 32, 47]. There are however some differences between the hybrid ship power system and larger scale isolated terrestrial power systems.

Due to the limited rotational inertia of the SMs in the ship power system, rapid load change can cause frequency fluctuations and the frequency of the ship system cannot be assumed constant as is for the onshore system. Instead of generation scheduling, the ship power generation has load-sharing most often realized by generator droop control. The short electrical distance in the ship system results in low impedance, leading to high increases in the coupling between the components of the power system. However, the shorter electrical distance also makes it easier to obtain data and measurements [44].

The rapid load changes in the ship power system are a result of the power demand from the propulsion system and other high-rated equipment. This leaves us with a system where both the active and reactive power changes rapidly. In large-scale commercial grids, time-scale separation is used for system analysis, as all the time constants are

quantified. The time constants of motor dynamics, controls, and electrical dynamics are all in the time range of milliseconds to seconds. By that fact, it is hard to analyze ship power systems in the same manner as for the commercial grids [44]. Power system stability, therefore, plays an important role when looking into the control and stability of a hybrid ship power system.

2.2 Power system stability

Power system stability is defined as the ability of an electric power system, for a given initial operating condition, to regain a state of operating equilibrium after being subjected to a physical disturbance, with most system variables restricted so that practically the entire system remains intact [29].

The synchronous machine (SM) is the heart of most power systems. The machine's rotor dynamics are directly coupled with the power systems frequency and the system frequency is a direct indicator of the balance between generation and load. The rotational inertia equation of an SM, therefore, plays a central to power system stability analysis [33]. A per unit representation of the swing equation can be found in (2.1). The equation describes the effect of an unbalance between the electromagnetic torque, τ_e, and the mechanical input torque, τ_m, where $\delta\theta_{sm}$ is the rotor angular deviation from the reference phase angle.

$$T_m \frac{\mathrm{d}^2\delta\theta_{sm}}{\mathrm{d}t^2} = \tau_m - \tau_e - k_d \frac{\mathrm{d}\delta\theta_{\mathrm{sm}}}{\mathrm{d}t} \tag{2.1}$$

The inertia constant, T_m, is the time it takes for rated torque to accelerate the rotor from steady-state position to synchronous speed. This inertia time constant is directly connected to the combined moment of inertia of the SM and the prime mover. The term $k_d \frac{\mathrm{d}\delta_{\mathrm{m}}}{\mathrm{d}t}$ is incorporated to represent a component of damping torque that is not included in the calculation of τ_e, where $k_{d,sm}$ is the damping factor. The term is proportional to the rotor angular frequency deviation $\frac{\mathrm{d}\delta\theta_{\mathrm{sm}}}{\mathrm{d}t}$ from the synchronous frequency ω_s, as shown in equation 2.2.

$$\frac{\mathrm{d}\delta\theta_{sm}}{\mathrm{d}t} = \delta\omega_{sm} = \omega_{sm} - \omega_s \tag{2.2}$$

2.2.1 Rotor angle stability

Rotor angle stability refers to the stability category concerned with the capacity of the interconnected SMs in a power system to stay in *synchronism* after experiencing a disturbance. For SMs to be interconnected, the frequency of their stator voltage and currents needs to be the same, which means that the rotors of all the interconnected SMs rotate at the same speed, i.e. the interconnected SMs are in *synchronism* [38]. The capacity

of each interconnected SM to preserve or recover equilibrium when there is an unbalance between the mechanical and electrical torque is what determines the stability of the power system.

When a power system undergoes disturbance causing the acceleration/deceleration of the rotor speed of an SM, the angular deviation of the rotor, $\delta\theta_{sm}$, will increase/decrease concerning the synchronous frequency ω_s. An important characteristic of power system stability to consider is then the relationship between interchange power and angular positions of the SM rotors. This indicates that in a simple power system consisting of two SMs, an increased rotor angular position transfers part of the output power from the slower SM to the faster SM. The power transfer is a function of the angular separation ($\delta\theta$) between the two SMs. This active power-angle relationship is highly non-linear[38]. The stability of the system then depends on the condition that the deviations in angular positions of the rotors result in enough restoring torques.

2.2.2 Voltage and frequency stability

Marine vessels with diesel-electric AC power systems can not be expected to have a constant frequency due to the large dynamic loads connected to the AC bus. A load change will typically induce voltage and frequency variation, and can potentially cause instability.

Voltage stability is the ability of a power system to maintain steady (or bounded) bus voltage under normal operation after a disturbance. It depends on the ability to maintain and restore equilibrium between load demand and load supply from the power system [29]. Voltage instability often occurs together with rotor angle stability. The distinction between angle stability and voltage stability is therefore hard to differentiate.

Frequency stability is the ability of the power system to maintain steady-state frequency, following a disturbance. Inertia plays a vital role in maintaining the *frequency stability* of power systems. The reduction of inertia in power systems challenges the regulation of the time derivative of frequency, i.e. rate-of-change-of (ROCOF). The ROCOF after a disturbance is higher in a low inertia power system than in a power system with sufficient inertia. For a system with high inertia, the synchronous angular frequency, ω_s, changes slowly, and thus, it can easily be stabilized [20].

2.3 Small-signal stability

Small-signal (or small-disturbance) stability is concerned with a system's ability to be stable under small disturbances. In this context, a disturbance is considered to be small if the equations that describe the resulting response of the system may be linearized and analyzed. Linearizing system equations around an operating point enables the use of linear technique to calculate relevant sensitivity information and be used for eigenvalues analysis [33].

Eigenvalue analysis gives the possibility to examine the damping and frequency of the oscillatory terms, as well as the speed of the non-oscillatory terms, for a system dynamic response. With the eigenvalues of the system an investigation into the participation factor can give useful insight into the interaction between the system states and modes [7, 33, 38, 43].

2.3.1 State-space representation

From the nonlinear system equations a state-space representation of the system with its output can be written as (2.1), where column vector $\mathbf{x}$ is the *state vector* $\mathbf{u}$ is the *input vector*.

$$\begin{aligned} \dot{\mathbf{x}} &= \mathbf{f}(\mathbf{x}, \mathbf{u}) \\ \mathbf{y} &= \mathbf{g}(\mathbf{x}, \mathbf{u}) \end{aligned} \tag{2.1}$$

The system can then be linearized around the steady-state operation, where the linearization is done with the use of the first-order Taylor expansion of the nonlinear system [38]. By defining the perturbations $\Delta\mathbf{x}$ and $\Delta\mathbf{u}$, and since $\mathbf{x}_0$ $\mathbf{u}_0$ satisfy $\mathbf{f}(\mathbf{x}_0, \mathbf{u}_0)$=0 we have that the first-order Taylor expression for the system around $\mathbf{x}_0$ $\mathbf{u}_0$ is

$$\begin{aligned} \dot{\mathbf{x}} &= \left.\frac{\partial \mathbf{f}}{\partial \mathbf{x}}\right|_{x_0,u_0} \mathbf{x} + \left.\frac{\partial \mathbf{f}}{\partial \mathbf{u}}\right|_{x_0,u_0} \mathbf{u} \\ \mathbf{y} &= \left.\frac{\partial \mathbf{h}}{\partial \mathbf{x}}\right|_{x_0,u_0} \mathbf{x} + \left.\frac{\partial \mathbf{h}}{\partial \mathbf{u}}\right|_{x_0,u_0} \mathbf{u} \end{aligned} \tag{2.2}$$

By solving the system with regards to the first derivative equal to zero the desired linearization points can be found, and the system with output can be expressed as (2.3) where $\mathbf{A}$, $\mathbf{B}$, $\mathbf{C}$ and $\mathbf{D}$ represents the system matrices.

$$\begin{aligned} \boldsymbol{\Delta}\dot{\mathbf{x}} &= \mathbf{A}\boldsymbol{\Delta}\mathbf{x} + \mathbf{B}\boldsymbol{\Delta}\mathbf{u} \\ \boldsymbol{\Delta}\mathbf{y} &= \mathbf{C}\boldsymbol{\Delta}\mathbf{x} + \mathbf{C}\boldsymbol{\Delta}\mathbf{u} \end{aligned} \tag{2.3}$$

2.3.2 Eigenvalue analysis

The eigenvalues of a system are given as the scalar parameter λ for which there exist a non-trivial solution to the equation

$$\det(\mathbf{A} - \lambda\mathbf{I}) = 0 \tag{2.4}$$

The expansion of the determinant gives the *characteristic equation* and the n solutions of λ are the *eigenvalues* of $\mathbf{A}$. The eigenvalues can be real or complex conjugate pairs. The real component of the eigenvalues gives the settling time, and the imaginary component

gives the frequency of oscillation. The unit for the real part of the is $1/s$ while the imaginary part is rad/s, where s is short for seconds. The damping ratio of a complex eigenvalue is given by

$$\frac{-\operatorname{real}(\lambda)}{\sqrt{\operatorname{real}(\lambda)^2 + \operatorname{imag}(\lambda)^2}} \tag{2.5}$$

The damping ratio determines the rate of decay of the amplitude of the oscillations. Trajectory behavior of the eigenvalues can be used to determine the stability of a system for different parameter values.

2.3.3 Participation factor

The eigenvalue analysis can identify modes that give the oscillations and damping of the system. To identify the different states contributing to the modes, the participation factor can be calculated as a measure of relative participation. The participation factor matrix is defined as

$$\mathbf{P} = \begin{bmatrix} p_{11} & p_{12} & \cdots & p_{1n} \\ p_{21} & p_{22} & \cdots & p_{2n} \\ \cdots & \cdots & \cdots & \cdots \\ p_{n1} & p_{n2} & \cdots & p_{nn} \end{bmatrix} = \begin{bmatrix} \phi_{11}\psi_{11} & \phi_{12}\psi_{21} & \cdots & \phi_{1n}\psi_{n1} \\ \phi_{21}\psi_{12} & \phi_{22}\psi_{22} & \cdots & \phi_{2n}\psi_{n2} \\ \cdots & \cdots & \cdots & \cdots \\ \phi_{n1}\psi_{1n} & \phi_{n2}\psi_{2n} & \cdots & \phi_{nn}\psi_{nn} \end{bmatrix} \tag{2.6}$$

where ψ and ϕ are the left and right eigenvalue matrix respectively. Each participation factor is the product of the kth element of the ith left and right eigenvector. This gives the sensitivity of the ith eigenvalue to the kth diagonal element of the state matrix [38]. Participation factor enables the analytical study of the sensitivity of eigenvalues to changes in the system parameters. The influence on slow and/or poorly damped modes are often of most interest [7, 33, 37, 43].

2.4 Virtual synchronous machine

The increase in penetration of renewable energy sources is apposing serious challenges to the development and operation of to-days onshore power systems. The renewable sources mainly depend on VSC topologies as grid interfaces[9]. When SMs are replaced by the VSC-connected renewable sources, the total rotating mass of the power system is reduced. This reduction of the total equivalent inertia can lead to problems with system stability and excessively high ROCOF during power system transients [36, 46, 51]. Control strategies based on the concept of virtual inertia have the potential to become a flexible framework for providing converter-based grid services for power systems.

The concept of the VSM was first introduced back in 2007 by Beck and Hess, as VISMA [5]. The concept is based on an inverter having the inertia and electromechanical damping

properties of an SM. As time has gone by several approaches have been documented and tested, varying in implementation and complexity[]. Different models can be used for implementing a mathematical SM model in the control system. There is however a trade-off in complexity for the high order models that give the most accurate and precise interpretation. [14] gives a classification of the complexity of the SM models that can be implemented for VSM.

VSM can help realize a flexible converter control structure, which can be connected to the grid and isolated and can be switched from one type to another without problems. Unlike traditional control schemes, the VSM can independently provide transient power exchange and frequency support as primary control actions, using only local information. The conceptual simplicity of the VSM is another advantage. This simplicity is due to the intuitive interpretation of their responses in correlation with the SM. However, to represent the energy storage simulating the moment of inertia, a sufficient energy buffer is required. Therefore, the current rating of the power converter and its configuration on the direct current (DC) side limit the amount of virtual inertia that this type of solution can provide [15].

Chapter 3

Modelling

The hybrid ship power system studied is a simplified model of the AC distributed hybrid marine power system introduced in section 2.1.2 (Figure 2.1). A one-line diagram of the power model can be observed in Figure 3.1. As the figure shows the model consists of three main parts, the SM, VSM, and Active Load. For practicality, each of the three components where modeled separately connected to a stiff grid, before combined to form the hybrid ship power system. The next three subsections describe each of the investigated components with their corresponding non-linear mathematical models.

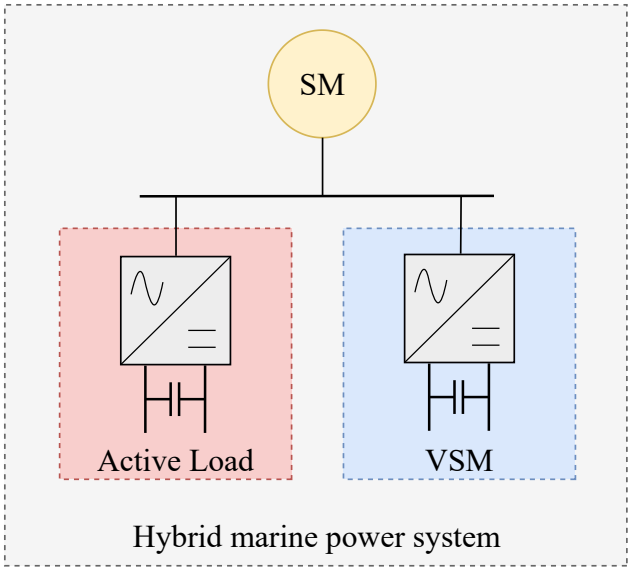

Figure 3.1: Hybrid ship power system description.

Upper case symbols represent the physical values of the electrical circuit. The electrical models are expressed in a Synchronous Rotating Reference Frame (SRRF) by an amplitude invariant Park Transformation, with the direct (d) axis aligned with a voltage

vector and the quadrature (q) axis leading the d-axis by 90°. At any time possible, the SRRF equations are presented in complex space-vector according (3.1). Balanced three-phase conditions have been assumed, so no zero sequence components are included. The angles of the systems are expressed in electrical radians and the angular frequencies are expressed in electrical radians per second. The control system implementation and modeling are based on per unit (pu) quantities denoted by lower case letters where the base values are defined from the apparent power ratings and the rated peak phase-to-neutral voltages [34, 38].

$$\mathbf{v} \triangleq v_d + \mathrm{j}v_q \tag{3.1}$$

(3.1) can therefore be used to express the active and reactive powers on complex or scalar form as in (3.2), where $\bar{\mathbf{i}}$ denotes the complex conjugate of $\mathbf{i}$.

$$\begin{aligned} p &= \mathrm{Re}(\mathbf{v} \cdot \bar{\mathbf{i}}) = v_d \cdot i_d + v_q \cdot i_q \\ q &= \mathrm{Im}(\mathbf{v} \cdot \bar{\mathbf{i}}) = -v_d \cdot i_q + v_q \cdot i_d \end{aligned} \tag{3.2}$$

The voltage amplitude is utilized for controllers and by using the measured dq-voltages the voltage amplitude $\hat{v}$ can be calculated as

$$\hat{v} = \sqrt{v_d^2 + v_q^2} \tag{3.3}$$

3.1 Synchronous machine

To obtain a complete model of the SM with the linear magnetic circuit the conventions and notations of [28] have been used. For the control of the SM [41] has been used. In developing the equations of the SM, some assumptions have been made; 1) the stator windings sinusoidally distributed along the air-gap; 2) the variations of the rotor inductance's with rotor position caused by the stator slots have been neglected; 3) magnetic hysteresis and magnetic saturation effects have also been neglected. With the magnetic saturation neglected, all circuits need to be assumed linearly coupled [38].

The simplified schematic of Figure 3.3 shows the coil orientation, assumed polarities, and rotor position references [38]. The stator circuit is encompassed of the three-phase armature windings, a, b, c, carrying AC-currents, while the rotor circuits consist of the field winding and damper circuits fd, $1d$ and $1q$. A DC voltage source, v_{fd}, is connected to the field winding. The solid rotor and/or damper windings are assumed to flow in two sets of closed circuits to a source of direct current; 1) one whose flux is in line with the field winding along the d-axis, $1d$; 2) one whose flux is at a right angle, along the q-axis [38].

The rotor phase angle, θ_{sm}, is defined as the angle by which the d-axis leads the phase a winding in the direction of rotation. As the rotor is rotating with respect to the stator,

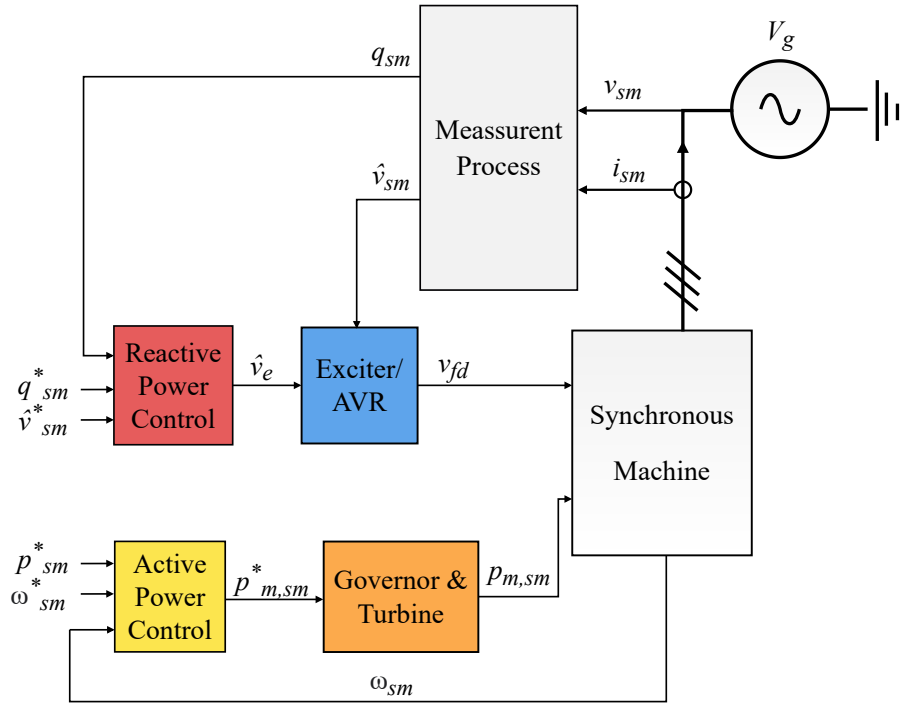

Figure 3.2: Overview of the synchronous machine with control structure.

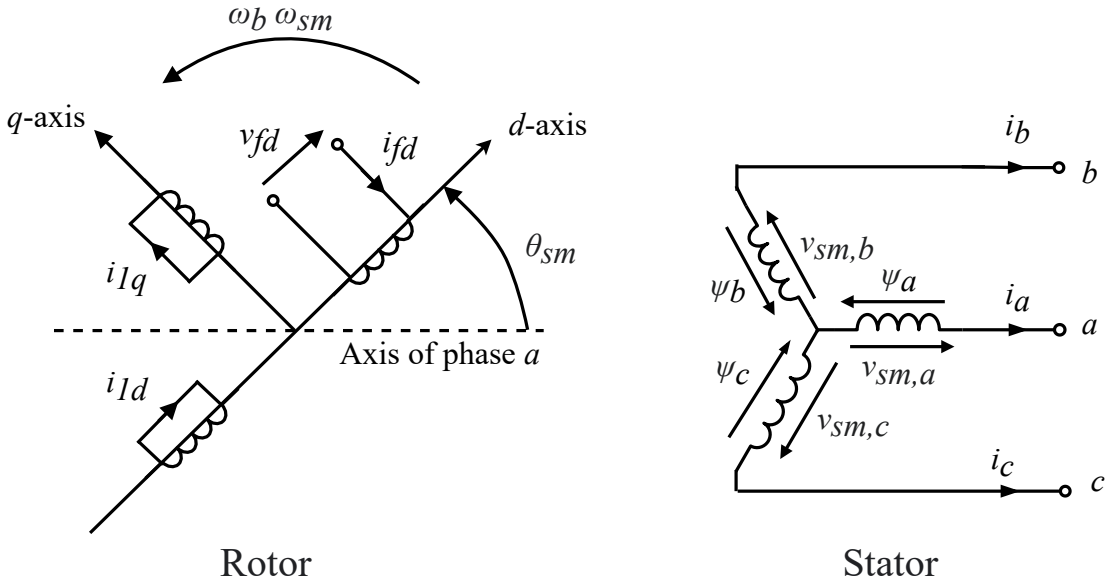

Figure 3.3: Stator and rotor circuits of the synchronous machine.

θ_{sm} is continuously increasing and is related to the rotor angular velocity ω_{sm} and time is

$$\theta_{sm} = \omega_b \omega_{sm} \cdot t \tag{3.1}$$

where ω_b is the angular frequency base value.

Following, the implementation of the SM model and each functional control block is presented. Together with the mathematical model of all system elements of Figure 3.2, the SM model makes up the basis for the development of the non-linear model of the SM system. The Park transformation, with θ_{sm} as the transformation angle, is utilized to express the equations associated with the stator circuits in the SM SRRF and to transform the control inputs.

3.1.1 Voltage and flux linkage equations

The d and q-axis stator voltage equations are given by

$$v_{sm,d} = \frac{1}{\omega_b}\frac{\mathrm{d}}{\mathrm{d}t}\psi_d - \psi_q \omega_{sm} - r_a i_{sm,d} \tag{3.2}$$

$$v_{sm,q} = \frac{1}{\omega_b}\frac{\mathrm{d}}{\mathrm{d}t}\psi_q + \psi_d \omega_{sm} - r_a i_{sm,q} \tag{3.3}$$

where r_a is the stator resistance, i_{sm} is the stator current, ψ_d and ψ_q are the d and q-axis stator flux linkages respectively. The voltage equations for the rotor are

$$v_{fd} = \frac{1}{\omega_b}\frac{\mathrm{d}}{\mathrm{d}t}\psi_{fd} + r_{fd} i_{fd} \tag{3.4}$$

$$0 = \frac{1}{\omega_b}\frac{\mathrm{d}}{\mathrm{d}t}\psi_{1d} + r_{1d} i_{1d} \tag{3.5}$$

$$0 = \frac{1}{\omega_b}\frac{\mathrm{d}}{\mathrm{d}t}\psi_{1q} + r_{1q} i_{1q} \tag{3.6}$$

where ψ_{fd}, ψ_{1d} and ψ_{1q} are the flux linkages, r_{fd}, r_{1d}, r_{1q} are the resistances and i_{fd}, i_{1d}, i_{1q} are the currents of the field and stator circuit's, respectively. The d and q-axis stator flux linkage equations are given (3.7) and (3.8), respectively, where l_l is the armature leakage inductance. l_{ad} and l_{aq} are the armature $d-$ and q-axis mutual inductance's, respectively.

$$\psi_d = -\left(l_{ad} + l_l\right) i_{sm,d} + l_{ad} i_{fd} + l_{ad} i_{1d} \tag{3.7}$$

$$\psi_q = -\left(l_{aq} + l_l\right) i_{sm,q} + l_{aq} i_{1q} \tag{3.8}$$

The rotor flux linkage equations are given by (3.9)-(3.11), where l_{f1d} is the mutual inductance between the field and d-axis damper winding, $l_{ffd}, l_{11d}, l_{11q}$ are the self-inductance's of the field and the d and q-axis damper windings, respectively, and l_{fd}, l_{1d}, l_{1q} are the corresponding leakage inductance's.

$$\psi_{fd} = l_{ffd} i_{fd} + l_{f1d} i_{1d} - l_{ad} i_{sm,d} \tag{3.9}$$

$$\psi_{1d} = l_{f1d} i_{fd} + l_{11d} i_{1d} - l_{ad} i_{sm,d} \tag{3.10}$$

$$\psi_{1q} = l_{11q} i_{1q} - l_{aq} i_{sm,q} \tag{3.11}$$

where, $l_{ffd} = l_{f1d} + l_{fd}$, $l_{11d} = l_{f1d} + l_{1d}$ and $l_{11q} = l_{aq} + l_{1q}$. While equations (3.2)-(3.11) can be used directly to determine the performance of the SM, the equivalent circuits shown in Figure (3.4) and (3.5), is included to provide a visual description of the machine model [38].

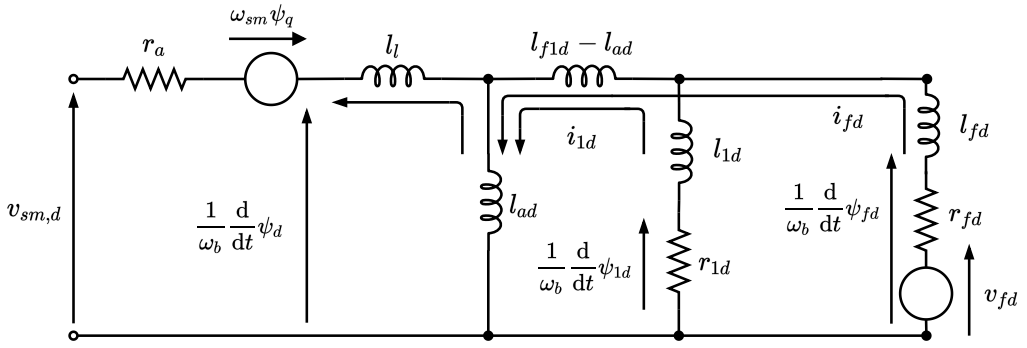

Figure 3.4: Synchronous machine d-axis equivalent circuit.

3.1.2 Equation of motion

The dynamics of the SM is modeled from the swing equation (3.12), where the details of the equation is discussed in the background section. The equation includes; 1) the inertia time constant T_M; 2) $\delta\omega_{sm}$ the rotor angular speed deviation from the grid frequency (3.13); 3) $\tau_{m,s}$ the mechanical input (3.14); 4) $\tau_{e,sm}$ the electromagnetic torque (3.15); 5) $k_{d,sm}\delta\omega_{sm}$ the damping component.

$$\frac{\mathrm{d}\delta\omega_{sm}}{\mathrm{d}t} = \frac{\tau_{m,sm}}{T_M} - \frac{\tau_{e,sm}}{T_M} - \frac{k_{d,sm}\delta\omega_{sm}}{T_M} \approx \frac{\mathrm{d}\omega_{sm}}{\mathrm{d}t} \tag{3.12}$$

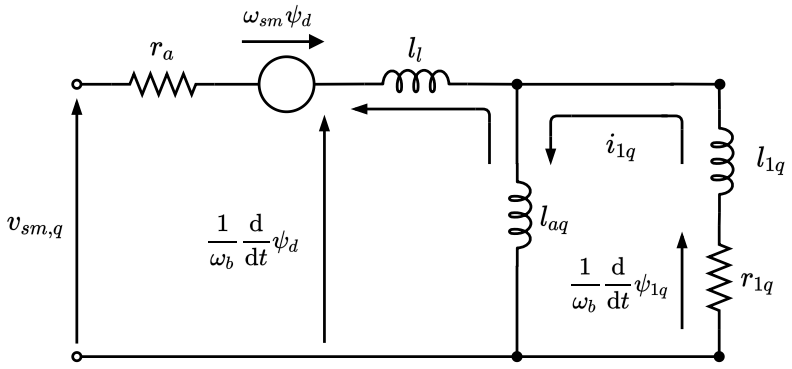

Figure 3.5: Synchronous machine q-axis equivalent circuit.

$$\delta\omega_{sm} = \omega_{sm} - \omega_g \tag{3.13}$$

$$\tau_{m,sm} = \frac{p_{m,sm}}{\omega_{sm}} \tag{3.14}$$

$$\tau_{e,sm} = \psi_d i_{sm,q} - \psi_q i_{sm,d} \tag{3.15}$$

From (3.13) a expression for the rotor phase angle displacement, $\delta\theta_{sm}$, can be found

$$\frac{\mathrm{d}\delta\theta_{sm}}{\mathrm{d}t} = \omega_b\delta\omega_{sm} = \omega_b\omega_{sm} - \omega_b\omega_g \tag{3.16}$$

3.1.3 Reactive power control, automatic voltage regulator and exciter

The droop-based reactive power control, automatic voltage regulator (AVR) and exciter for the SM control is shown in Figure 3.6. The dynamic characteristics of the exciter are modelled as a first-order system (3.17) with the time constant T_{ex}. The exciter model gives the field voltage used to calculate the field current of the SM.

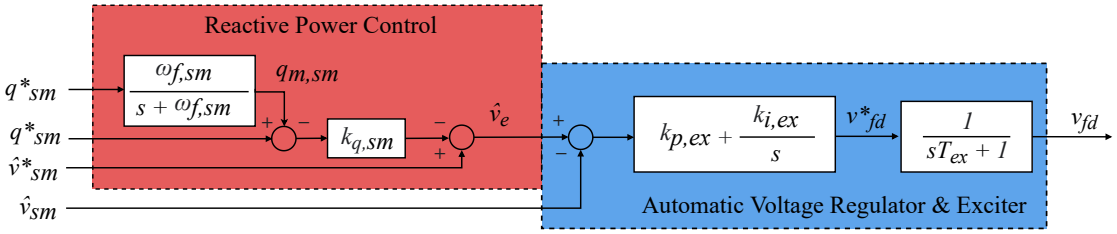

Figure 3.6: Reactive power control, AVR and exciter diagram.

$$\frac{\mathrm{d}v_{fd}}{\mathrm{d}t} = \frac{v_{fd}^*}{T_{ex}} - \frac{v_{fd}}{T_{ex}} \tag{3.17}$$

The automatic voltage regulator (3.18) gives the reference field voltage, v_{fd}^*, for exciter model. It is modelled as a PI-controller where its reference voltage, $\hat{v}_e$, is compared with the armature voltage amplitude, $\hat{v}_{sm}$. The PI-controller proportional and integral gains are $k_{p,ex}$ and $k_{i,ex}$, respectively, and the state ζ (3.19) represents the integrator of the PI controller.

$$v_{fd}^* = k_{p,ex}\left(\hat{v}_e - \hat{v}_{sm}\right) + k_{i,ex}\zeta \tag{3.18}$$

$$\frac{d\xi_{sm}}{dt} = \left(\hat{v}_{sm}^* - \hat{v}_{o,sm}\right) + k_{q,sm}\left(q_{sm}^* - q_{m,sm}\right) \tag{3.19}$$

The reactive power controller output signal, $\hat{v}_e$, is the reference for the automatic voltage regulator and is given by (3.20). It is the sum of reactive power droop and the voltage amplitude reference $\hat{v}_{sm}^*$.

$$\hat{v}_e = \hat{v}_{sm}^* + k_{q,sm}\left(q_{sm}^* - q_{m,sm}\right) \tag{3.20}$$

The gain k_q is the reactive power droop gain acting on the difference between the reactive power reference q_{sm}^* and the filtered reactive power measurement $q_{m,sm}$. The equation for the first-order low-pass filter is given by (3.21), where q_{sm} is the reactive power measurement (3.22) and $\omega_{f,sm}$ is the filter cut-off angular frequency.

$$\frac{\mathrm{d}q_{m,sm}}{\mathrm{d}t} = -\omega_{f,sm}q_{m,sm} + \omega_{f,sm}q_{sm} \tag{3.21}$$

$$q_{sm} = -v_{sm,d}i_{sm,q} + v_{sm,q}i_{sm,d} \tag{3.22}$$

3.1.4 Governor, turbine and active power control

For simplicity, the dynamic characteristics of the governor and the speed turbine are modeled together as a first-order system (3.23), with the time constant T_{gt}. The block diagrams for the SM active power control, speed governor and turbine are shown in Figure 3.7.

$$\frac{\mathrm{d}p_{m,sm}}{\mathrm{d}t} = \frac{p_{m,sm}^*}{T_{gt}} - \frac{p_{m,sm}}{T_{gt}} \tag{3.23}$$

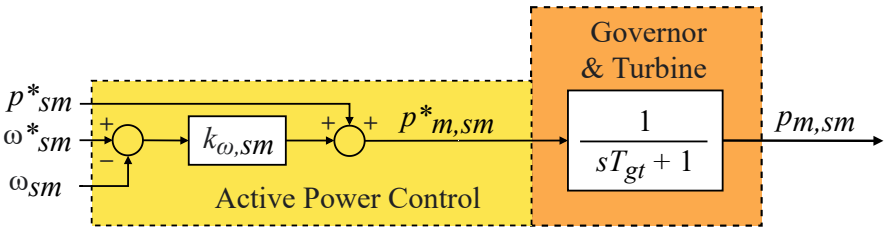

Figure 3.7: Active power, governor and turbine.

The active power control is supplied by an external frequency droop and is characterized by the droop constant k_ω acting on the difference between the SM speed ω_{sm} and the input reference ω^*_{sm}. The sum of the frequency droop effect and an external power reference set-point, p^*_{sm}, gives the mechanical input power $p^*_{m,SM}$ for the SM:

$$p^*_{m,sm} = p^*_{sm} - k_{\omega,sm}\left[\omega_{sm} - \omega^*_{sm}\right] \tag{3.24}$$

3.1.5 Synchronous reference frame orientation ('SRRF')

The synchronization of the SM to the grid is based on the phase angle orientation of the SM rotor. The phase angle θ_{sm} is used in the transformation between the stationary reference frame and the SM-oriented SRRF. Since the SM-oriented SRRF rotates at the same frequency as the grid voltage in a steady-state, the phase angle will continually increase, as is illustrated in the vector diagram in Figure 3.8. As the vector diagram also indicates, the phase angle $\delta\theta_{sm}$, represents the phase difference between the SM-orientation SRRF and the spinning grid voltage vector. Assuming that the grid voltage amplitude, $\hat{v}_g$, to be known the grid voltage vector in the SM SRRF can be given as

$$\mathbf{v}_g^{sm} = \hat{v}_g \mathrm{e}^{-\mathrm{j}\delta\theta_{sm}} \tag{3.25}$$

3.1.6 Non-linear model

The equations needed for the detailed modelling of the SM in grid-connected operation have been reduced down to a model on state-space form with 11 distinct state variables and 7 input signals. The resulting non-linear state space model of the overall system is given in Appendix A.1, with the state vector $\mathbf{x}_{sm}$ (3.26) and the input vector $\mathbf{u}_{load}$ (3.27).

$$\begin{aligned}\mathbf{x}_{sm} \triangleq [\, & i_{sm,d} \quad i_{sm,q} \quad i_{fd} \quad i_{1d} \quad i_{1q} \quad \cdots \\ & \cdots \quad \omega_{sm} \quad \delta\theta_{sm} \quad p_{m,sm} \quad q_{m,sm} \quad \zeta \quad v_{fd} \,]^T\end{aligned} \tag{3.26}$$

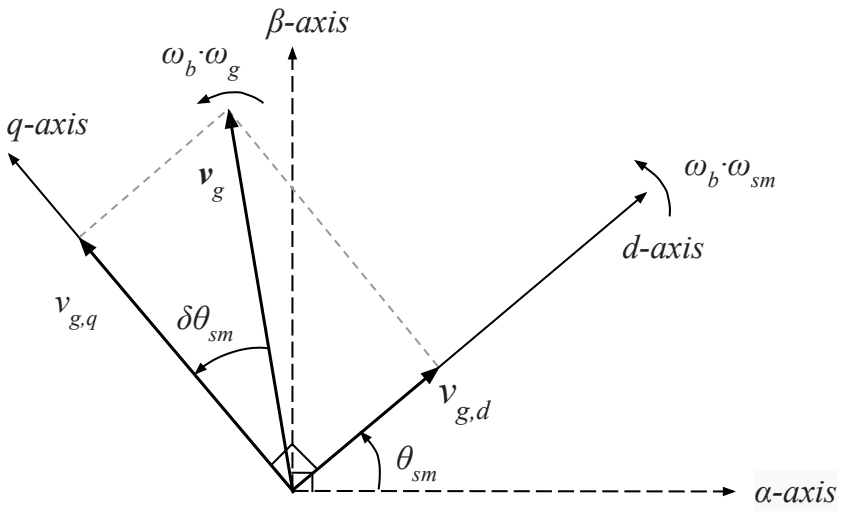

Figure 3.8: Vector diagram defining the SM SRRF and vector orientations.

$$\mathbf{u}_{sm} \triangleq [\, \hat{v}_{g,d} \quad \hat{v}_{g,q} \quad \omega_g \quad p^*_{sm} \quad q^*_{sm} \quad \omega^*_{sm} \quad \hat{v}^*_{sm} \,]^T \tag{3.27}$$

3.1.7 Small-signal model

The corresponding linearized small-signal-state-space model of the non-linear active load model, presented in 3.2.7, is derived on the form given by

$$\boldsymbol{\Delta}\dot{\mathbf{x}}_{sm} \triangleq \frac{\mathrm{d}}{\mathrm{d}t}\boldsymbol{\Delta}\mathbf{x}_{sm} = \mathbf{A}_{sm}\boldsymbol{\Delta}\mathbf{x}_{sm} + \mathbf{B}_{sm}\boldsymbol{\Delta}\mathbf{u}_{sm} \tag{3.28}$$

where the prefix $\boldsymbol{\Delta}$ denotes small-signal deviations around the steady-state operating point [38]. Moreover, the matrices $\mathbf{A}_{load}$ and $\mathbf{B}_{load}$ for the small-signal model can be found in Appendix B.2.

3.2 Active load

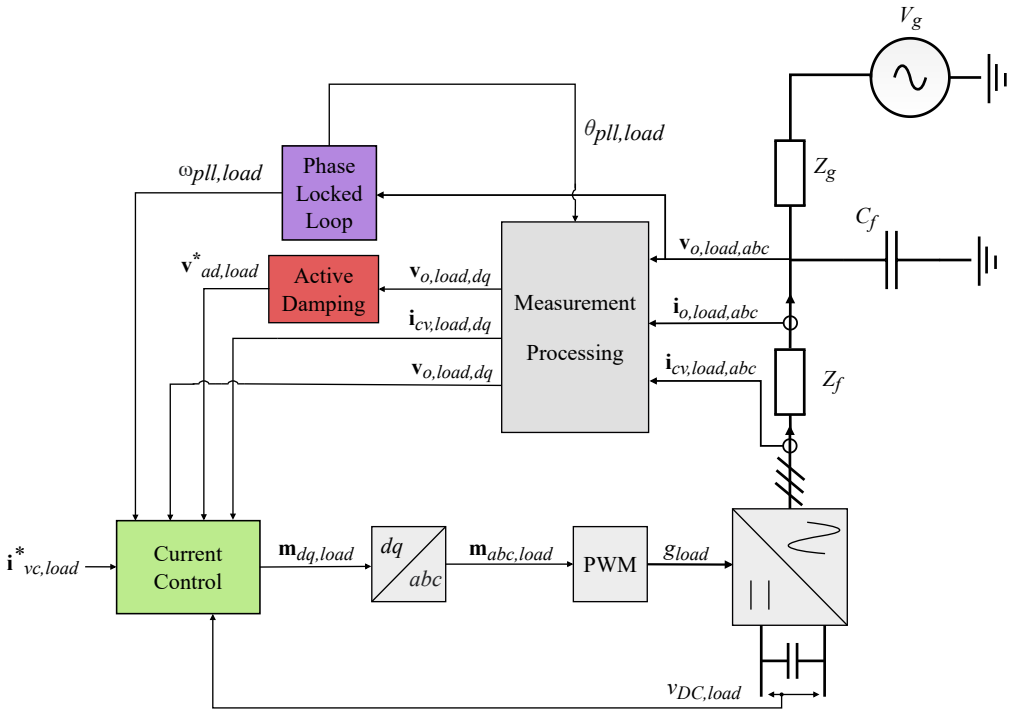

Figure 3.9: Overview of investigated system configuration and control structure for the active load.

Large dynamic loads in a marine power system demand significant changes in the supply within a short time. These large dynamic loads include propulsion motor drives, pumps, and fans that are controlled by power electronics. The most important dynamics of these loads can be modeled using an active load. This load is continuously drawing power from the ship grid and can quickly increase with no delay. The active load used for the hybrid ship power system is modeled as a three-phase voltage source converter (VSC) feeding a DC-bus with an ideal DC voltage source.

An overview of the active load control structure can be found in Figure 3.9. The VSC is synchronized to the grid using a PLL and the current drawn from the grid is controlled through a current controller. The VSC is connected to the grid through an LC filter. The switching effects of the VSC are neglected and an ideal average model is assumed for the modeling. The PLL calculates the position of the SRRF by measurements and the applied inner loop current controllers are conventional PI-controllers with decoupling terms [6].

3.2.1 Measurement processing

The Measurement Processing block supplies the measurements needed for the simulated active load. This is where the output active and reactive power, as well as the output voltage amplitude and need currents from the converter, are all calculated. The AC voltage and currents are transformed from the *abc*-frame to the *dq*-frame via Park transformation. The Phase angle, $\theta_{pll,load}$, is used as the transformation angle, with the *d*-axis aligned with the *a*-phase on the three-phase *abc*-side.

3.2.2 Electrical system equations

A set of filter inductors connected to the converter and a shunt capacitor bank representing the capacitance represents the capacitance of the LC filter. Together with a Thévenin equivalent of the grid, this represents the electrical system included in the model according to FIG. This incorporates the dynamic interaction between the VSC control system and the equivalent grid voltage in the model. Considering an instantaneous average model of the converter, the SRRF state-space equations of the electrical system are given by (3.1)-(3.3) [6, 15, 37, 34].

$$\frac{\mathrm{d}\mathbf{i}_{cv,load}}{\mathrm{d}t} = \frac{\omega_b}{l_f}\mathbf{v}_{cv} - \frac{\omega_b}{l_f}\mathbf{v}_o - \left[\frac{r_f\omega_b}{l_f} + \mathrm{j}\omega_b\omega_g\right]\mathbf{i}_{cv} \tag{3.1}$$

$$\frac{\mathrm{d}\mathbf{v}_{o,load}}{\mathrm{d}t} = \frac{\omega_b}{c_f}\mathbf{i}_{cv} - \frac{\omega_b}{c_f}\mathbf{i}_o - \mathrm{j}\omega_b\omega_g\mathbf{v}_o \tag{3.2}$$

$$\frac{\mathrm{d}\mathbf{i}_{o,load}}{\mathrm{d}t} = \frac{\omega_b}{l_g}\mathbf{v}_o - \frac{\omega_b}{l_g}\mathbf{v}_g - \left[\frac{r_g\omega_b}{l_g} + \mathrm{j}\omega_b\omega_g\right]\mathbf{i}_o \tag{3.3}$$

From equations (3.1)-(3.2) we have $\mathbf{v}_{o,load}$, the voltage over the filter capacitor, $\mathbf{i}_{cv,load}$, the current through the filter inductor, c_f, the filter capacitance, and l_f, the filter inductance. In equation (3.3) $\mathbf{i}_{o,load}$ represents the current flowing from grid to load, with l_g and r_g being the grid equivalent inductance and resistance respectively.

3.2.3 Phase locked loop ('PLL')

The active load is synchronized and connected to the grid; to achieve this a Phase Locked Loop (PLL) is used to detect the grid phase angle. Figure 3.10 show the structure of a commonly used PLL structure, based on [26, 27], that can be used for tracking the grid angular frequency, ω_g.

From the control structure in Figure 3.10, the PLL instantaneous phase voltage for the active load model, $\theta_{PLL,load}$, can be found and used to transformer the grid voltage measurements into the PLL-oriented SRRF. A first-order low-pass filter is used on the PLL SRRF voltage measurements for the active load, $\mathbf{v}_{pll,load}$. The states of the applied

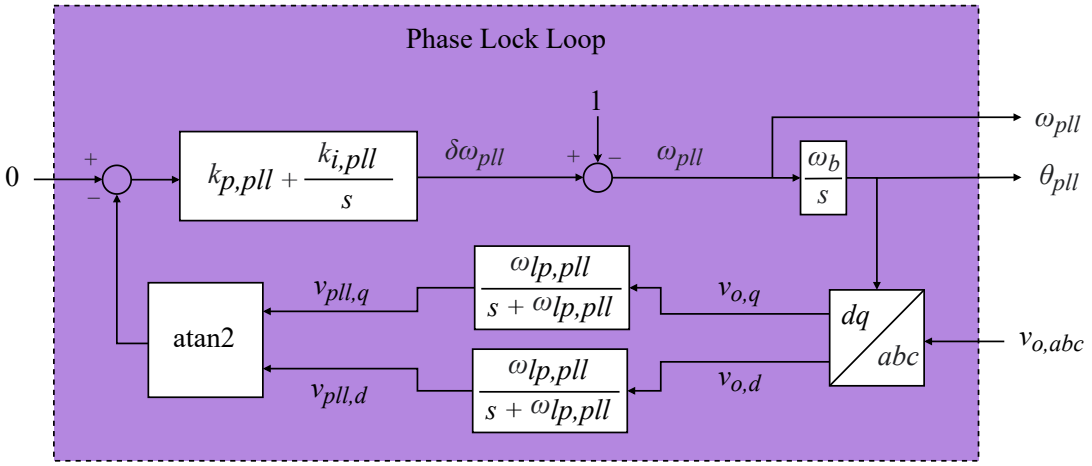

Figure 3.10: Control structure for a Phase Locked Loop ('PLL').

filter can be expressed by (3.4), where $\omega_{LP,PLL}$ is the cut-off frequency. An inverse tangent function is then used on to calculate the phase angle error $\varepsilon_{pll,load}$ (3.5). A PI-controller is used on the angular speed deviation, where k, pll is the proportional gain and $k_{i,pll}$ is the integral gain.

$$\frac{d\mathbf{v}_{pll,load}}{dt} = -\omega_{lp,pll} \cdot \mathbf{v}_{pll,load} + \omega_{lp,pll} \cdot \mathbf{v}_{o,load} \tag{3.4}$$

The integrator state ε of the PI-controller is defined as

$$\frac{\mathrm{d}\varepsilon_{pll,load}}{\mathrm{d}t} = \arctan\left[\frac{v_{pll,load,q}}{v_{pll,load,d}}\right] \tag{3.5}$$

A angular speed deviation $\delta\omega_{pll,load}$ with respect to the the grid angular frequency can be defined according to (3.6) with the corresponding phase angle displacement, $\delta\theta_{pll,load}$, of the active load PLL is then defined by (3.7).

$$\delta\omega_{pll,load} = k_{p,pll,load} \arctan\left[\frac{v_{pll,load,q}}{v_{pll,d}}\right] + k_{i,pll,load}\varepsilon_{pll,load} \tag{3.6}$$

$$\frac{\mathrm{d}\delta\theta_{pll,load}}{\mathrm{d}t} = \omega_b\delta\omega_{pll,load} \approx \omega_b\omega_{pll,load} - \omega_b \tag{3.7}$$

The actual per unit frequency $\omega_{pll,load}$ detected by the PLL is given by (3.8) and the phase angle used in the implementation of the active load PLL is defined by $\theta_{pll,load}$. The phase angle, $\theta_{pll,load}$ is used for the transformation of the measured three-phase voltage measurements into the PLL-oriented SRRF.

$$\omega_{pll,load} = \delta\omega_{pll,load} + \omega_g \approx \delta\omega_{pll,load} + 1 \tag{3.8}$$

$$\frac{\mathrm{d}\theta_{pll,load}}{\mathrm{d}t} = \omega_b\omega_{pll,load} \approx \omega_b\delta\omega_{pll,load} + \omega_b \tag{3.9}$$

3.2.4 Active damping

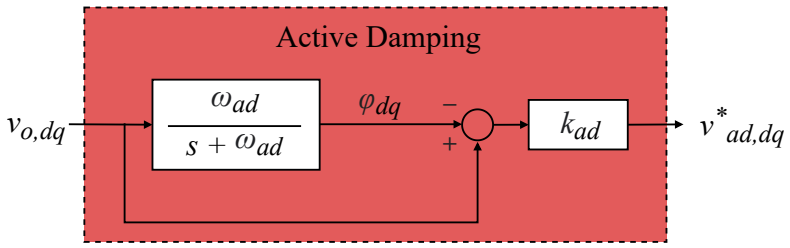

Figure 3.11: Control structure for a active damping algorithm.

An active damping term $v^*_{ad,load}$ is included in voltage reference, designed for suppressing LC oscillations in the filter [39]. The implementation of a commonly used active damping algorithm is shown in Figure 3.11, and is based on high pass filtering of the measured voltage $\mathbf{v_{o,load}}$, obtained from the difference between $\mathbf{v}_{o,load}$ and the low pass filtered value of the same voltage. As stated in equation (3.10), the resulting high pass filter is then scaled by the gain $k_{ad,load}$ and subtracted from the output the current controller, presented in 3.2.5, to cancel detected oscillations in the capacitor voltages.

$$\mathbf{v}^*_{ad,load} = k_{ad,load}\left(\mathbf{v}_{o,load} - \boldsymbol{\varphi}_{load}\right) \tag{3.10}$$

In (3.10), φ represent the internal states of the low pass filter used for the active damping and is defined in (3.11) where $\omega_{ad,load}$ is the cut-off frequency for active damping filter in the active load model.

$$\frac{d\boldsymbol{\varphi}_{load}}{dt} = \omega_{ad,load}\cdot\mathbf{v}_{o,load} - \omega_{ad,load}\cdot\boldsymbol{\varphi}_{load} \tag{3.11}$$

3.2.5 Current control

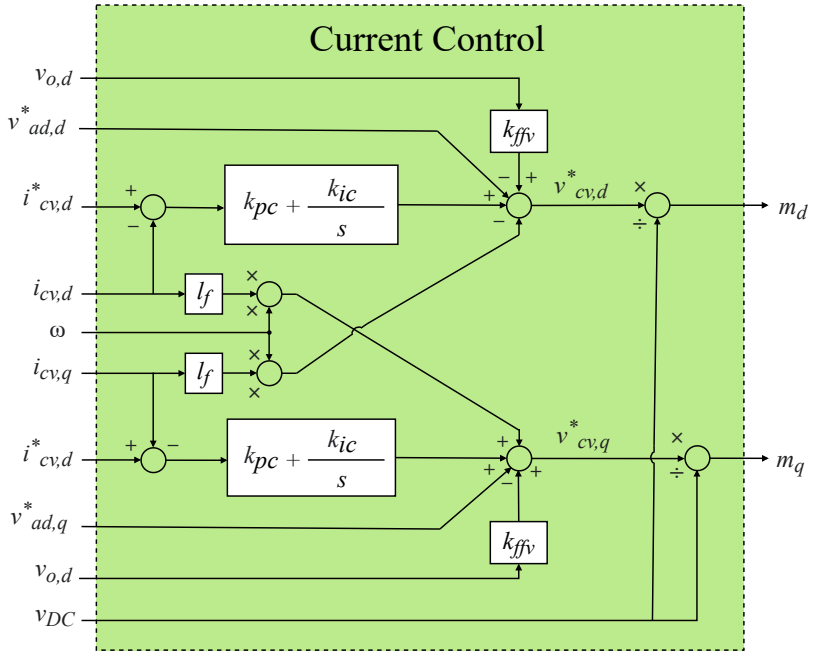

Figure 3.12: Control structure for the current control.

A common current controller is used for to control the the power drawn from the grid for the active load. The control structure consist of PI-controllers with decoupling terms as is illustrated in the Figure 3.12 [6, 15, 37, 34]. The output of the current controller is the voltage reference signal for the VSC, $\mathbf{v}^*_{cv,load}$ given by equation (3.12), where k_{pc} and k_{ic} are the PI controller proportinak and integral gains, respectively. The state $\boldsymbol{\gamma}_{load}$ represents the PI controller integrators and its equation is found in (3.13), k_{ffv} is the feed-forward gain, used for disabling or enabling the forward feeding of the measured output voltage $\mathbf{v}_{o,load}$.

$$\mathbf{v}^*_{cv,load} = k_{pc}\left[\mathbf{i}^*_{cv,load} - \mathbf{i}_{cv,load}\right] + k_{ic}\gamma_{load} + \mathrm{j}l_f\omega_g\mathbf{i}_{cv,load} + k_{ffv}\mathbf{v}_{o,load} - \mathbf{v}^*_{ad,load} \tag{3.12}$$

$$\boldsymbol{\gamma}_{load} = \mathbf{i}^*_{cv,load} - \mathbf{i}_{cv,load} \tag{3.13}$$

The reference $\mathbf{v}^*_{cv,load}$ is divided by the measured DC link voltage, $v_{DC,load}$, to produce the modulation index, $\mathbf{m}_{load}$, as in FIG. Neglecting the switching operations of the converter and any delay related to the PWM implementation, the instantaneous average value of the per unit converter output voltage, $\mathbf{v}_{cv,load}$, is given by the product of the modulation index, $\mathbf{m}_{load}$, and the measured DC-voltage, $v_{DC,load}$. Thus, the converter output voltage

will be decoupled from possible transients of the DC-side implying that the converter output voltage is equal to its reference value (3.1) [6, 15, 34].

$$\mathbf{m}_{load} = \frac{\mathbf{v}^*_{cv,load}}{v_{DC,load}}, \quad \mathbf{v}_{cv,load} = \mathbf{m}_{load} v_{DC,load} \quad \Rightarrow \quad \mathbf{v}_{cv,load} \approx \mathbf{v}^*_{cv,load} \tag{3.14}$$

3.2.6 Synchronous reference frame orientation ('SRRF')

The synchronization of the active load control system to the grid is based on the phase angle orientation of the PLL, and the phase angle $\theta_{pll,load}$ is used in the transformation between the stationary reference frame and the active load-oriented SRRF. Because the active load-oriented SRRF rotates at the same frequency as the grid voltage in a steady-state, the phase angle will continually increase between 0 and 2π, as illustrated in the vector diagram in Figure 3.19. As the vector diagram also indicates, the phase angle $\delta\theta_{pll,load}$, as defined by its definition, represents the phase difference between the active load SRRF orientation SRRF and the spinning grid voltage vector.

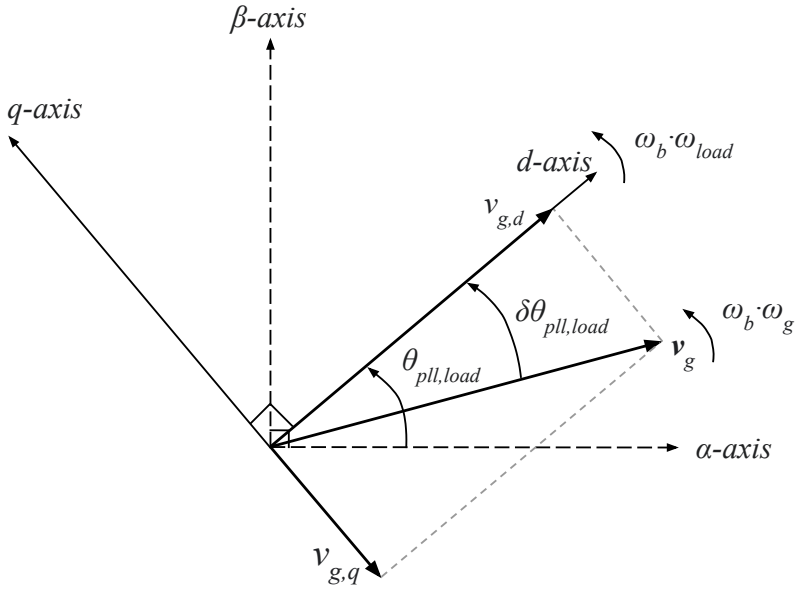

Figure 3.13: Vector diagram defining the active load SRRF and vector orientations.

3.2.7 Non-linear active load model in grid-connected operation

All equation need for the detaled modelling of the active load configuration in grid-connected operation have now been presented. The equations can be reduced down to a model on state-space form with 14 disticnt state variables and 5 input signals, with the

state vector $\mathbf{x}_{load}$ (3.15) and the input vector $\mathbf{u}_{load}$ (3.16). The resulting non-linear state space model of the overall system is given in Appendix B.1.

$$\begin{aligned}\mathbf{x}_{load} \triangleq [\, & i_{cv,load,d} \quad i_{cv,load,q} \quad v_{o,load,d} \quad v_{o,load,q} \quad i_{o,load,d} \quad i_{o,load,q} \quad \gamma_{load,d} \quad \cdots \\ & \cdots \quad \gamma_{load,q} \quad \varphi_{load,d} \quad \varphi_{load,q} \quad v_{pll,load,d} \quad v_{pll,load,q} \quad \varepsilon_{pll,load} \quad \delta\theta_{pll,load} \,]^T\end{aligned} \tag{3.15}$$

$$\mathbf{u}_{load} \triangleq \begin{bmatrix} \hat{i}^*_{cv,d} & \hat{i}^*_{cv,q} & \hat{v}_{g,d} & \hat{v}_{g,q} & \omega_g \end{bmatrix}^T \tag{3.16}$$

3.2.8 Small signal model of the active load

The corresponding linearized small-signal-state-space model of the non-linear active load model, presented in 3.2.7, is derived on the form given by

$$\mathbf{\Delta}\dot{\mathbf{x}}_{load} \triangleq \frac{\mathrm{d}}{\mathrm{d}t}\mathbf{\Delta}\mathbf{x}_{load} = \mathbf{A}_{load}\mathbf{\Delta}\mathbf{x}_{load} + \mathbf{B}_{load}\mathbf{\Delta}\mathbf{u}_{load} \tag{3.17}$$

where the prefix $\mathbf{\Delta}$ denotes small-signal deviations around the steady-state operating point [38]. Moreover, the matrices $\mathbf{A}_{load}$ and $\mathbf{B}_{load}$ for the small-signal model can be found in Appendix B.2.

3.3 Virtual synchronous machine

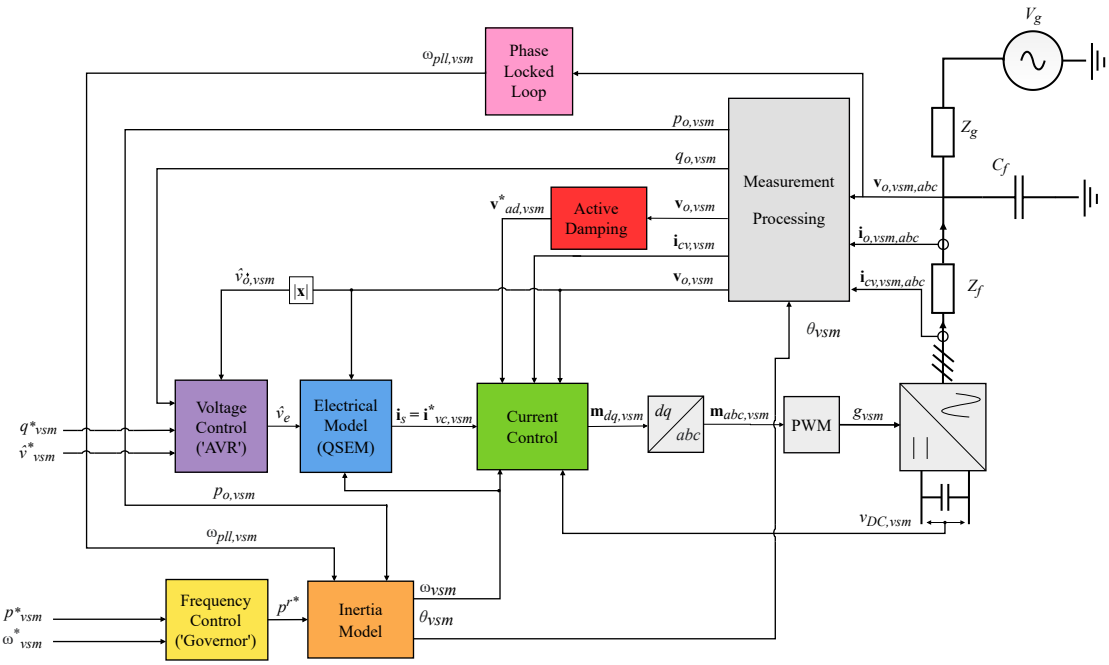

Figure 3.14: Overview of investigated system configuration and control structure for the virtual synchronous machine when connected to a stiff grid.

The model for the VSM for the hybrid ship power system was developed for the specialization project (TTK4550). It is an adaptation of the model presented in [34], but with a PLL implemented for damping in the virtual swing equation. A general overview of the VMS control system and the power configuration is presented in Figure 3.14. The inertia model block contains the simplified swing equation, while the frequency controller emulates the simplified behavior of a prime mover with its speed governor. The electrical model represents the stator windings and the voltage controller acts as the automatic voltage regulator ('AVR'). When modeling the VSM the DC voltage, $V_{DC,vsm}$ is assumed to have sufficient voltage, and therefore for the Matlab Simulink model: $V_{dc} > 2V_b$. An average model is used for the three-phase converter, meaning that as for the active load there is no need for a PWM. Any delay due to the PWM implementation can therefore be neglected. Furthermore, the input voltage reference signal for the three-phase converter can be assumed to approximately equal to the output voltage

$$\mathbf{m}_{dq,vsm} = \frac{\mathbf{v}^*_{cv,vsm}}{v_{DC,vsm}}, \quad \mathbf{v}_{cv,vsm} = \mathbf{m}_{dq,vsm} v_{DC,vsm} \quad \Rightarrow \quad \mathbf{v}_{cv,vsm} \approx \mathbf{v}^*_{cv,vsm} \tag{3.1}$$

and for this reason, the dynamics of the DC-side are not modeled.

3.3.1 Frequency control and inertia model

The VSM control structure for the frequency controller and the inertia model is found in Figure 3.15. The inertia model represents a linearized swing equation for an SM [34, 14, 50, 33]. The SM exhibits a damping torque nearly proportional to the difference between the grid angular frequency and the angular frequency given by the rotational speed of the SM. The grid frequency is made available for the inertia model from the PLL, and the gain, k_d, is used to emulate the damping that is found in a real SM and will be almost equivalent if the grid frequency changes relatively slowly compared to the dynamics of the emulated VSM speed. The equations (3.2) and (3.3) represent the state-space equations for the inertia model found in Figure 3.15.

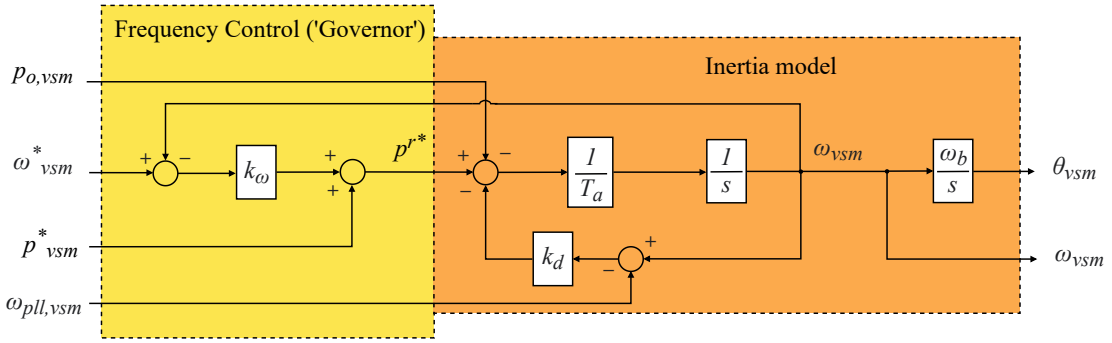

Figure 3.15: Frequency control ('Governor') and Inertia Model.

$$\frac{\mathrm{d}\omega_{vsm}}{\mathrm{d}t} = \frac{p^{r^*}}{T_a} - \frac{p_{o,vsm}}{T_a} - \frac{k_{d,vsm}\left[\omega_{vsm} - \omega_{pll,vsm}\right]}{T_a} \tag{3.2}$$

$$\frac{\mathrm{d}\theta_{vsm}}{\mathrm{d}t} \tag{3.3}$$

The variable p^{r^*} is the virtual power driving the inertia, $p_{o,vsm}$ is the measured power output to the grid, $\omega_{pll,vsm}$ is the measured grid angular frequency discussed in 3.3.5 and T_a is the virtual inertia time constant. The angle θ_{vsm} is the angle used for the SRRF transformation on the VSM, which is referred the phase angle of the grid voltage vector in the SRRF. The $\delta\theta_{vsm}$ given in (3.4) represents the deviation between the VSM virtual rotor position and the phase angle of the grid vector in the SRRF.

$$\frac{\mathrm{d}\delta\theta_{vsm}}{\mathrm{d}t} = \omega_b\omega_{vsm} - \omega_b\omega_g \tag{3.4}$$

The frequency control ('Governor'), indicated in Figure 3.14 is modeled as an ideal power source able to provide instantaneously the required power. p^{r*}, the power reference for the ideal prime mover is generated by a frequency droop regulator given in equation

(3.5). The power reference for the VSM is given as p_{vsm}, ω^*_{vsm} is the VSM frequency speed reference and the frequency droop gain is given as k_ω.

$$p^{r^*} = p^*_{vsm} - k_\omega \left[\omega_{vsm} - \omega^*_{vsm}\right] \tag{3.5}$$

3.3.2 Voltage controller with reactive power droop

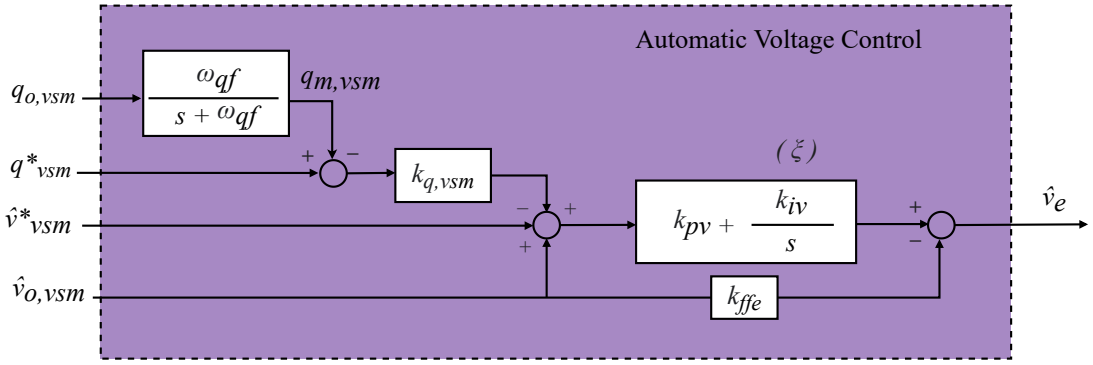

Figure 3.16: Automatic Voltage Controller with reactive power droop.

The voltage controller regulates the amplitude of the internally induced voltage $\hat{v}_e$ of the VSM electric model, to control the output voltage amplitude $\hat{v}_{o,vsm}$ of the VSM. The voltage controller is represented by the block labelled Voltage Control ('AVR') in Figure 3.14 and the control structure is illustrated in Figure 3.16. The internally induced voltage is calculated by

$$\hat{v}_e = k_{pv} \cdot (\hat{v}^*_{vsm} - \hat{v}_{o,vsm}) + k_{pv} \cdot k_{q,vsm} \left(q^*_{vsm} - q_{m,vsm}\right) + k_{iv} \cdot \xi + k_{ffe} \cdot \hat{v}_{o,vsm} \tag{3.6}$$

where $\hat{v}^*_{vsm}$ is the external voltage amplitude reference and q^*_{vsm} is the reactive power reference. The gain $k_{q,vsm}$ is the reactive power droop gain acting on the difference between the output reactive power measurement $q_{o,vsm}$ (3.7) and the reactive power reference for the VSM, q^*_{vsm}. A PI-controller is used for the voltage control, where ξ (3.8) represents the integral state of the controller.

$$\frac{\mathrm{d}q_{m,vsm}}{\mathrm{d}t} = \omega_{qf} q_{vsm} - \omega_{qf} q_{m,vsm} \tag{3.7}$$

$$\frac{d\xi}{dt} = (\hat{v}^*_{vsm} - \hat{v}_{o,vsm}) + k_q \left(q^*_{vsm} - q_{m,vsm}\right) \tag{3.8}$$

3.3.3 Virtual impedance (Electrical model)

The internally induced voltage from the voltage controller is used in the electrical model for the VSM-implementation. All VSM implementations include a presentation of an SM, executed in real-time to generate internal control references. The two dominating architectures depend on if the model provides a current reference or a voltage reference for the control of the converter [14]. For the chosen VSM implantation a current reference is used, and the electrical part of the internal SM model can therefore be represented with one of two models. Either as a dynamical electrical model (DEM) [5, 10, 11, 12, 24, 49] or as a quasi-stationary representation of the SM stator windings [25, 34, 42].

However, the DEM-based implementation has the disadvantage that it depends on a high value of the virtual stator resistance to avoid poorly dampened synchronous frequency resonance in the SRRF, which could lead to significant coupling between the active and reactive power control [34]. For that reason, the QSEM-implementation is chosen for the implementation of the VSM electrical model. The QSEm-implementation assumes an algebraic, i.e. phasor based representation of the SM stator impedance in the SRRF, and the stator currents can be represented as

$$\mathbf{i}_s = \frac{r_s\left(\mathbf{v}_e - \mathbf{v}_m\right)}{r_s^2 + \left(\omega_{vsm} l_s\right)^2} - j\frac{\omega_{vsm} l_s\left(\mathbf{v}_e - \mathbf{v}_m\right)}{r_s^2 + \left(\omega_{vsm} l_s\right)^2} \tag{3.9}$$

where $\mathbf{v}_m$ is the low pass filtered measurement of $\mathbf{v_{o,vsm}}$ with the crossover frequency ω_{vf}. The expression for $\mathbf{v}_m$ is given as

$$\frac{d\mathbf{v}_m}{dt} = \omega_{vf} \cdot \mathbf{v}_{o,vsm} - \omega_{vf} \cdot \mathbf{v}_m \tag{3.10}$$

3.3.4 Synchronous reference frame orientation ('SRRF')

The SRRF applied for control and modeling of the VSM-implementation is given by the angular position of the internally induced voltage, $\mathbf{v}_e$, as defined by the virtual inertia. In steady state, the VSM SRRF rotates with the same angular speed as the grid voltage. Hence, the virtual rotor phase angle of the VSM, θ_{sm}, continuously increases, as can be seen in Figure 3.17. The virtual internal voltage phase angle difference, $\delta\theta_{vsm}$, represents the phase difference between the VSM SRRF d-axis and the rotating grid voltage vector. Considering the amplitude of the equivalent grid voltage $\hat{v}_g$ to be known, the voltage vector $\mathbf{v}_g$ in the VSM-oriented SRRF can then be expressed by:

$$\mathbf{v}_g = \hat{\mathbf{v}}_g e^{-j(\theta_{vsm} - \theta_g)} = \hat{\mathbf{v}}_g e^{-j\delta\theta_{vsm}} \tag{3.11}$$

As previously stated a PLL was implemented to estimate the grid angular frequency used to implement the VSM damping effect. This PLL will establish its own SRRF aligned with the voltage vector $\mathbf{v}_{o,vsm}$ and the phase angle displacement of this PLL with respect

to the grid voltage can therefore be defined as $\delta\theta_{pll,vsm}$. The PLL-oriented SRRF and the stationary reference frame are found in Figure 3.17. The phase angle between the VSM SRRF and PLL SRRF is defined by the difference between the VSM and VSM PLL angles. When modeling the VSM PLL in its own reference frame, the voltage $\mathbf{v}_{o,vsm}$ can be transformed from the VMS SRRF to the VSM PLL SRRF by:

$$\mathbf{v}_{o,vsm}^{pll} = \mathbf{v}_{o,vsm}^{vsm} e^{-j\left(\delta\theta_{pll,vsm} - \delta\theta_{vsm}\right)} \tag{3.12}$$

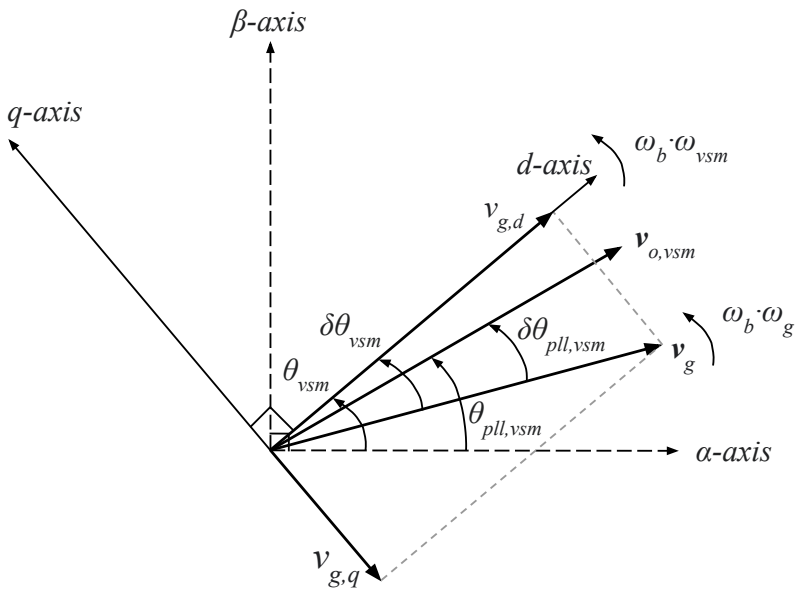

Figure 3.17: Vector diagram defining the VSM and VSM PLL SRRF with vector orientations.

3.3.5 Phase lock loop ('PLL')

The same PLL configuration as the active load is used for the VSM-implementation. The filtered voltages for the PLL are expressed in (3.13) where the same cut-off frequency $\omega_{lp,pll}$ as for the active load is used.

$$\frac{\mathrm{d}\mathbf{v}_{pll,vsm}}{\mathrm{d}t} = -\omega_{lp,pll}\mathbf{v}_{pll,vsm} + \omega_{lp,pll,vsm}\mathbf{v}_{o,vsm}^{pll} \tag{3.13}$$

The integrator state $\varepsilon_{pll,vsm}$ of the PI-controller is given as

$$\frac{\mathrm{d}\varepsilon_{pll,vsm}}{\mathrm{d}t} = \arctan\left[\frac{v_{pll,vsm,q}}{v_{pll,vsm,d}}\right] \tag{3.14}$$

The speed deviation $\delta\omega_{pll,vsm}$ with respect to the grid frequency is defined by (3.15) and the corresponding phase angle displacement, $\delta\theta_{pll,vsm}$ is defined by (3.16).

$$\delta\omega_{pll,vsm} = k_{p,pll,vsm} \arctan\left[\frac{v_{pll,vsm,q}}{v_{pll,vsm,d}}\right] + k_{i,pll,vsm}\varepsilon_{pll,vsm} \tag{3.15}$$

$$\frac{\mathrm{d}\delta\theta_{pll,vsm}}{\mathrm{d}t} = \omega_b \delta\omega_{pll,vsm} \tag{3.16}$$

3.3.6 Electrical system equations

Similar to the active load the electrical system included in the VSM model consists of a set of filter inductors connected to the three-phase inverter, a shunt capacitor bank representing the capacitance of the LC-filter, and a Thévenin equivalent of the grid. The equations (3.17)-(3.19) represent the SRRF state space of the electrical system for the VSM [15, 37, 38].

$$\frac{\mathrm{d}\mathbf{i}_{cv,vsm}}{\mathrm{d}t} = \frac{\omega_b}{l_f}\mathbf{v}_{cv,vsm} - \frac{\omega_b}{l_f}\mathbf{v}_o - \left[\frac{r_f\omega_b}{l_f} + \mathrm{j}\omega_b\omega_g\right]\mathbf{i}_{cv,vsm} \tag{3.17}$$

$$\frac{\mathrm{d}\mathbf{v}_{o,vsm}}{\mathrm{d}t} = \frac{\omega_b}{c_f}\mathbf{i}_{cv,vsm} - \frac{\omega_b}{c_f}\mathbf{i}_{o,vsm} - \mathrm{j}\omega_b\omega_g\mathbf{v}_{o,vsm} \tag{3.18}$$

$$\frac{\mathrm{d}\mathbf{i}_{o,vsm}}{\mathrm{d}t} = \frac{\omega_b}{l_g}\mathbf{v}_{o,vsm} - \frac{\omega_b}{l_g}\mathbf{v}_g - \left[\frac{r_g\omega_b}{l_g} + \mathrm{j}\omega_b\omega_g\right]\mathbf{i}_{o,vsm} \tag{3.19}$$

In the electrical system equations for the VSM, $\mathbf{v}_{cv,vsm}$ represent the converter output voltage, $\mathbf{i}_{cv,vsm}$ the filter inductor current, $\mathbf{v}_{o,vsm}$ the voltage at the filter capacitor and $\mathbf{v}_g$ the voltage of the stiff grid.

3.3.7 Current control and active damping

The current controller used for the VSM-implementation is the same as for the active load. Moreover, the output for the current controller in VSM-implementation is given as

$$\begin{aligned}\mathbf{v}^*_{cv,vsm} = k_{pc,vsm}\left[i^*_{cv,vsm} - i_{cv,vsm}\right] + k_{ic,vsm}\boldsymbol{\gamma}_{vsm} + \mathrm{j}l_f\omega_{vsm}\mathbf{i}_{cv,vsm} \\ + k_{ffv}\mathbf{v}_{o,vsm} - \mathbf{v}^*_{ad,vsm}\end{aligned} \tag{3.20}$$

where the state $\boldsymbol{\gamma}_{vsm}$ is defined to represent the integrates of the PI-controllers:

$$\frac{\mathrm{d}}{\mathrm{d}t}\boldsymbol{\gamma}_{vsm} = \mathbf{i}^*_{cv,vsm} - \mathbf{i}_{cv,vsm} \tag{3.21}$$

An active damping term (3.22) is also included in the voltage reference (3.3.7) for the VSM, to suppress LC oscillations in the filter. The equation (3.23) gives the state $\boldsymbol{\varphi}_{vsm}$ is used for the low pass filter in the active damping.

$$\frac{\mathrm{d}\boldsymbol{\varphi}_{vsm}}{\mathrm{d}t} = \omega_{ad,vsm}\mathbf{v}_{o,vsm} - \omega_{ad,vsm}\boldsymbol{\varphi}_{vsm} \tag{3.22}$$

$$\mathbf{v}^*_{ad,vsm} = k_{ad,vsm}\left[\mathbf{v}_{o,vsm} - \boldsymbol{\varphi}_{vsm}\right] \tag{3.23}$$

3.3.8 Non-linear model

The equations presented for the VSM-implementation has been reduced to a model on state-space form with 20 distinct state variables and 7 input signals. The states are represented by state vector $\mathbf{v}_{vsm}$ (3.24) and the inputs by the input vector $\mathbf{u}_{vsm}$ (3.25), and the full non-linear model can be found in Appendix C.1.

$$\begin{aligned}\mathbf{x}_{vsm} \triangleq [\, & i_{cv,vsm,d} \quad i_{cv,vsm,q} \quad v_{o,vsm,d} \quad v_{o,vsm,q} \quad i_{o,vsm,d} \quad i_{o,vsm,q} \quad \cdots \\ & \cdots \quad \gamma_{vsm,d} \quad \gamma_{vsm,q} \quad \varphi_{vsm,d} \quad \varphi_{vsm,q} \quad v_{m,d} \quad v_{m,q} \quad v_{pll,vsm,d} \quad \cdots \\ & \cdots \quad v_{pll,vsm,q} \quad \varepsilon_{pll,vsm} \quad \delta\theta_{pll,vsm} \quad \xi \quad q_{m,vsm} \quad \omega_{vsm} \quad \delta\theta_{vsm}]^T\end{aligned} \tag{3.24}$$

$$\mathbf{u}_{vsm} \triangleq [p^*_{vsm} \quad q^*_{vsm} \quad \hat{v}_{g,d} \quad \hat{v}_{g,q} \quad \hat{v}^*_{vsm} \quad \omega^*_{vsm} \quad \omega_g]^T \tag{3.25}$$

3.3.9 Small-signal model

As for the active load and SM, a linearized small-signal state space model has been derived, with the form given by (3.26), where the perfix Δ denotes small-signal deviations around the steady state operating point [38]. $\mathbf{A}_{vsm}$, the state matrix, and $\mathbf{B}_{vsm}$, the input matrix, can be found in Appendix C.2.

$$\boldsymbol{\Delta}\dot{\mathbf{x}}_{vsm} \triangleq \frac{\mathrm{d}}{\mathrm{d}t}\boldsymbol{\Delta}\mathbf{x}_{vsm} = \mathbf{A}_{vsm}\boldsymbol{\Delta}\mathbf{x}_{vsm} + \mathbf{B}_{vsm}\boldsymbol{\Delta}\mathbf{u}_{vsm} \tag{3.26}$$

3.4 Hybrid ship power system

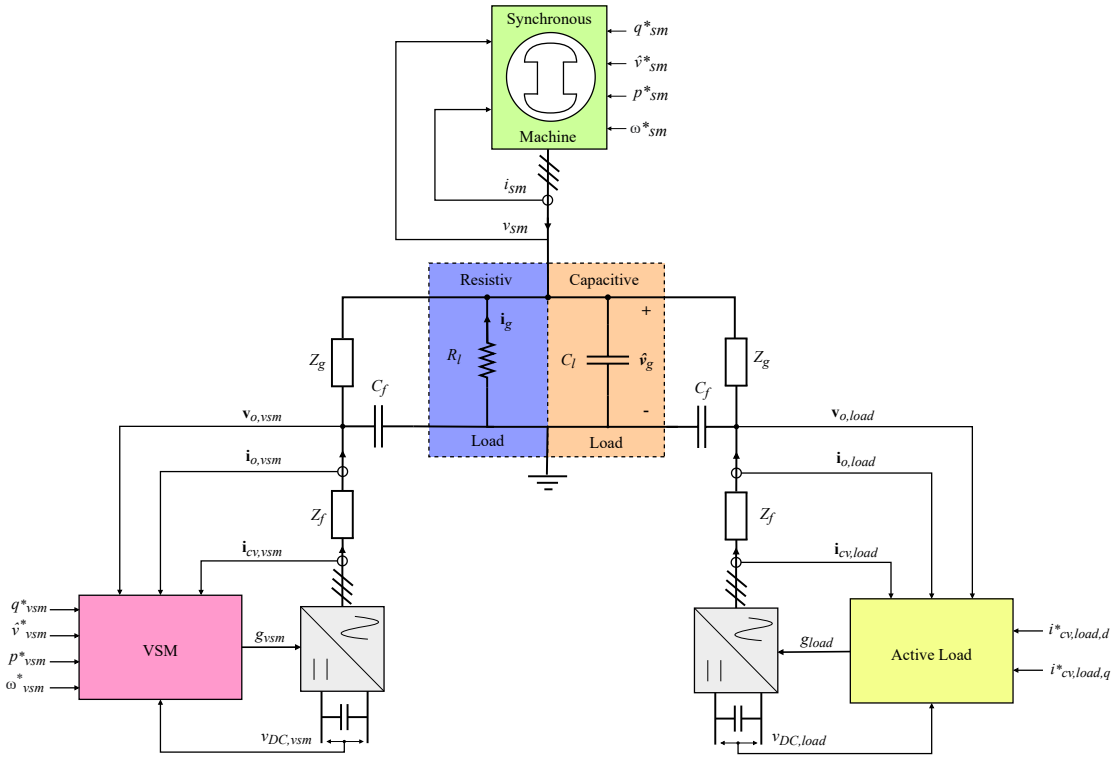

Figure 3.18: Overview of investigated system configuration and control structure for the hybrid ship power system.

The non-linear model of the hybrid ship power system of this thesis consists of the equations derived for the grid-connected SM, active load, and VSM. An overview of the power system can be seen in Figure 3.18. The VSM and the SM are the power generation of the power system, while the active load along with the resistor, r_l, and capacitor, c_l are the consumers.

When connecting the the three components together as one power system, the stiff grid that was previously modeled as an input for each system, is now introduced as the state (3.1). From Figure 3.18 we have the grid voltage, $\hat{\mathbf{v}}_g$, is the voltage at load capacitor, c_l, and the grid current, $\mathbf{v}_g$, is the current through the resistor load, r_l.

$$\frac{\mathrm{d}\hat{\mathbf{v}}_g}{\mathrm{d}t} = -\frac{\omega_b}{c_l}\mathbf{i}_g - j \cdot \omega_b \omega_{vsm} \mathbf{v}_g + \frac{\omega_b}{c_l}\mathbf{i}_{sm} + \frac{\omega_b}{c_l}\mathbf{i}_{o,\text{ load}} + \frac{\omega_b}{c_l}\mathbf{i}_{o,vsm} \tag{3.1}$$

3.4.1 Phase angle displacement

For the investigated hybrid ship power system, $\delta\theta_{sm}$ represents the phase angle displacement of the rotor in SM with respect to the VSM output voltage, as in equation (3.3). From equation (3.2), $\delta\theta_{pll,load}$, refers to the deviation between the virtual rotor position of the VSM, θ_{vsm}, and the phase angle displacement of the Load PLL, $\theta_{pll,load}$.

$$\frac{\mathrm{d}}{\mathrm{d}t}\delta\theta_{pll,load} = \omega_b\delta\omega_{pll,load} = \omega_b\omega_{pll,load} - \omega_b\omega_{sm} \tag{3.2}$$

$$\frac{\mathrm{d}}{\mathrm{d}t}\delta\theta_{vsm} = \omega_b\delta\omega_{sm} = \omega_b\omega_{sm} - \omega_b\omega_{sm} \tag{3.3}$$

$$\frac{\mathrm{d}}{\mathrm{d}t}\delta\theta_{pll,vsm} = \omega_b\delta\omega_{pll,vsm} = \omega_b\omega_{pll,sm} - \omega_b\omega_{sm} \tag{3.4}$$

3.4.2 Synchronous reference frame orientation ('SRRF')

When designing the state-space model for the hybrid ship power system, the virtual rotor position of the VSM, θ_{vsm}, is chosen as the reference for the SRRF. This result in the elimination of the virtual internal voltage phase difference, $\delta\theta_{vsm}$, that represented the displacement from the grid phase in the grid-connected VSM model. In steady-state, the load PLL angle, $\theta_{pll,load}$, and SM rotor angle, θ_{sm}, will both rotate with the same angular speed as the VSM voltage.

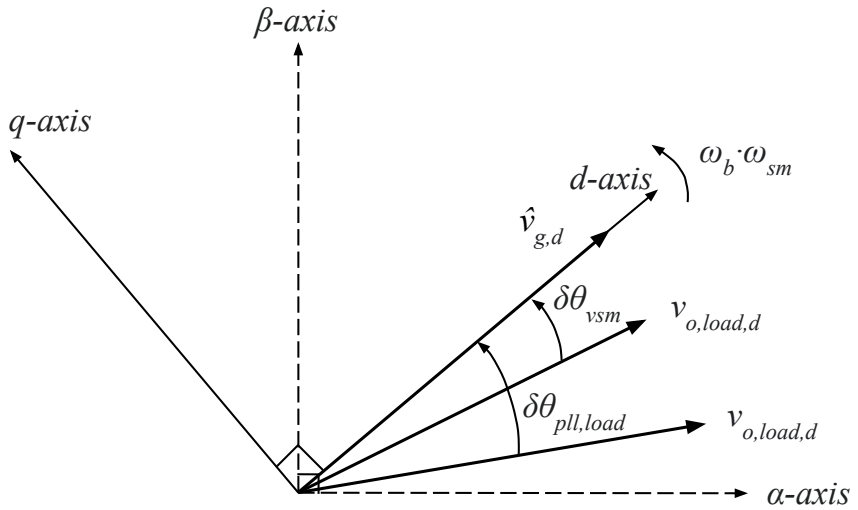

Figure 3.19: Vector diagram defining the ship grid SRRF and vector orientations.

3.4.3 Non-linear model

All equations needed for detailed modeling of the marine power system configuration have been presented in the previous three sub-section, and have been reduced to a model on state-space form with 46 distinct state variables and 10 input signals, with the state vector $\mathbf{x}_{sys}$ (3.5) and the input vector $\mathbf{u}_{sys}$ (3.6).

$$\begin{aligned}\mathbf{x}_{sys} \triangleq [\ & i_{cv,vsm,d} \quad i_{cv,vsm,q} \quad v_{o,vsm,d} \quad v_{o,vsm,q} \quad i_{o,vsm,d} \quad i_{o,vsm,q} \quad \gamma_{vsm,d} \quad \cdots \\ & \cdots \quad \gamma_{vsm,q} \quad \varphi_{vsm,d} \quad \varphi_{vsm,q} \quad v_{m,d} \quad v_{m,q} \quad v_{pll,vsm,d} \quad v_{pll,vsm,q} \quad \cdots \\ & \cdots \quad \varepsilon_{pll,vsm} \quad \delta\theta_{pll,vsm} \quad \xi \quad q_{m,vsm} \quad \omega_{vsm} \quad \delta\theta_{vsm} \quad i_{sm,d} \quad i_{sm,q} \quad \cdots \\ & \cdots \quad i_{fd} \quad i_{1d} \quad i_{1q} \quad \omega_{sm} \quad p_{sm} \quad q_{sm} \quad \zeta \quad v_{fd} \quad i_{cv,load,d} \quad i_{cv,load,q} \quad \cdots \\ & \cdots \quad \gamma_{load,d} \quad \gamma_{load,q} \quad \varphi_{load,d} \quad \varphi_{load,q} \quad v_{o,load,d} \quad v_{o,load,q} \quad i_{o,load,d} \quad \cdots \\ & \cdots \quad i_{o,load,q} \quad v_{pll,load,d} \quad v_{pll,load,q} \quad \varepsilon_{pll,load} \quad \delta\theta_{pll,load} \quad \hat{v}_{g,d} \quad \hat{v}_{g,q} \ ]^T\end{aligned} \tag{3.5}$$

$$\mathbf{u}_{sys} \triangleq \left[\ p^*_{vsm} \quad q^*_{vsm} \quad \hat{v}^*_{vsm} \quad \omega^*_{vsm} \quad i^*_{cv,load,d} \quad i^*_{cv,load,q} \quad p^*_{sm} \quad q^*_{sm} \quad \omega^*_{sm} \quad \hat{v}^*_{sm} \ \right]^T \tag{3.6}$$

New state variables

As stated previously the new state variable introduced is the d and q-axis grid voltages

$$\begin{aligned}\frac{\mathrm{d}\hat{v}_{g,d}}{\mathrm{d}t} = & -\frac{\omega_b}{c_l r_l}\hat{v}_{g,d} - \omega_b\omega_{sm}\hat{v}_{g,q} + \frac{\omega_b}{c_l}i_{o,vsm,d} - \frac{\omega_b}{c_l}i_{o,load,d}\sin\left(\delta\theta_{load}\right) \\ & + \frac{\omega_b}{c_l}i_{o,load,q}\cos\left(\delta\theta_{load}\right) + \frac{\omega_b}{c_l}i_{vsm,d}\sin\left(\delta\theta_{vsm}\right) - \frac{\omega_b}{c_l}i_{vsm,q}\cos\left(\delta\theta_{vsm}\right)\end{aligned} \tag{3.7}$$

$$\begin{aligned}\frac{\mathrm{d}\hat{v}_{g,d}}{\mathrm{d}t} = & -\frac{\omega_b}{c_l r_l}\hat{v}_{g,q} + \omega_b\omega_{sm}\hat{v}_{g,d} + \frac{\omega_b}{c_l}i_{o,vsm,q} - \frac{\omega_b}{c_l}i_{o,load,d}\cos\left(\delta\theta_{load}\right) \\ & - \frac{\omega_b}{c_l}i_{o,load,q}\sin\left(\delta\theta_{load}\right) + \frac{\omega_b}{c_l}i_{vsm,d}\cos\left(\delta\theta_{vsm}\right) + \frac{\omega_b}{c_l}i_{vsm,q}\sin\left(\delta\theta_{vsm}\right)\end{aligned} \tag{3.8}$$

The states $\delta\theta_{pll,load}$, $\delta\theta_{vsm}$ and $\delta\theta_{vsm}$ has been altered for the new power system. And for all other states where the variable ω_g is included in the equation is has been swapped with ω_{sm}. Apart from these changes in the equations of state variables from the grid-connected components, all of the states used for the hybrid ship power systems have stayed unchanged when connected together.

3.4.4 Small-signal model

Classic stability assessment techniques based on eigenvalues are not directly applicable to the non-linear state-space model and a linearized space model has been derived.

$$\boldsymbol{\Delta}\dot{\mathbf{x}}_{sys} \triangleq \frac{\mathrm{d}}{\mathrm{d}t}\boldsymbol{\Delta}\mathbf{x}_{sys} = \mathbf{A}_{sys}\boldsymbol{\Delta}\mathbf{x}_{sys} + \mathbf{B}_{sya}\boldsymbol{\Delta}\mathbf{u}_{sys} \tag{3.9}$$

Chapter 4

Model verification

The electrical (non-linear) models of the investigated systems and their corresponding small-signal (linearized) state-space models have been implemented in MATLAB Simulink. The Simscape Electrical block set was used to model the electrical systems. For the SM, a Synchronous Machine pu Fundamental block is utilized with a salient pole rotor type. In the case of VSM systems, the controllable voltage source module represents an ideal average three-phase voltage source converter (VSC) model.

A base case is defined for each unit of the hybrid ship power system. The SM is presented by the general model, where the damping circuit is considered and the damping factor, $k_{d,sm}$, is set to zero. The base case parameters and initial inputs for the SM are given in Table 4.1. The active load and virtual synchronous machine (VSM) base case parameters and the initial inputs are as indicated in Table 4.2 and Table 4.3 respectively. Table 4.4 includes static load parameters for the hybrid ship power system as well as the initial input values. For the SM, only the parameters related to the PI controllers and filters are assumed tunable. For the VSM however, only the five parameters related to the electrical system are presumed to be fixed.

As stated previously the SM, active load, and VSM were initially modeled connected to a stiff grid, and their small-signal models were validated before the units were combined to become the hybrid ship power system. Furthermore, to validate the small-signal models, the responses to different operating situations have been verified to match those of the electrical (non-linear) models around the linearization points. Numerical simulations of various digital time steps were performed at different steady-state operating points. The next four subsections present some of the results of the simulation cases for the SM, active load, VSM, and finally the complete hybrid ship power system.

The SM, VSM, and complete hybrid ship power system have all been simulated with a step-change in the power reference so that the results can be compared. For the SM and VSM, results for grid disturbances have also been presented. The results from a simulation of the active load for a change in active load drawn from the grid are also

Table 4.1: Table containing the base case synchronous machine system parameters and inputs.

Parameter	Value	Parameter	Value	Parameter	Value
S_{rated}	2.749MVA	l_{aq}	0.5249 pu	$k_{d,sm}$	0.0
V_{rated}	690 $V_{\text{rms,L-L}}$	l_{ad}	1.2285 pu	$k_{q,sm}$	0.4
ω_b	100π rad/s	l_{11d}	1.5455 pu	T_{gt}	0.5 s
r_a	0.0044 pu	l_{f1d}	1.2287 pu	$k_{\omega,sm}$	15
r_{fd}	9.3236×10^{-4} pu	l_{11q}	1.8392 pu	$\omega_{f,sm}$	1000 rad/s
r_{1q}	0.0314 pu	l_l	0.06 pu	T_{sm}	2 s
r_{1d}	0.0415 pu	$k_{p,ex}$	0.0259	T_{ex}	0.1 s
l_{ffd}	1.4993 pu	$k_{i,ex}$	0.0075		
Variable	Value	Variable	Value	Variable	Value
p^*_{sm}	0.50 pu	ω^*_{sm}	1.0 pu	$\hat{v}_{g,d}$	1.0 pu
q^*_{sm}	0.0 pu	ω_g	1.0 pu	$\hat{v}_{g,q}$	0.0 pu
$\hat{v}^*_{sm}$	1.0 pu				

Table 4.2: Table containing the base case active load system parameters and inputs.

Parameters	Value	Par.	Value	Parameters	Value
S_{rated}	2.749MVA	l_f	0.08pu	$\omega_{ad,load}$	50rad/s
V_{rated}	690 $V_{\text{rms,L-L}}$	c_f	0.074pu	k_{ffv}	0.0
ω_b	100πrad/s	$k_{pc,load}$	1.2732	$k_{i,pll,load}$	9.3800
r_g	0.01pu	$k_{ic,load}$	15.0	$k_{p,pll,load}$	0.1596
l_g	0.2pu	$k_{ad,load}$	1.5	$\omega_{lp,pll}$	1000rad/s
r_f	0.003pu				
Var.	Value	Var.	Value	Var.	Value
$i^*_{cv,load,d}$	-0.5pu	$\hat{v}_{g,d}$	1.0pu	ω_g	1.0pu
$i^*_{cv,load,q}$	0.0pu	$\hat{v}_{g,q}$	0.0pu		

presented. For the hybrid ship power system, the response of the system to an increased active power is carefully reviewed as well as the result from a change in the angular frequency reference for the SM. The behavior of each of the models is discussed, and any inconsistency between the electrical simulation and the small-signal model is commented on.

Table 4.3: Table containing the base case virtual synchronous machine system parameters and inputs.

Parameters	Value	Par.	Value	Parameters	Value
S_{rated}	2.749MVA	k_d	40	$k_{ad,vsm}$	1.5
V_{rated}	690 $V_{\text{rms,L-L}}$	k_ω	20	$\omega_{ad,vsm}$	50rad/s
ω_b	100πrad/s	$l_{s,vsm}$	0.25pu	k_{pv}	0.29
r_g	0.01pu	$r_{s,vsm}$	0.01pu	k_{iv}	92
l_g	0.2pu	$\omega_{vf,vsm}$	1200rad/s	ω_{qf}	200rad/s
r_f	0.003pu	$k_{pc,vsm}$	1.27	$k_{q,vsm}$	0.1
l_f	0.08pu	$k_{ic,vsm}$	15	$k_{i,pll,vsm}$	9.3800
c_f	0.074pu	k_{ffv}	0.0	$k_{p,pll,vsm}$	0.1596
T_a	4.0 s	k_{ffe}	0.0	$\omega_{lp,pll}$	1000rad/s
Var.	Value	Var.	Value	Var.	Value
p^*_{vsm}	0.5pu	ω^*	1.0pu	$\hat{v}_{g,d}$	1.0pu
q^*_{vsm}	0.0pu	ω_g	1.0pu	$\hat{v}_{g,q}$	0.0pu
$\hat{v}^*$	1.0pu				

Table 4.4: Table containing the base case hybrid ship power system parameters and inputs.

Parameters	Value	Paramter	Value	Parameters	Value
S_{rated}	2.749MVA	c_l	$5 \cdot 10^{-5}$pu		
V_{rated}	690 $V_{\text{rms,L-L}}$	r_l	2.0pu		
Variable	Value	Variable	Value	Variable	Value
p^*_{vsm}	0.5pu	p^*_{sm}	0.25pu	$i^*_{cv,load,d}$	-0.5pu
q^*_{vsm}	0.0pu	q^*_{sm}	0.0pu	$i^*_{cv,load,q}$	0.0pu
$\hat{v}^*_{vsm}$	1.0pu	$\hat{v}^*_{sm}$	1.0pu		
ω_{vsm}	1.0pu	ω_{sm}	1.0pu		

4.1 Synchronous machine

In the initial simulating case, the dynamic response of the SM is examined for a perturbation in the active power reference input, p^*_{sm}, from 0.5 pu to 0.6 pu for 4 second with the parameter and input values found in Table 4.1. The power reference and the resulting electrical power, p_{sm}, from the SM, are illustrated in the top graph in Figure 4.1, where it shows that the SM with the selected parameters exhibits a good transient response and reaches the steady within 2 seconds accompanied by some oscillation. The bottom plots in Figure 4.1 show that the step change in active power reference triggers a dynamic response in the angular frequency of the rotor, ω_{sm}, as well as an increase in the angular deviation, $\delta\theta_{sm}$, between the SM SRRF and the grid voltage vector that settles as the output power reaches the desired value.

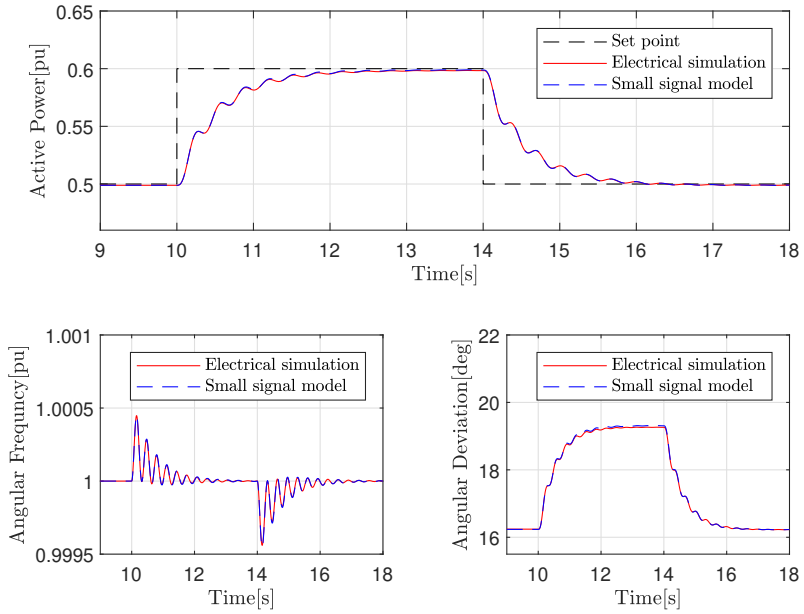

Figure 4.1: Simulation results for a perturbation of 0.1 pu in the active power reference for the SM, p^*_{sm}. Figure shows the response for the SM active power output, the angular frequency of the rotor and the SM SRRF angular deviation from the grid voltage.

Figure 4.2 shows the dynamic response of the SM system to a 4 seconds disturbance in the form of a 0.01 pu step change in the grid angular frequency, ω_g, with the parameter and input values found in Table 4.1. In response to the change in grid frequency, the active power control decreases the active power output to contribute to the system frequency control. This response is illustrated in the bottom left plot. The plot on top in Figure 4.2 shows the response of the rotor frequency, ω_{sm}, of the SM. About two seconds after the step, as the angular frequency reaches a steady-state, a small difference in the electrical simulation and small-signal model response can be noticed. When the grid frequency steps back to its initial value at 14s the response of the small-signal model and electrical (non-linear) model corresponds, and no deviation can be seen. The difference observed after the first step is anticipated to be the result of the non-linear elements of the electrical simulation that are not present in the small-signal model. The same small deviations can be found in the plot for the active power of the SM in the bottom left of Figure 4.2 and in the plot of the SM SRRF angular deviation from the grid voltage in the bottom right of Figure 4.2.

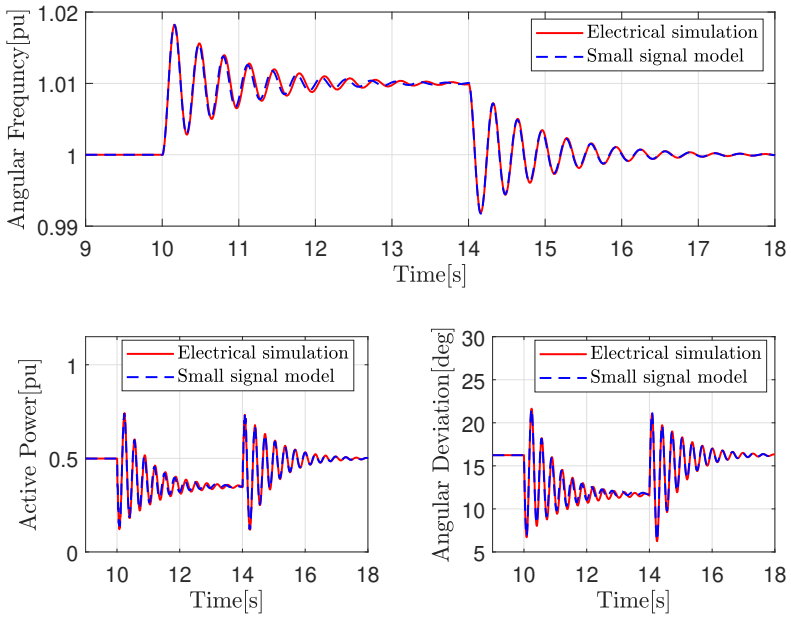

Figure 4.2: Simulation results for a 0.01 pu perturbation in grid frequency. The figure shows the response of the SM rotor angular frequency, the SM active power output and the SM SRRF angular deviation from the grid voltage vector.

4.2 Active load

For the electricity-consuming unit of the hybrid ship power system, a step in the d-axis current reference for the current controller was simulated as the unit was connected to a stiff grid with the parameter and input values found in Table 4.2. Figure 4.3 show the dynamic response of the active load 0.25 pu step down (from -0.5 pu to -0.75 pu) in the d-axis filter current reference, $i^*_{cv,load,d}$, occurs. This results in a 0.25 pu increase in active power being drawn for the grid as well as a change in the angular deviation of the active load SRRF from the grid voltage vector. As illustrated in Figure 4.3 there is practically no difference in the response of the small-signal model and the electrical model for the active load. Meaning that the presented small-signal model for the active load is a good fit for the electrical model.

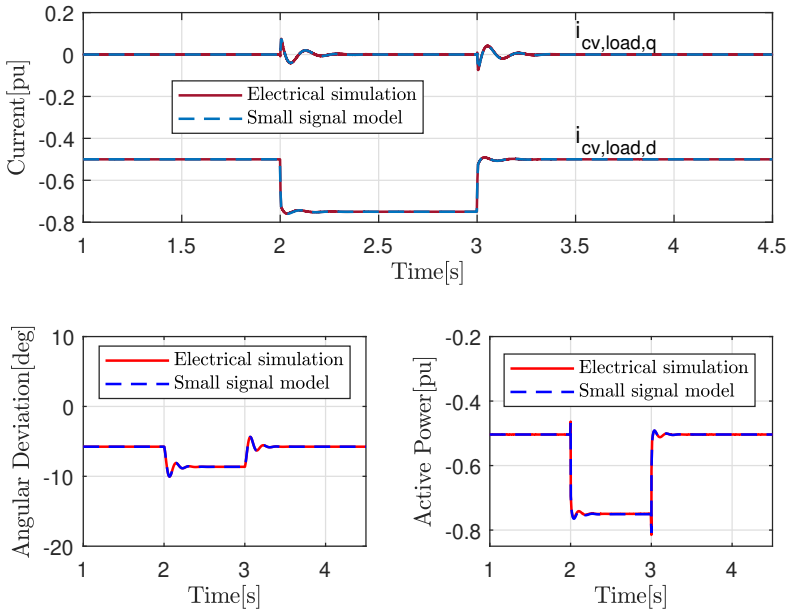

Figure 4.3: Simulation results for a 1 second 0.1 pu step change in d-axis filter current reference for the active load. Figure presents the response of the d and q-axis filter currents of the active load, the active load SRRF angular deviation from the voltage grid vector and the active power output of the active load.

4.3 Virtual synchronous machine

As for the SM, the initial simulation presents the dynamic response for a step in the power reference input, p^*_{vsm}, for the VSM from 0.5 pu to 0.6 pu. with the parameter and input values found in Table 4.3. The power reference and the resulting electrical power, p_{vsm}, from the VSM are both shown in the top plot in Figure 4.4. The step-change in the reference triggers a dynamic response in the rotating speed of the virtual inertia, as to be seen in the bottom left plot in Figure 4.4. The excess power input accumulated in the virtual inertia of the VSM, result in an increase in angular speed during the first part of the transient. This leads to an increase in the phase angle between the VSM SRRF and the grid voltage vector, as illustrated in the bottom right plot in Figure 4.4. Furthermore, the phase shift increases for as long the electrical power output from the VSM deviates from its power reference input. As for the rotational speed of the SM, the rotational speed of virtual inertia returns to the synchronous speed of the grid when the steady-state power balance of the system is restored.

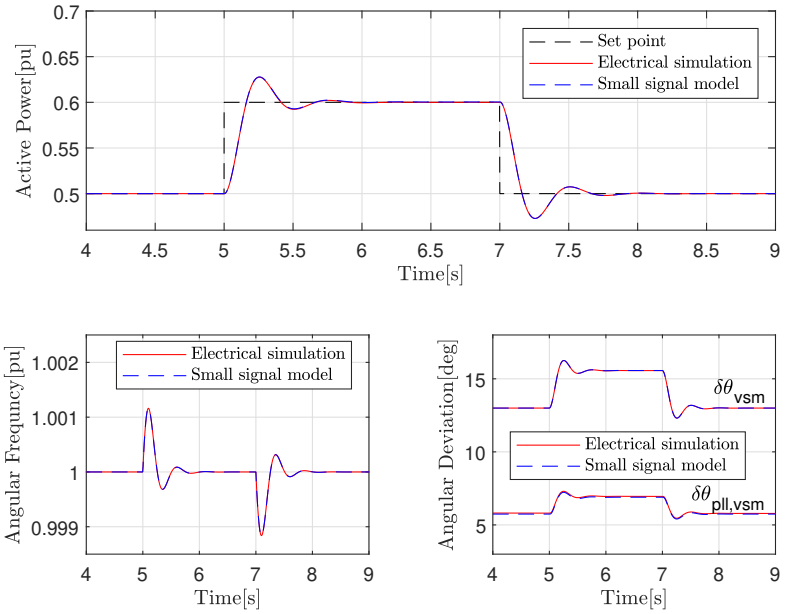

Figure 4.4: Simulation results for a perturbation of 0.1 pu in the active power reference for the VSM, p^*_{vsm}. Figure shows the response for the VSM active power output, the angular frequency of the rotor and the VSM SRRF angular deviation from the grid voltage.

The dynamic response of the SM system to a 0.01 step in the d-axis grid voltage, $\hat{v}_{g,d}$, with the parameter and input values found in Table 4.3, is shown in Figure 4.5. In the left panel, is the VSM reactive power output, q_{vsm}, response, while the angular deviation between the VSM SRRF and grid voltage, $\delta\theta_{vsm}$, is plotted on the right panel. When studying the zoomed-in transient of the reactive power response we can observe a slight deviation of the electrical and small-signal model. This deviation is anticipated to be the result of the non-linearity of the electrical model, and it will be present for all linearized models but more visible in some cases. In response to the voltage change in the grid, the reactive power control of the VSM decreases the reactive power output and contributes to the voltage control. The right panel is the angular difference between the VSM SRRF and the grid voltage vector. When studied it can be observed that angle changes with less than 0.1°, displaying that the active power output of the VSM is not affected by the change in grid voltage and that there is a clear decoupling between the active and reactive power.

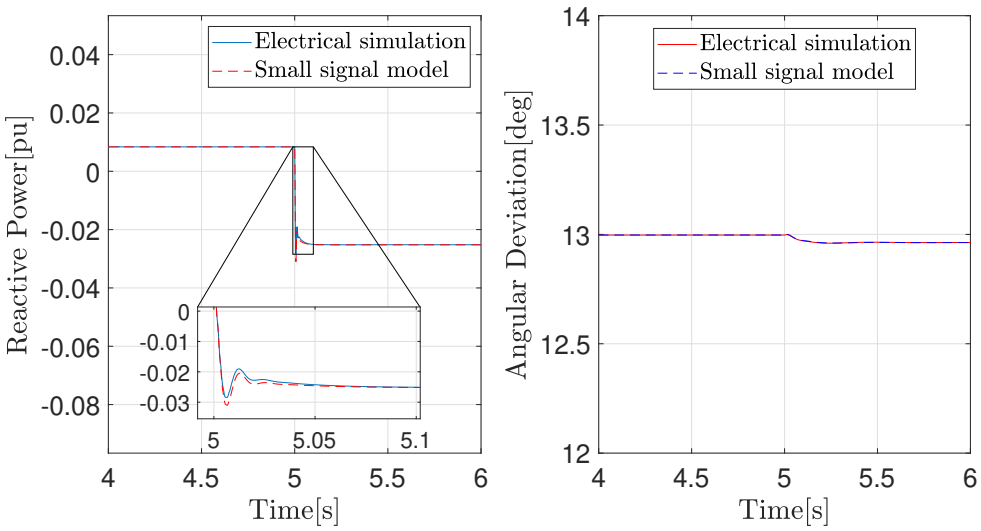

Figure 4.5: Simulation results of a 0.01 pu step in grid frequency. The figure shows response of VSM reactive power output and the VSM SRRF angular deviation from the grid voltage vector.

4.4 Hybrid ship power system

Lastly, the dynamic response of the hybrid ship power system is resented. The parameter values utiliized when simulating are given in table 4.1-4.4. Similar simulations scenarios as for the SM, VSM and active load are presented, showing the dynamics of the three units together in one isolated grid. The initial simulation presented is the performance of the VSM in the hybrid ship power system. Equivalently to the grid-connected VSM, a change in power reference of the VSM in the hybrid ship power system simulated. The dynamic response for all three units to a change in active load are presented. To finish of the model verification, the response to a disturbance in the power system reference angular frequency is presented.

Figure 4.6 the dynamic response of the VSM in the hybrid ship power system a change in the active power reference of the VSM, p^*_{vsm}, takes place. The settling time and the frequency of oscillation is different from that of stiff grid connected VSM response, and the response clearly some coupling between the states of the three units, as was expected. However, the electrical simulation and the small-signal model response match, and the repons of the VSM virtual rotor angular frequency (bottom left) and response of the angular deviation between the VSM SRRF and grid vector is as expected.

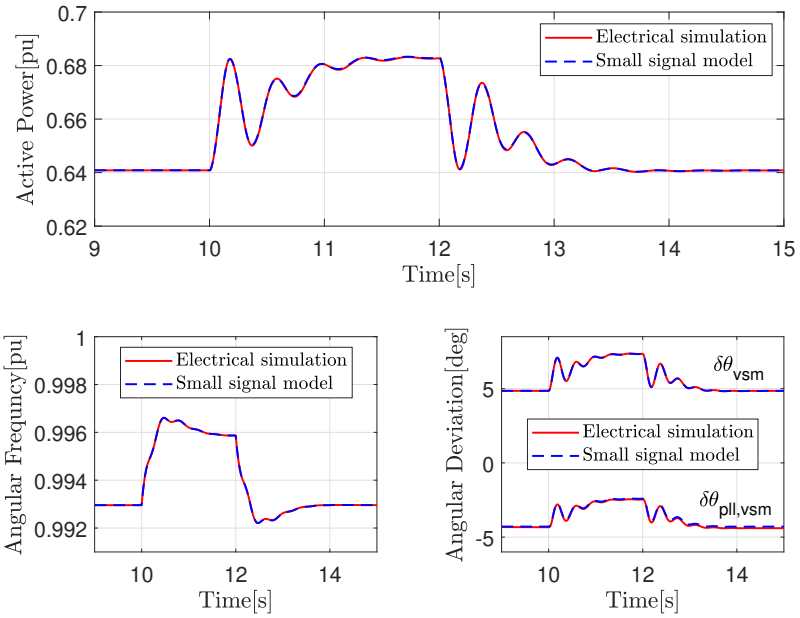

Figure 4.6: Simulation results for a 0.1 pu step in the active power reference for the VSM The figure shows the response of the VSM active power output, VSM virtual rotor angular frequency and VSM SRRF angular deviation from the grid voltage vector.

Figure 4.7-4.9 shows the response that can be observed for a relatively large increase in active power for the hybrid ship power system. This increase can be equivalent to an motor for ship propulsion in operation. Figure 4.7 shows that the dynamic response of the active load is similar to that of the grid-connected active load. However, there is a different frequency of oscillation and a slower settling time is observed. This is likely related to the power and frequency response of the SM. Some deviation between the electrical simulation and small-signal model can be observed in the active power response of the active load closely after the step in the d-axis reference of the active load.

The angular frequency and current response of the VSM and SM is illustrated in Figure 4.8 and 4.9 respectively. From the response we can see a almost identical decrease in angular speed for the VSM and SM. This demonstrates the VSM capabilities to act as a spinning reserve, and less need for having generators in operation (as spinning reserves). It can also be seen that the SM currents has more a prominent frequency of oscillations than of the VSM, but the settling time of the currents is identical. These oscillations where also more prominent for the grid-connected SM model than for the VSM.

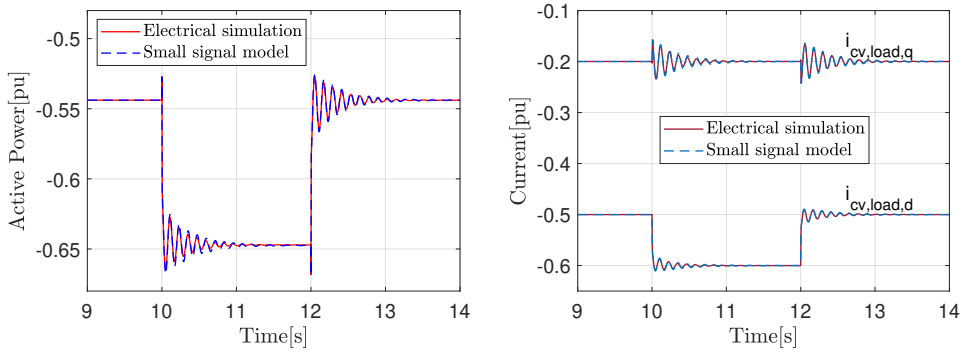

Figure 4.7: Dynamic response of the active power and filter currents for the active load with a 0.1 pu temporary step change in d-axis filter current, $i^*_{cv,load,d}$, for the active load.

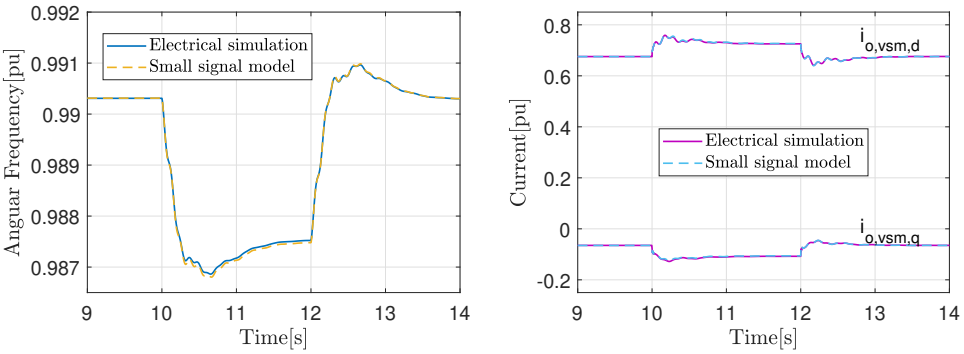

Figure 4.8: Dynamic response of the angular frequency and filter currents for the VSM with a 0.1 pu temporary step change in d-axis filter current, $i^*_{cv,load,d}$, for the active load.

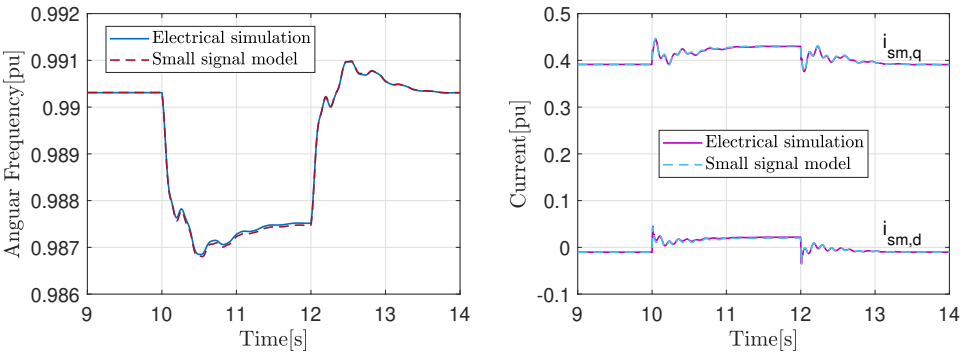

Figure 4.9: Dynamic response of the angular frequency and d and q-axis currents for the SM with a 0.1 pu temporary step change in d-axis filter current, $i^*_{cv,load,d}$, for the active load.

Lastly, presented in Figure 4.10, the dynamic response for the disturbance in the power system reference angular frequency, simulated by a perturbation in the angular frequency reference of the SM, ω^*_{sm}. The plot on top in Figure 4.10 shows the response of the SM rotor angular frequency. The bottom left plot the shows the active power response for all three units and the left plot shows angular deviation of the SRRF VSM and SRRF active load from the grid voltage vector. As the frequency of the SM decreases the active power output of the SM also decreases, the VSM compensates for the loss of active power. As a consequence the consumed active power of the active load stays constant.

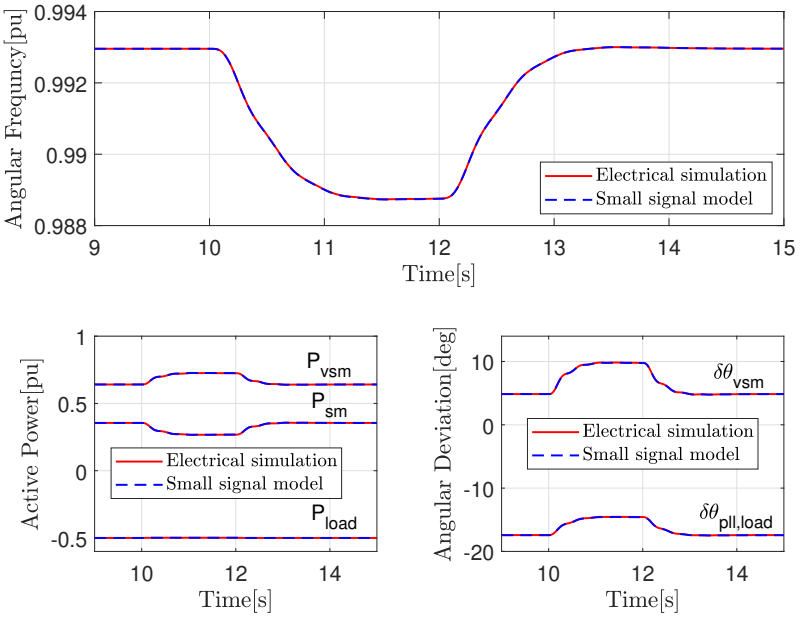

Figure 4.10: Results for 0.1 pu step in the angular frequency reference of the SM. Figure shows the response of the SM rotor angular frequency, active power output of VSM, SM and active load and the angular deviation of VSM SRRF and active load SRRF.

The small deviations between the electrical simulation and the small-signal model for the dynamic response of the hybrid ship power system is most likely due to the coupling between states and the non-linearties that are not present in the small-signal model. Overall, there is a good correspondence between the response of the dynamic (non-linear) model and the corresponding small-signal (linearized) state space model for the hybrid ship power system. This indicates that the small-signal model accurately represents the system under study. This confirms the validity of the small-signal model around the steady state operating point and supports its application in the small-signal stability analysis of the power system using traditional linear techniques.

Chapter 5

Eigenvalue analysis

The accuracy of the small-signal (linearization) model around the steady-state operating point has been verified. Eigenvalue analysis is utilized to examine small-signal dynamics using the linearized state-space model established in the previous sections. Furthermore, by charting the eigenvalue trajectories in the complex plane for a variety of parameter values or operating circumstances, the effect of the parameters on the modes of the system can be assessed.

This subsection focuses on the impact of three primary parameters on the hybrid ship power system's dynamic response: restive loading, the active power of the active load, and the VSM virtual inertia and stator resistance. Large signal stability and the potential influence of saturation of the current limits during transients are not captured by the presented eigenvalue analysis. Large signal stability can be validated using time-domain simulation. This is, however, considered not to be within the scope of this thesis.

When evaluating the non-linear hybrid ship power system and its corresponding linear model, the eigenvalues are essentially constant. These eigenvalues are not affected by the operating conditions, but the linearization of the non-linear systems generally results in different linear models for each steady-state operating point, fundamentally leading to a correlation between operating modes and conditions. As a result, the displacement of the eigenvalues in the complex plane as a function of the operating conditions indirectly provides a qualitative indication of the non-linearity of the system.

Next, the confirmation of the stability of the hybrid ship power system in all operating ranges is presented. This has been completed by calculating the eigenvalues (modes), for the state matrices of the small-signal model, $\mathbf{A}_{sys}$, for a given situation and corresponding parameters, with initial inputs varying within a reciprocal interval. The resulting system eigenvalues for the operating point corresponding to the conditions given in Table 4.1-4.4 are listed in Table 5.1.

5.1 Participation factor

Participation factors are non-dimensional scalars that measure the interaction between the modes and the state variables of a linear system and are useful for analyzing power systems. The results from the calculated participation factor for the hybrid ship power system are found in Table 5.1. As the table clearly indicates, the eigenvalues λ_1 and λ_2 corresponds to the grid voltage states. The eigenvalues position in the complex plane is a result of the high value of the load connected to the AC-bus. The eigenvalues $\lambda_{3,4}$, $\lambda_{15,16}$ and λ_6 through to λ_{12} are all resulting from the filters of the VSM and Active Load as well as the d and q-axis currents from the SM.

For all three units in the power system, their measurement states are found in modes 13, 14, 21, 23, and 25 and are all related to the filter cut-off angular frequency of the filters. Similarly, both the active load and VSM the phase lock loop (PLL) low-pass filters give the location of modes 19, 20, 22, and 24. The PLL is also linked to modes 25, 26, 29, and 30. The filters of the active damping have a lower cut-off frequency than for the PLL, but cannot be directly recognized in any of the eigenvalues. Modes 27, 28, 31, 32, and 33 however, have a close interaction with the states of the active damping in both the VSM and active load, in addition to being coupled with the currents in the SM and the integral state of the voltage controller of VSM. These eigenvalues are in near connection with reactive power-voltage control of the power system, and thus the related states influence the voltage stability of the power system.

Coupling between the SM current states can be recognized in $\lambda_{17,18}$, λ_{34} and $\lambda_{37,38}$, and are determined by the SM parameters. Other eigenvalues determined by the SM parameters are λ_{45}, mainly influenced by the q-axis current, and λ_{46}, corresponding to the Exciter/AVR. $\lambda_{35,36}$ and $\lambda_{43,44}$ are the main influences on the frequency and power stability of the power system. These eigenvalues are closely related to the chose the first-order delay used to model the dynamics of the SM governor and turbine, the angular frequency of both the SM and VSM and the angular deviation of the VSM SRRF from the grid voltage. As appose to the SM, the VSM parameters are not assumed fixed, and can therefore be tuned to influence the power and frequency stability of the power system.

Lastly, $\lambda_{39,40}$ and $\lambda_{41,42}$ relate to the current controller of the active load and the VSM, respectively. The position of these eigenvalues is limited by the related integration time, k_{pc}/k_{ic}. For both the VSM and the active load the integral time correspond to the filter inductors time constant, $l_f/(\omega_b r_f) \approx 0.0895$s. For assessing the system stability, the slow and poorly damped poles are of main interest. The result of some parameter influence on these modes is introduced in section 5.4. First, the dynamic effects of the static load and the dynamic characteristics of the hybrid ship power system dynamic under its full operating range will be presented.

Table 5.1: Table of eigenvalues (modes) and the main participating states [participation factor] for the hybrid ship power system model.

Mode(s)	Value(s)	State(s) [Participation factor]
λ_1	-306181	$\hat{v}_{g,q}$
λ_2	-304316	$\hat{v}_{g,d}$
$\lambda_{3,4}$	$-2082.3 \pm \text{j}9286.5$	$v_{o,vsm,q}^{[0.26]}$, $i_{cv,vsm,q}^{[0.25]}$, $v_{o,vsm,d}^{[0.24]}$, $i_{cv,vsm,d}^{[0.21]}$
λ_5	-9644.58	$i_{sm,d}^{[0.37]}$, $i_{o,vsm,q}^{[0.34]}$, $i_{o,load,q}^{[0.30]}$
λ_6	-7778.04	$i_{o,vsm,d}^{[0.41]}$, $i_{o,load,d}^{[0.36]}$, $i_{sm,q}^{[0.20]}$
$\lambda_{7,8}$	$-1720.43 \pm \text{j}6935.76$	$v_{o,vsm,d}^{[0.34]}$, $v_{o,vsm,q}^{[0.30]}$, $i_{cv,vsm,d}^{[0.29]}$, $i_{cv,vsm,q}^{[0.25]}$
$\lambda_{9,10}$	$-2277.7 \pm \text{j}6554.81$	$v_{o,load,d}^{[0.29]}$, $v_{o,load,q}^{[0.27]}$, $i_{cv,load,d}^{[0.24]}$, $i_{cv,load,q}^{[0.23]}$
$\lambda_{11,12}$	$-2434.43 \pm \text{j}6214.85$	$v_{o,load,q}^{[0.76]}$, $v_{o,load,d}^{[0.27]}$, $i_{cv,load,q}^{[0.26]}$, $i_{cv,load,d}^{[0.24]}$
$\lambda_{13,14}$	$-1611.08 \pm \text{j}1641.99$	$v_{m,vsm,q}^{[0.53]}$, $v_{m,vsm,d}^{[0.52]}$
$\lambda_{15,16}$	$-464.831 \pm \text{j}328.906$	$i_{o,load,q}^{[0.29]}$, $i_{o,load,d}^{[0.26]}$, $i_{sm,d}^{[0.17]}$, $i_{o,vsm,d}^{[0.16]}$, $i_{o,vsm,q}^{[0.13]}$
$\lambda_{17,18}$	$-75.7551 \pm \text{j}356.297$	$i_{sm,d}$, $i_{fd}^{[0.75]}$, $i_{1d}^{[0.65]}$, $i_{sm,q}^{[0.55]}$
λ_{19}	-948.155	$v_{pll,vsm,q}$
λ_{20}	-1009.93	$v_{pll,load,q}$
λ_{21}	-1000.03	$q_{m,sm}$
λ_{22}	-1000	$v_{pll,load,d}$
λ_{23}	-195.938	$q_{m,vsm}$
λ_{24}	-1000	$v_{pll,vsm,d}$
$\lambda_{25,26}$	$-3.027 \pm \text{j}53.614$	$\delta\theta_{pll,load}^{[0.47]}$, $\varepsilon_{pll,load}^{[0.41]}$
$\lambda_{27,28}$	$-48.95 \pm \text{j}30.62$	$\xi_{vsm}^{[0.48]}$, $\phi_{vsm,q}^{[0.37]}$, $\phi_{vsm,d}^{[0.31]}$
$\lambda_{29,30}$	$-30.25 \pm \text{j}25.62$	$\varepsilon_{pll,vsm}^{[0.88]}$, $\delta\theta_{pll,vsm}^{[0.64]}$
$\lambda_{31,32}$	$-40.57 \pm \text{j}13.96$	$\phi_{load,q}^{[0.58]}$, $\phi_{load,d}^{[0.51]}$, $i_{1d}^{[0.32]}$, $i_{sm,d}^{[0.31]}$, $\varepsilon_{pll,load}^{[0.27]}$, $i_{fd}^{[0.12]}$
λ_{33}	-32.5247	$i_{1d}^{[0.76]}$, $\phi_{vsm,q}^{[0.35]}$, $\phi_{vsm,q}^{[0.34]}$, $\xi_{vsm}^{[0.29]}$, $i_{sm,d}^{[0.28]}$, $i_{fd}^{[0.21]}$
λ_{34}	-29.4379	i_{1d}, $i_{fd}^{[0.50]}$, $i_{sm,q}^{[0.39]}$
$\lambda_{35,36}$	$-2.61 \pm \text{j}16.41$	$\delta\theta_{vsm}^{[0.61]}$, $\omega_{sm}^{[0.38]}$, $\delta\theta_{pll,vsm}^{[0.28]}$, $\omega_{vsm}^{[0.18]}$
$\lambda_{37,38}$	$-4.63 \pm \text{j}7.55$	i_{fd}, $i_{sm,d}^{[0.85]}$, $v_{fd}^{[0.55]}$
$\lambda_{39,40}$	$-11.635 \pm \text{j}0.595$	$\gamma_{load,q}^{[0.54]}$, $\gamma_{load,d}^{[0.52]}$
λ_{41}	-11.853	$\gamma_{vsm,q}^{[0.52]}$, $\gamma_{vsm,d}^{[0.41]}$
λ_{42}	-11.713	$\gamma_{vsm,d}^{[0.63]}$, $\gamma_{vsm,q}^{[0.51]}$
$\lambda_{43,44}$	$-2.886 \pm \text{j}1.921$	$p_{m,sm}^{[0.59]}$, $\omega_{sm}^{[0.51]}$, $\delta\theta_{vsm}^{[0.25]}$, $\delta\theta_{pll,vsm}^{[0.16]}$, $\omega_{vsm}^{[0.15]}$
λ_{45}	-5.455	i_{1q}
λ_{46}	-0.282	ζ_{sm}

5.2 The effect of change in static load on system dynamics

The first aspect for assessing the capabilities of the power system is to evaluate the stability for a wide range of static loads. The trajectories of the eigenvalues have been calculated for the full range between 1.0 pu and 100 pu for the shunt resistance found on the AC-bus, emulating the full range of possible resistive loading conditions. The outcome is illustrated in Figure 5.1, with blue representing the lowest values and red representing the highest. For this case, the active power references for the VSM, p^*_{vsm}, has been maintained constant and equal to 0.5 pu and 0.25 pu for the SM, p^*_{sm}.

As Figure 5.1 shows there is in fact a very pronounced shift of the poles. However, the change is mainly limited to the eigenvalues with high oscillation frequency or with a short time constant. These poles are primarily associated with the electrical dynamics of the grid and the LC filters. The zoomed version of the plot in Figure 5.2 confirms that there are minor effects on the poles closes to the origin, being the most critical for the stability of the power system. As the results show, the change in resistive load plays part in defining the electrical resonances in the power system. However, it will not significantly impact the eigenvalues of significance related to the power or frequency control.

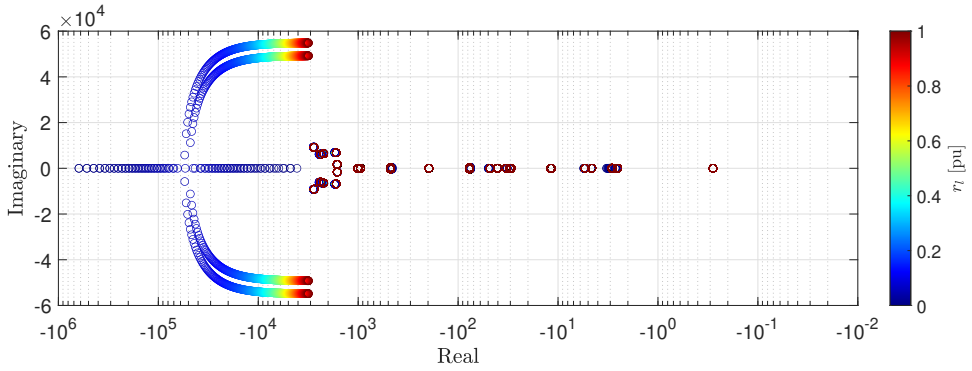

Figure 5.1: Eigenvalue trajectory for a sweep of load resistance, r_l, from 100 pu to 1.0 pu.

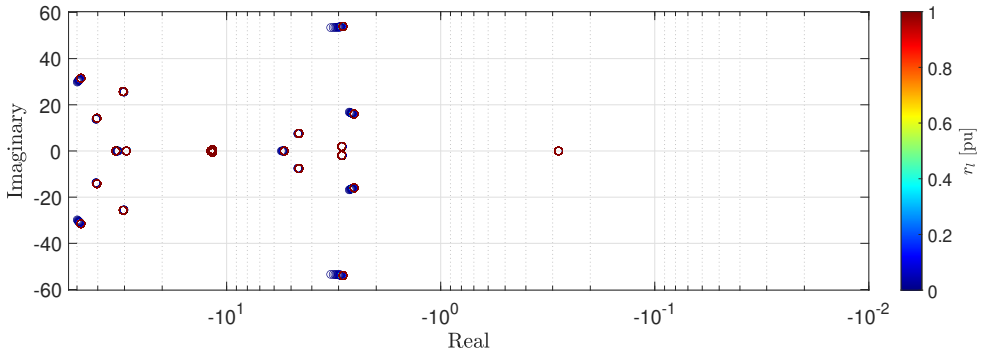

Figure 5.2: Zoomed in eigenvalue trajectory for a sweep of load resistance, r_l, from 100 pu to 1.0 pu.

5.3 Dynamic characteristics over the full operating range

As mentioned previously, the SM unit is responsible for actively controlling the frequency and voltage of the grid in the hybrid ship power system. Both the SM and VSM contributes to the power power balance and stability of the power system, and the capabilities of both units needs to be evaluated. The stability of the SM and VSM over their whole designated power range is an indication of their capabilities. The trajectories of the eigenvalues have been calculated for the full range between -1.0 and 1.0 pu for the active power reference for both the VSM, p^*_{vsm}, and SM, p^*_{sm}. A trajectory of the poles can seen in Figure 5.3 and 5.4 for input parametric sweep of the VSM power reference, p^*_{vsm}, from -1.0 pu to 1.0 pu, together with a parametric sweep of the SM power reference sweep, p^*_{sm}, from 1.0 pu to 0.0 pu and then the active load d-axis reference, $i^*_{cv,d}$, from 0.0 to -1.0 . An overview of all the eigenvalues of the system is presented in Figure 5.3, and a zoomed view of the poles closest to the imaginary axis is presented in Figure 5.4. As the position of the plots indicates the system maintains a small-signal stability for the entire operating range. There is little change in the eigenvalues position, and most of the critical modes are not effected.

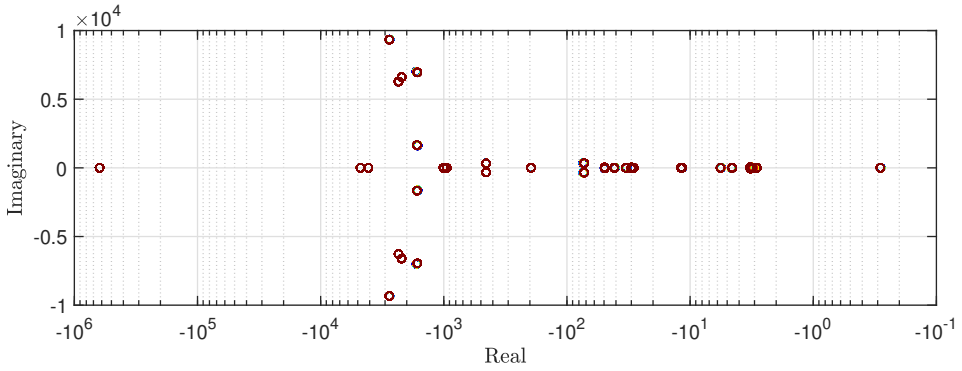

Figure 5.3: Eigenvalue trajectory for a sweep of VSM active power reference, p^*_{vsm}, from -1.0 pu to 1.0 pu and SM active power reference, p^*_{sm}, from 1.0 pu to -1.0 pu.

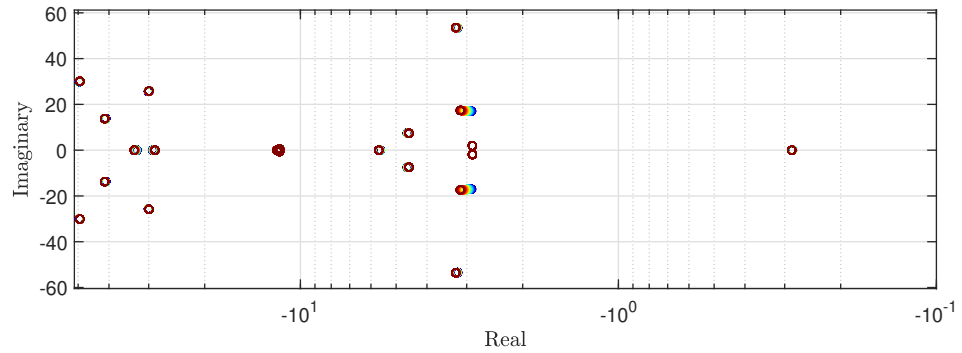

Figure 5.4: Zoomed inn eigenvalue trajectory for a sweep of VSM active power reference, p^*_{vsm}, from -1.0 pu to 1.0 pu, SM active power reference, p^*_{sm}, from 1.0 pu to 0.0 pu and then the active load d-axis reference, $i^*_{cv,d}$, from 0.0 to -1.0

5.4 Impact of virtual inertia, damping and stator resistance on system stability

The unidirectional component of the hybrid ship power system dynamic response is dominated by the slowest (real) mode, λ_{45} and λ_{46}. As Table 5.1 shows, the λ_{46} is connected to the integral state of the SM exciter, and altering the integral gain has little influencing on the position of the eigenvalue. Furthermore, the armature voltage of the SM is determined by the grid and cannot be controlled directly by the SM. The placement of λ_{45} is determined by the fixed parameters of the SM and can therefore not be affected by the tuning of parameters.

The complex conjugate pairs $\lambda_{43,44}$ and $\lambda_{35,36}$ are also of great importance to the power systems stability. The time constants of $\lambda_{43,44}$ and $\lambda_{35,36}$, 0.35 and 0.38 respectively, and

are very similar. However, the damping ratio of the modes differs. The damping factor of the eigenvalues $\lambda_{43,44}$ is $-\sigma_{43,44}/\sqrt{\sigma_{43,44}^2 + \omega_{43,43}^2} \approx 0.8333 > 0.05$, a damping factor which in practice is considered more than satisfactory in traditional power systems [33]. Whereas the damping factor of $\lambda_{35,36}$ is much lower in value, but still sufficient for a traditional power system. When studying the influence of the virtual inertia, damping gain, and virtual stator resistance on the power system stability, the critical modes 35, 36, 43, and 44 are given special attention as their position and damping are critical to the dynamics of the power system.

Figure 5.5 shows the trajectory of the slowest poles in the power system, for a sweep of T_a from 0.1 s to 8.0 s. The blue color is related to the smaller values of the virtual inertia time constant while the red color represents the larger time constant. A high value of inertia time constant will lead to slower oscillatory modes and a higher risk of approaching small-signal instability. The system will be stable for even higher values of the virtual inertia time constant than what is shown in Figure 5.5. Decreasing the inertia time constant has mostly beneficial effects on the stability, but when looking at $\lambda_{35,36}$ for time constants smaller than 1, they lead to a higher oscillation frequency for this the pair of eigenvalues. Whereas for $\lambda_{43,42}$ higher inertia time constant leads to a faster damping and a lower oscillation frequency. Overall, a very high virtual inertia value will not have any significant stabilizing effect and the general result will be an increase in the settling time for the system. The chosen inertia time constant for the base case seems to be a good balance between settling and response time.

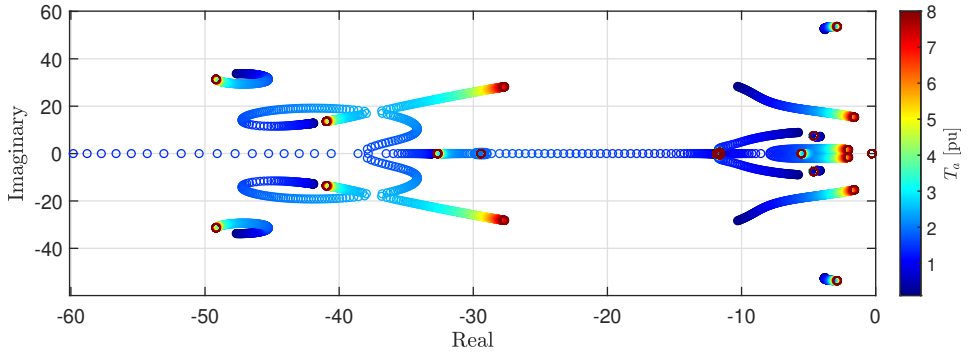

Figure 5.5: Eigenvalue trajectory for a sweep of virtual inertia time constant, T_a, from 0.1 s to 8.0 s.

By simulating the stat-space model for the power system, the impact of the T_a on the frequency of the system can be analyzed. Figure 5.6 show the response of the rotor frequency of the SM for with T_a set to 0.0001, 1, 4 and 8. The simulation results show that a higher inertia time constant will lead to a slower response with more oscillation, but with less of a dip (frequency nadir).

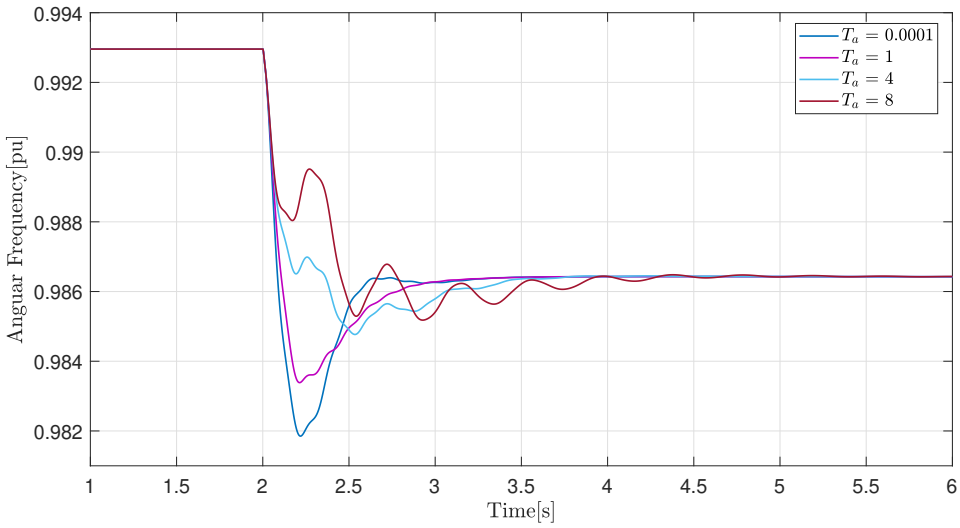

Figure 5.6: SM rotor angular frequency response to a increase in active power for different values of T_a.

With regards to the virtual stator resistance, $r_{s,vsm}$, the resulting trajectory can be seen in Figure 5.7. The plot shows the change in $r_{s,vsm}$ from 0.001 s to 0.4 s, where the blue color is related to the small values while the red color represents the larger values. Higher virtual resistance will eventually lead to instability in the system, as a result of the $\lambda_{43,44}$ ending up in the right half-plane. The trajectory shows that decreasing the virtual stator resistance has little effect on the critical modes of the system. A lower stator resistance could however be chosen than what is need for the SM. A higher value will still only implies virtual losses that do not influence the efficiency of the system but will have implications on the coupling between the reactive and active power.

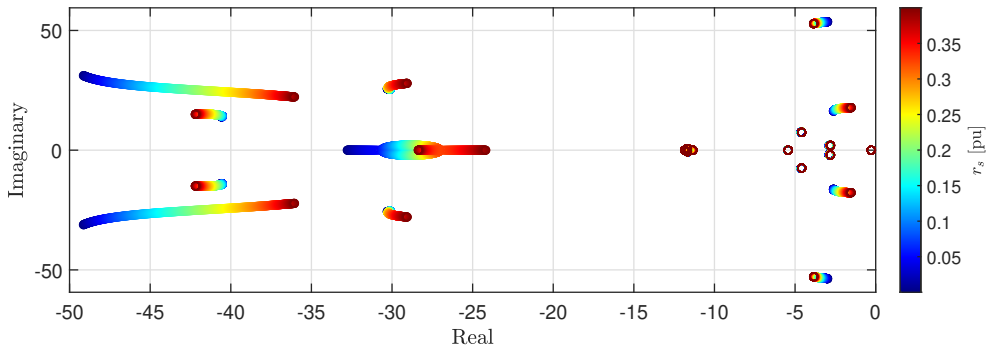

Figure 5.7: Eigenvalue trajectory for a sweep of virtual stator resistance, r_s, from 0.0001 pu to 0.4 pu.

The impact of varying the gain, $k_{d,vsm}$, can be seen in Figure 5.8. The plot shows the sweep in $k_{d,vsm}$ from 0.0 to 80, where the blue color is related to the small values while the red color represents the larger values. The trajectory shows that increasing the damping gain has a positive effect on modes 35 and 36. To further investigate the impact of the varying values of the damping gain, the dynamic response of the power system for a perturbation can be studied. To accomplish this, the simulated response of the small-signal model with four different values of $k_{d,vsm}$ has been plotted for an active power increase in the system. Figure show the response of the rotor frequency of the SM for with $k_{d,vsm}$ set to 0.0, 20, 40 and 80. Figure 5.9 show the results and a higher damping gain will lead to a smoother frequency response with less oscillation and a faster settling time.

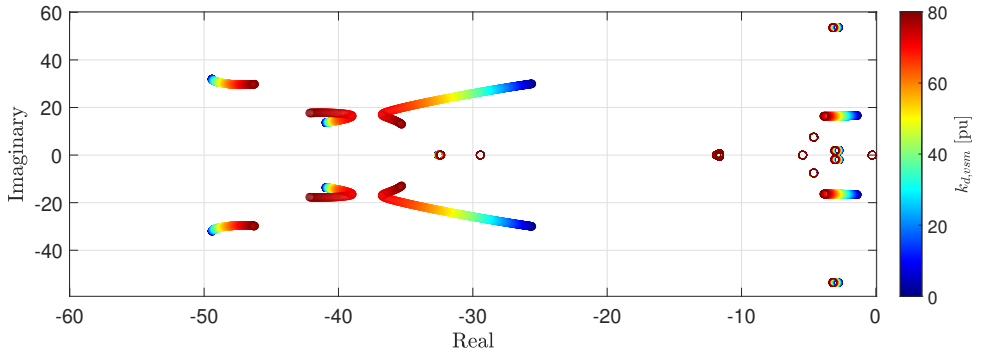

Figure 5.8: Eigenvalue trajectory for a sweep of damping gain, k_d, from 0.0 pu to 80 pu.

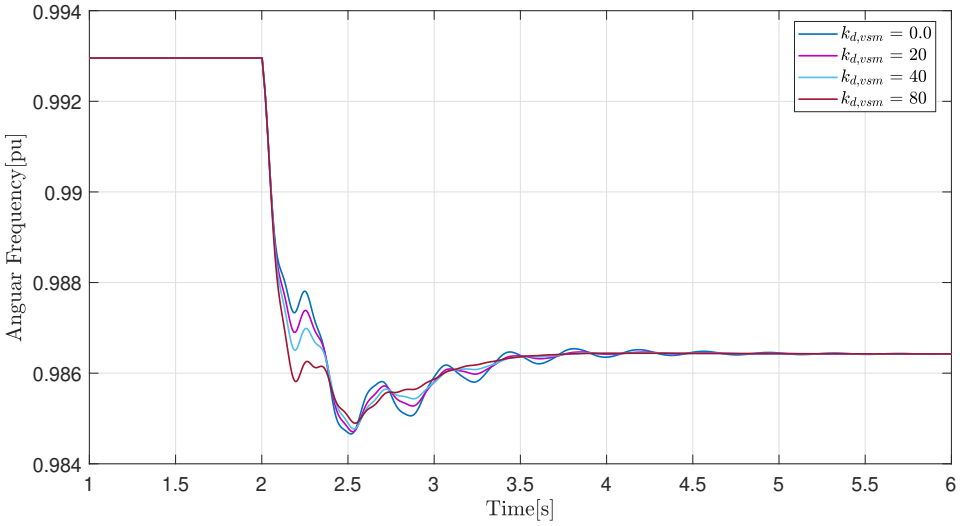

Figure 5.9: SM rotor angular frequency response to a increase in active power for different values of $k_{d,vsm}$.

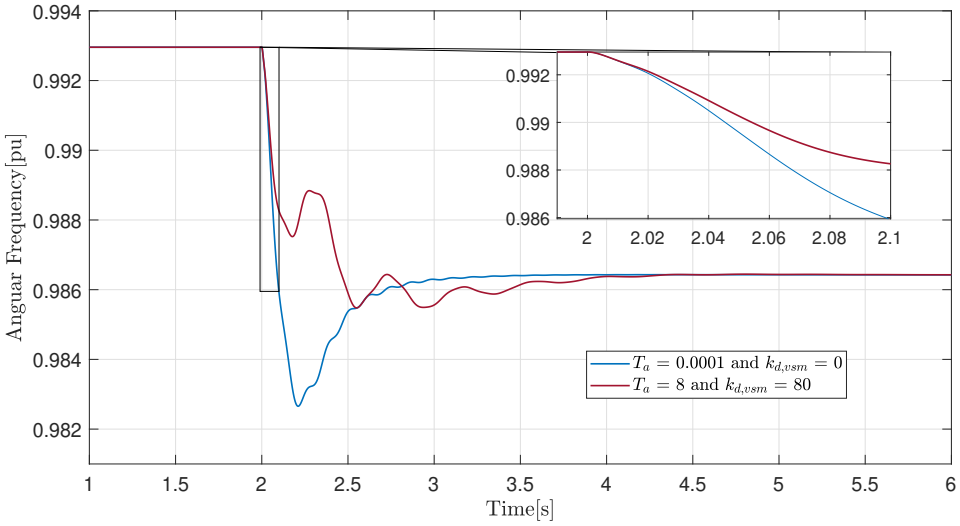

Figure 5.10: SM rotor angular frequency response to a increase in active power for different values of T_a and $k_{d,vsm}$.

The results from sweeps and the state-space simulations of the varying values of T_a and $k_{d,vsm}$ indicate that by incorporating the power system with a high value for both parameters a frequency response for the system with the little nadir and fewer oscillations may be achieved. Figure 5.10 show the response for to simulations one for $k_{d,vsm} = 0$

and $T_a = 0.0001$, and one for $k_{d,vsm} = 80$ and $T_a = 80$. From the figure, we can see that the system did achieve less frequency nadir and less oscillation. From the zoomed-in plot it can also be noticed that the ROCOF of the system is smaller for the simulation with the higher values, which is desirable.

Chapter 6

Conclusion and further work

6.1 Conclusion

In future ship power systems, the need for hybrid solutions may become essential to develop reliable and efficient power systems. Applications such as load sharing, reactive power control (voltage stability), and backup power can be achieved with the use of a VSM-implementations. The VSM has the capabilities to control the voltage amplitude and frequency of a power system in islanded mode, and with the same control system, can be used in parallel with diesel generators. In this thesis, the VSM-implementation in a hybrid ship power system has proven to have the potential to permit seamless operation under a wide range of system conditions.

The thesis has been presented with the focus on the implementation of a state-space model, and the small-signal analysis, of a hybrid marine power system with a VSM. A mathematical model of a marine power system consisting of an SM, active load and VSM has been developed, where each component was initially modeled connected to a stiff grid. The small-signal model for each component has been verified with the electrical (non-linear) model and is presented with their non-linear state-space model.

It is evident from the simulation results that the VSM-controlled VSC together with the ideal DC source, acquire the *damping*, *load sharing* and *inertia response* to behave as the SM. The VSM has displayed the aforementioned properties in a power system with fixed loads and active load that imitates the dynamics of large propulsion motors in ships. Together with an ESS, the VSM-implantation can facilitate a large dynamic load and by doing the same work as an SM but with no need for fossil fuel, and can therefore lower the fuel consumption for a ship.

This thesis has also presented an eigenvalue-based assessment of how the small-signal dynamics are influenced by the operating conditions and parameters of the VSM. The small-signal analysis has given further insight into the system response and the coupling between the states of the system. Eigenvalue trajectories and participation factor analysis

have given an understanding of the developed small-signal model, and the dynamics of states and parameters influence this model. The small-signal stability has been proven for the operation of static loads and dynamic loads. Excessively high values of stator resistance can have a negative effect on the dynamic response of the system and ultimately lead to small-signal instability.

From the small-signal analysis, the flexibility of the VSM parameters stands out as one of its great features. Unlike the SM with the physical presence of rotating mass and damper windings, the virtual damping and inertia response of the VSM can be varied to achieve optimal performance. This has been shown with the sweep of T_a and $k_{d,vsm}$ parameters of the VSM. More desirable frequency response for the power system was accomplished by the tuning of these variables.

In conclusion, it can be stated that the proposed hybrid ship power system with a VSM-implementation has shown promising characteristics for use in new hybrid vessels and in retrofitting (older vessels) as the VSM enhances the system stability, reliability, and flexibility by emulating the behavior of the SM.

6.2 Further work

The implemented hybrid ship power system utilized in this thesis is a simplified model of a common hybrid AC distributed power system. The model could therefore be extended to include more SMs, VSMs, and active loads to obtain a more realistic model. The coupling between components in a more complex system will have an impact on the study of the frequency and voltage stability of the power system.

For this thesis, the switching effects are neglected and the VSCs used are presented by ideal average models. For further work, the switching effects could be introduced and analysis into the harmonic pollution may be of interest. Harmonic pollution is defined as any waveform with frequencies that are multiples of the fundamental frequency that is measured as *Total Harmonic Distrotion* (THD). Most ship power systems today are affected by harmonic pollution and it can have an impact on equipment lifespan and even lead to system breakdowns.

A more in-depth investigation into to *parametric sensitivity* could be conducted looking into other parameters than those that have been studied for this thesis. Parameters such as the gains for the variety of controllers and the cut-off frequencies for the filters of the VSM. A further expansion of the model can be done to investigate if the system provides the right amount of detail. In doing so, the small-signal model developed can be manipulated to obtain equitable characteristics.

Appendix A

Synchronous machine system mathematical model in grid-connected operation

A.1 Non-linear model

The nonlinear equations for the grid-connected SM is given by (A.1)-(A.11).

$$\begin{aligned}\frac{\mathrm{d}i_{\mathrm{sm},d}}{\mathrm{d}t} =& \frac{\omega_b \left(l_{11\mathrm{d}}\, l_{\mathrm{ffd}} - {l_{\mathrm{f1d}}}^2\right) \left(i_{\mathrm{sm},d}\, r_a - \omega_{\mathrm{sm}} \left(i_{\mathrm{sm},q} \left(l_{\mathrm{aq}} + l_l\right) - i_{1\mathrm{q}}\, l_{\mathrm{aq}}\right) - \hat{v}_{g,q} \cos\left(\delta\theta_{\mathrm{sm}}\right) + \hat{v}_{g,d} \sin\left(\delta\theta_{\mathrm{sm}}\right)\right)}{l_{11\mathrm{d}}\, {l_{\mathrm{ad}}}^2 + l_{\mathrm{ad}}\, {l_{\mathrm{f1d}}}^2 - 2\, {l_{\mathrm{ad}}}^2\, l_{\mathrm{f1d}} + {l_{\mathrm{ad}}}^2\, l_{\mathrm{ffd}} + {l_{\mathrm{f1d}}}^2\, l_l - l_{11\mathrm{d}}\, l_{\mathrm{ad}}\, l_{\mathrm{ffd}} - l_{11\mathrm{d}}\, l_{\mathrm{ffd}}\, l_l} \\ & - \frac{\omega_b \left(v_{\mathrm{fd}} - i_{\mathrm{fd}}\, r_{\mathrm{fd}}\right) \left(l_{11\mathrm{d}}\, l_{\mathrm{ad}} - l_{\mathrm{ad}}\, l_{\mathrm{f1d}}\right)}{l_{11\mathrm{d}}\, {l_{\mathrm{ad}}}^2 + l_{\mathrm{ad}}\, {l_{\mathrm{f1d}}}^2 - 2\, {l_{\mathrm{ad}}}^2\, l_{\mathrm{f1d}} + {l_{\mathrm{ad}}}^2\, l_{\mathrm{ffd}} + {l_{\mathrm{f1d}}}^2\, l_l - l_{11\mathrm{d}}\, l_{\mathrm{ad}}\, l_{\mathrm{ffd}} - l_{11\mathrm{d}}\, l_{\mathrm{ffd}}\, l_l} \\ & - \frac{i_{1\mathrm{d}}\, \omega_b\, r_{1\mathrm{d}} \left(l_{\mathrm{ad}}\, l_{\mathrm{f1d}} - l_{\mathrm{ad}}\, l_{\mathrm{ffd}}\right)}{l_{\mathrm{sm},q}}\end{aligned} \tag{A.1}$$

$$\begin{aligned}\frac{\mathrm{d}i_{\mathrm{sm},q}}{\mathrm{d}t} =& - \frac{l_{11\mathrm{q}}\, \omega_b \left(i_{\mathrm{sm},q}\, r_a + \hat{v}_{g,d} \cos\left(\delta\theta_{\mathrm{sm}}\right) - \omega_{\mathrm{sm}} \left(i_{1\mathrm{d}}\, l_{\mathrm{ad}} - i_{\mathrm{sm},d} \left(l_{\mathrm{ad}} + l_l\right) + i_{\mathrm{fd}}\, l_{\mathrm{ad}}\right) + \hat{v}_{g,q} \sin\left(\delta\theta_{\mathrm{sm}}\right)\right)}{-{l_{\mathrm{aq}}}^2 + l_{11\mathrm{q}}\, l_{\mathrm{aq}} + l_{11\mathrm{q}}\, l_l} \\ & - \frac{i_{1\mathrm{q}}\, l_{\mathrm{aq}}\, \omega_b\, r_{1\mathrm{q}}}{-{l_{\mathrm{aq}}}^2 + l_{11\mathrm{q}}\, l_{\mathrm{aq}} + l_{11\mathrm{q}}\, l_l}\end{aligned} \tag{A.2}$$

$$\begin{aligned}\frac{\mathrm{d}i_{\mathrm{fd}}}{\mathrm{d}t} =& \frac{\omega_b \left(l_{11\mathrm{d}}\, l_{\mathrm{ad}} - l_{\mathrm{ad}}\, l_{\mathrm{f1d}}\right) \left(i_{\mathrm{sm},d}\, r_a - \omega_{\mathrm{sm}} \left(i_{\mathrm{sm},q} \left(l_{\mathrm{aq}} + l_l\right) - i_{1\mathrm{q}}\, l_{\mathrm{aq}}\right) - \hat{v}_{g,q} \cos\left(\delta\theta_{\mathrm{sm}}\right) + \hat{v}_{g,d} \sin\left(\delta\theta_{\mathrm{sm}}\right)\right)}{l_{11\mathrm{d}}\, {l_{\mathrm{ad}}}^2 + l_{\mathrm{ad}}\, {l_{\mathrm{f1d}}}^2 - 2\, {l_{\mathrm{ad}}}^2\, l_{\mathrm{f1d}} + {l_{\mathrm{ad}}}^2\, l_{\mathrm{ffd}} + {l_{\mathrm{f1d}}}^2\, l_l - l_{11\mathrm{d}}\, l_{\mathrm{ad}}\, l_{\mathrm{ffd}} - l_{11\mathrm{d}}\, l_{\mathrm{ffd}}\, l_l} \\ & - \frac{\omega_b \left(v_{\mathrm{fd}} - i_{\mathrm{fd}}\, r_{\mathrm{fd}}\right) \left(-{l_{\mathrm{ad}}}^2 + l_{11\mathrm{d}}\, l_{\mathrm{ad}} + l_{11\mathrm{d}}\, l_l\right)}{l_{11\mathrm{d}}\, {l_{\mathrm{ad}}}^2 + l_{\mathrm{ad}}\, {l_{\mathrm{f1d}}}^2 - 2\, {l_{\mathrm{ad}}}^2\, l_{\mathrm{f1d}} + {l_{\mathrm{ad}}}^2\, l_{\mathrm{ffd}} + {l_{\mathrm{f1d}}}^2\, l_l - l_{11\mathrm{d}}\, l_{\mathrm{ad}}\, l_{\mathrm{ffd}} - l_{11\mathrm{d}}\, l_{\mathrm{ffd}}\, l_l} \\ & - \frac{i_{1\mathrm{d}}\, \omega_b\, r_{1\mathrm{d}} \left(-{l_{\mathrm{ad}}}^2 + l_{\mathrm{f1d}}\, l_{\mathrm{ad}} + l_{\mathrm{f1d}}\, l_l\right)}{l_{11\mathrm{d}}\, {l_{\mathrm{ad}}}^2 + l_{\mathrm{ad}}\, {l_{\mathrm{f1d}}}^2 - 2\, {l_{\mathrm{ad}}}^2\, l_{\mathrm{f1d}} + {l_{\mathrm{ad}}}^2\, l_{\mathrm{ffd}} + {l_{\mathrm{f1d}}}^2\, l_l - l_{11\mathrm{d}}\, l_{\mathrm{ad}}\, l_{\mathrm{ffd}} - l_{11\mathrm{d}}\, l_{\mathrm{ffd}}\, l_l}\end{aligned} \tag{A.3}$$

$$\begin{aligned}\frac{\mathrm{d}i_{1d}}{\mathrm{d}t} =&\frac{\omega_b\ (v_{\mathrm{fd}} - i_{\mathrm{fd}}\, r_{\mathrm{fd}})\ \left(-{l_{\mathrm{ad}}}^2 + l_{\mathrm{f1d}}\, l_{\mathrm{ad}} + l_{\mathrm{f1d}}\, l_l\right)}{l_{11\mathrm{d}}\, {l_{\mathrm{ad}}}^2 + l_{\mathrm{ad}}\, {l_{\mathrm{f1d}}}^2 - 2\, {l_{\mathrm{ad}}}^2\, l_{\mathrm{f1d}} + {l_{\mathrm{ad}}}^2\, l_{\mathrm{ffd}} + {l_{\mathrm{f1d}}}^2\, l_l - l_{11\mathrm{d}}\, l_{\mathrm{ad}}\, l_{\mathrm{ffd}} - l_{11\mathrm{d}}\, l_{\mathrm{ffd}}\, l_l} \\ &- \frac{\omega_b\ (l_{\mathrm{ad}}\, l_{\mathrm{f1d}} - l_{\mathrm{ad}}\, l_{\mathrm{ffd}})\ (i_{\mathrm{sm},d}\, r_a - \omega_{\mathrm{sm}}\ (i_{\mathrm{sm},q}\ (l_{\mathrm{aq}} + l_l) - i_{1\mathrm{q}}\, l_{\mathrm{aq}}) - \hat{v}_{g,q}\, \cos(\delta\theta_{\mathrm{sm}}) + \hat{v}_{g,d}\, \sin(\delta\theta_{\mathrm{sm}}))}{l_{11\mathrm{d}}\, {l_{\mathrm{ad}}}^2 + l_{\mathrm{ad}}\, {l_{\mathrm{f1d}}}^2 - 2\, {l_{\mathrm{ad}}}^2\, l_{\mathrm{f1d}} + {l_{\mathrm{ad}}}^2\, l_{\mathrm{ffd}} + {l_{\mathrm{f1d}}}^2\, l_l - l_{11\mathrm{d}}\, l_{\mathrm{ad}}\, l_{\mathrm{ffd}} - l_{11\mathrm{d}}\, l_{\mathrm{ffd}}\, l_l} \\ &+ \frac{i_{1\mathrm{d}}\, \omega_b\, r_{1\mathrm{d}}\ \left(-{l_{\mathrm{ad}}}^2 + l_{\mathrm{ffd}}\, l_{\mathrm{ad}} + l_{\mathrm{ffd}}\, l_l\right)}{l_{11\mathrm{d}}\, {l_{\mathrm{ad}}}^2 + l_{\mathrm{ad}}\, {l_{\mathrm{f1d}}}^2 - 2\, {l_{\mathrm{ad}}}^2\, l_{\mathrm{f1d}} + {l_{\mathrm{ad}}}^2\, l_{\mathrm{ffd}} + {l_{\mathrm{f1d}}}^2\, l_l - l_{11\mathrm{d}}\, l_{\mathrm{ad}}\, l_{\mathrm{ffd}} - l_{11\mathrm{d}}\, l_{\mathrm{ffd}}\, l_l}\end{aligned} \tag{A.4}$$

$$\begin{aligned}\frac{\mathrm{d}i_{1q}}{\mathrm{d}t} =&-\frac{l_{\mathrm{aq}}\, \omega_b\ (i_{\mathrm{sm},q}\, r_a + \hat{v}_{g,d}\, \cos(\delta\theta_{\mathrm{sm}}) - \omega_{\mathrm{sm}}\ (i_{1\mathrm{d}}\, l_{\mathrm{ad}} - i_{\mathrm{sm},d}\ (l_{\mathrm{ad}} + l_l) + i_{\mathrm{fd}}\, l_{\mathrm{ad}}) + \hat{v}_{g,q}\, \sin(\delta\theta_{\mathrm{sm}}))}{-{l_{\mathrm{aq}}}^2 + l_{11\mathrm{q}}\, l_{\mathrm{aq}} + l_{11\mathrm{q}}\, l_l} \\ &- \frac{i_{1\mathrm{q}}\, \omega_b\, r_{1\mathrm{q}}\ (l_{\mathrm{aq}} + l_l)}{-{l_{\mathrm{aq}}}^2 + l_{11\mathrm{q}}\, l_{\mathrm{aq}} + l_{11\mathrm{q}}\, l_l}\end{aligned} \tag{A.5}$$

$$\begin{aligned}\frac{\mathrm{d}\omega_{\mathrm{sm}}}{\mathrm{d}t} =&\frac{(l_{\mathrm{ad}} - l_{\mathrm{ad}})}{T_M} i_{\mathrm{sm},q} i_{\mathrm{sm},d} + \frac{l_{\mathrm{ad}}}{T_M} i_{1\mathrm{q}} i_{\mathrm{sm},d} - \frac{l_{\mathrm{ad}}}{T_M} i_{\mathrm{fd}} i_{\mathrm{sm},q} \\ &- \frac{l_{\mathrm{ad}}}{T_M} i_{1d} i_{\mathrm{sm},q} + \frac{k_{d,\mathrm{sm}}}{T_M} (\omega_{\mathrm{g}} - \omega_{\mathrm{sm}}) + \frac{1}{T_M} \frac{p_{m,\mathrm{sm}}}{\omega_{\mathrm{sm}}}\end{aligned} \tag{A.6}$$

$$\frac{\mathrm{d}\delta\theta_{\mathrm{sm}}}{\mathrm{d}t} = \omega_b \omega_{\mathrm{sm}} - \omega_b \omega_{\mathrm{g}} \tag{A.7}$$

$$\frac{\mathrm{d}p_{m,\mathrm{sm}}}{\mathrm{d}t} = -\frac{k_{\omega,\mathrm{sm}}}{T_{\mathrm{gt}}} \omega_{\mathrm{sm}} + \frac{1}{T_{\mathrm{gt}}} (p^*_{\mathrm{sm}} - p_{m,\mathrm{sm}}) + \frac{k_{\omega,\mathrm{sm}}}{T_{\mathrm{gt}}} \omega^*_{\mathrm{sm}} \tag{A.8}$$

$$\begin{aligned}\frac{\mathrm{d}q_{m,\mathrm{sm}}}{\mathrm{d}t} =&\omega_{f,\mathrm{sm}}\ (i_{\mathrm{sm},d}\ (\hat{v}_{g,d}\, \cos(\delta\theta_{\mathrm{sm}}) + \hat{v}_{g,q}\, \sin(\delta\theta_{\mathrm{sm}})) + i_{\mathrm{sm},q}\ (\hat{v}_{g,q}\, \cos(\delta\theta_{\mathrm{sm}}) - \hat{v}_{g,d}\, \sin(\delta\theta_{\mathrm{sm}}))) \\ &- \omega_{f,\mathrm{sm}}\, q_{m,\mathrm{sm}}\end{aligned} \tag{A.9}$$

$$\begin{aligned}\frac{\mathrm{d}\zeta}{\mathrm{d}t} =&\hat{v}^*_{\mathrm{sm}} + k_{q,\mathrm{sm}}\ (q^*_{\mathrm{sm}} - q_{m,\mathrm{sm}}) \\ &- \sqrt{(\hat{v}_{g,d}\, \cos(\delta\theta_{\mathrm{sm}}) + \hat{v}_{g,q}\, \sin(\delta\theta_{\mathrm{sm}}))^2 + (\hat{v}_{g,q}\, \cos(\delta\theta_{\mathrm{sm}}) - \hat{v}_{g,d}\, \sin(\delta\theta_{\mathrm{sm}}))^2}\end{aligned} \tag{A.10}$$

$$\begin{aligned}\frac{\mathrm{d}v_{\mathrm{fd}}}{\mathrm{d}t} =& \frac{k_{p,\mathrm{ex}}}{T_{\mathrm{ex}}} \hat{v}^*_{\mathrm{sm}} + \frac{k_{p,\mathrm{ex}} k_{q,\mathrm{sm}}}{T_{\mathrm{ex}}} (q^*_{\mathrm{sm}} - q_{m,\mathrm{sm}}) + \frac{k_{i,\mathrm{ex}}}{T_{\mathrm{ex}}} \zeta - \frac{1}{T_{\mathrm{ex}}} v_{\mathrm{fd}} \\ &- \frac{k_{p,\mathrm{ex}}}{T_{\mathrm{ex}}} \sqrt{(\hat{v}_{g,d}\, \cos(\delta\theta_{\mathrm{sm}}) + \hat{v}_{g,q}\, \sin(\delta\theta_{\mathrm{sm}}))^2 + (\hat{v}_{g,q}\, \cos(\delta\theta_{\mathrm{sm}}) - \hat{v}_{g,d}\, \sin(\delta\theta_{\mathrm{sm}}))^2}\end{aligned} \tag{A.11}$$

A.2 Small-signal model

By linearization of the nonlinear model (A.1)-(A.11), the small-signal state-space model has been derived, with the form given by (A.1) where Δ indicates the small-signal deviations around the steady-state operating point. For convenience of notation, $\mathbf{A}_{\mathrm{sm}}$ is expressed through 4 sub-matrices (A.6)-(A.9) as shown in (A.2) and the input matrix $\mathbf{B}_{\mathrm{sm}}$ is expressed through 4 sub-matrices (A.10)-(A.16) as shown in (A.3). To simplify the equations $l_{\mathrm{sm},d}$ (A.4) and $l_{\mathrm{sm},q}$ (A.5) are introduced.

$$\boldsymbol{\Delta}\dot{\mathbf{x}}_{\mathrm{sm}} = \frac{\mathrm{d}}{\mathrm{d}t}\boldsymbol{\Delta}\mathbf{x}_{\mathrm{sm}} = \mathbf{A}_{\mathrm{sm}}\boldsymbol{\Delta}\mathbf{x}_{\mathrm{sm}} + \mathbf{B}_{\mathrm{sm}}\boldsymbol{\Delta}\mathbf{u}_{\mathrm{sm}} \tag{A.1}$$

$$\mathbf{A}_{\mathrm{sm}} = \begin{bmatrix} \mathbf{A}_{\mathrm{sm},1} & \mathbf{A}_{\mathrm{sm},2} \\ \mathbf{A}_{\mathrm{sm},3} & \mathbf{A}_{\mathrm{sm},4} \end{bmatrix} \tag{A.2}$$

$$\mathbf{B}_{\mathrm{sm}} = \begin{bmatrix} \mathbf{B}_{\mathrm{sm},1} & \mathbf{B}_{\mathrm{sm},2} & \mathbf{B}_{\mathrm{sm},3} & \mathbf{B}_{\mathrm{sm},4} & \mathbf{B}_{\mathrm{sm},5} & \mathbf{B}_{\mathrm{sm},6} & \mathbf{B}_{\mathrm{sm},7} \end{bmatrix} \tag{A.3}$$

$$l_{\mathrm{sm},d} = l_{11\mathrm{d}}\, {l_{\mathrm{ad}}}^2 + l_{\mathrm{ad}}\, {l_{\mathrm{f1d}}}^2 - 2\, {l_{\mathrm{ad}}}^2\, l_{\mathrm{f1d}} + {l_{\mathrm{ad}}}^2\, l_{\mathrm{ffd}} + {l_{\mathrm{f1d}}}^2\, l_l - l_{11\mathrm{d}}\, l_{\mathrm{ad}}\, l_{\mathrm{ffd}} - l_{11\mathrm{d}}\, l_{\mathrm{ffd}}\, l_l \tag{A.4}$$

$$l_{\mathrm{sm},q} = -{l_{\mathrm{aq}}}^2 + l_{11\mathrm{q}}\, l_{\mathrm{aq}} + l_{11\mathrm{q}}\, l_l \tag{A.5}$$

$$\mathbf{A}_{\mathrm{sm},1} = \begin{pmatrix} \frac{\omega_b\, r_a\, \left(l_{11\mathrm{d}}\, l_{\mathrm{ffd}} - {l_{\mathrm{f1d}}}^2\right)}{l_{\mathrm{sm},d}} & -\frac{\omega_b\, \omega_{\mathrm{sm}}\, (l_{\mathrm{aq}} + l_l)\, \left(l_{11\mathrm{d}}\, l_{\mathrm{ffd}} - {l_{\mathrm{f1d}}}^2\right)}{l_{\mathrm{sm},d}} & \frac{\omega_b\, r_{\mathrm{fd}}\, (l_{11\mathrm{d}}\, l_{\mathrm{ad}} - l_{\mathrm{ad}}\, l_{\mathrm{f1d}})}{l_{\mathrm{sm},d}} \\ -\frac{l_{11\mathrm{q}}\, \omega_b\, \omega_{\mathrm{sm}}\, (l_{\mathrm{ad}} + l_l)}{l_{\mathrm{sm},q}} & -\frac{l_{11\mathrm{q}}\, \omega_b\, r_a}{l_{\mathrm{sm},q}} & \frac{l_{11\mathrm{q}}\, l_{\mathrm{ad}}\, \omega_b\, \omega_{\mathrm{sm}}}{l_{\mathrm{sm},q}} \\ \frac{\omega_b\, r_a\, (l_{11\mathrm{d}}\, l_{\mathrm{ad}} - l_{\mathrm{ad}}\, l_{\mathrm{f1d}})}{l_{\mathrm{sm},d}} & -\frac{\omega_b\, \omega_{\mathrm{sm}}\, (l_{\mathrm{aq}} + l_l)\, (l_{11\mathrm{d}}\, l_{\mathrm{ad}} - l_{\mathrm{ad}}\, l_{\mathrm{f1d}})}{l_{\mathrm{sm},d}} & \frac{\omega_b\, r_{\mathrm{fd}}\, \left(-{l_{\mathrm{ad}}}^2 + l_{11\mathrm{d}}\, l_{\mathrm{ad}} + l_{11\mathrm{d}}\, l_l\right)}{l_{\mathrm{sm},d}} \end{pmatrix} \tag{A.6}$$

$$\mathbf{A}_{\mathrm{sm},3} = \begin{pmatrix} -\frac{\omega_b\, r_a\, (l_{\mathrm{ad}}\, l_{\mathrm{f1d}} - l_{\mathrm{ad}}\, l_{\mathrm{ffd}})}{l_{\mathrm{sm},d}} & \frac{\omega_b\, \omega_{\mathrm{sm}}\, (l_{\mathrm{aq}} + l_l)\, (l_{\mathrm{ad}}\, l_{\mathrm{f1d}} - l_{\mathrm{ad}}\, l_{\mathrm{ffd}})}{l_{\mathrm{sm},d}} & -\frac{\omega_b\, r_{\mathrm{fd}}\, \left(-{l_{\mathrm{ad}}}^2 + l_{\mathrm{f1d}}\, l_{\mathrm{ad}} + l_{\mathrm{f1d}}\, l_l\right)}{l_{\mathrm{sm},d}} \\ -\frac{l_{\mathrm{aq}}\, \omega_b\, \omega_{\mathrm{sm}}\, (l_{\mathrm{ad}} + l_l)}{l_{\mathrm{sm},q}} & -\frac{l_{\mathrm{aq}}\, \omega_b\, r_a}{l_{\mathrm{sm},q}} & \frac{l_{\mathrm{ad}}\, l_{\mathrm{aq}}\, \omega_b\, \omega_{\mathrm{sm}}}{l_{\mathrm{sm},q}} \\ \frac{i_{\mathrm{sm},q}\, (l_{\mathrm{ad}} - l_{\mathrm{aq}})}{T_{\mathrm{sm}}} + \frac{i_{1\mathrm{q}}\, l_{\mathrm{aq}}}{T_{\mathrm{sm}}} & \frac{i_{\mathrm{sm},d}\, (l_{\mathrm{ad}} - l_{\mathrm{aq}})}{T_{\mathrm{sm}}} - \frac{i_{1\mathrm{d}}\, l_{\mathrm{ad}}}{T_{\mathrm{sm}}} - \frac{i_{\mathrm{fd}}\, l_{\mathrm{ad}}}{T_{\mathrm{sm}}} & -\frac{i_{\mathrm{sm},q}\, l_{\mathrm{ad}}}{T_{\mathrm{sm}}} \\ 0 & 0 & 0 \end{pmatrix} \tag{A.7}$$

$$\mathbf{A}_{\mathrm{sm},2} = \begin{pmatrix} -\frac{\omega_b\, r_{1\mathrm{d}}\, (l_{\mathrm{ad}}\, l_{\mathrm{f1d}} - l_{\mathrm{ad}}\, l_{\mathrm{ffd}})}{l_{\mathrm{sm},d}} & \frac{l_{\mathrm{aq}}\, \omega_b\, \omega_{\mathrm{sm}}\, \left(l_{11\mathrm{d}}\, l_{\mathrm{ffd}} - {l_{\mathrm{f1d}}}^2\right)}{l_{\mathrm{sm},d}} & -\frac{\omega_b\, (i_{\mathrm{sm},q}\, (l_{\mathrm{aq}} + l_l) - i_{1\mathrm{q}}\, l_{\mathrm{aq}})\, \left(l_{11\mathrm{d}}\, l_{\mathrm{ffd}} - {l_{\mathrm{f1d}}}^2\right)}{l_{\mathrm{sm},d}} & \frac{\omega_b\, \left(\hat{v}_{g,d}\, \cos(\delta\theta_{\mathrm{sm}}) + \hat{v}_{g,q}\, \sin(\delta\theta_{\mathrm{sm}})\right)\, \left(l_{11\mathrm{d}}\, l_{\mathrm{ffd}} - {l_{\mathrm{f1d}}}^2\right)}{l_{\mathrm{sm},d}} \\ \frac{l_{11\mathrm{q}}\, l_{\mathrm{ad}}\, \omega_b\, \omega_{\mathrm{sm}}}{l_{\mathrm{sm},q}} & -\frac{l_{\mathrm{aq}}\, \omega_b\, r_{1\mathrm{q}}}{l_{\mathrm{sm},q}} & \frac{l_{11\mathrm{q}}\, \omega_b\, \left(i_{1\mathrm{d}}\, l_{\mathrm{ad}} - i_{\mathrm{sm},d}\, (l_{\mathrm{ad}} + l_l) + i_{\mathrm{fd}}\, l_{\mathrm{ad}}\right)}{l_{\mathrm{sm},q}} & -\frac{l_{11\mathrm{q}}\, \omega_b\, \left(\hat{v}_{g,q}\, \cos(\delta\theta_{\mathrm{sm}}) - \hat{v}_{g,d}\, \sin(\delta\theta_{\mathrm{sm}})\right)}{l_{\mathrm{sm},q}} \\ -\frac{\omega_b\, r_{1\mathrm{d}}\, \left(-{l_{\mathrm{ad}}}^2 + l_{\mathrm{f1d}}\, l_{\mathrm{ad}} + l_{\mathrm{f1d}}\, l_l\right)}{l_{\mathrm{sm},d}} & \frac{l_{\mathrm{aq}}\, \omega_b\, \omega_{\mathrm{sm}}\, (l_{11\mathrm{d}}\, l_{\mathrm{ad}} - l_{\mathrm{ad}}\, l_{\mathrm{f1d}})}{l_{\mathrm{sm},d}} & -\frac{\omega_b\, (i_{\mathrm{sm},q}\, (l_{\mathrm{aq}} + l_l) - i_{1\mathrm{q}}\, l_{\mathrm{aq}})\, (l_{11\mathrm{d}}\, l_{\mathrm{ad}} - l_{\mathrm{ad}}\, l_{\mathrm{f1d}})}{l_{\mathrm{sm},d}} & \frac{\omega_b\, \left(\hat{v}_{g,d}\, \cos(\delta\theta_{\mathrm{sm}}) + \hat{v}_{g,q}\, \sin(\delta\theta_{\mathrm{sm}})\right)\, (l_{11\mathrm{d}}\, l_{\mathrm{ad}} - l_{\mathrm{ad}}\, l_{\mathrm{f1d}})}{l_{\mathrm{sm},d}} \end{pmatrix} \tag{A.8}$$

$$\mathbf{A}_{\mathrm{sm},4} = \begin{pmatrix} \frac{\omega_b\, r_{1\mathrm{d}}\, \left(-{l_{\mathrm{ad}}}^2 + l_{\mathrm{ffd}}\, l_{\mathrm{ad}} + l_{\mathrm{ffd}}\, l_l\right)}{l_{\mathrm{sm},d}} & -\frac{l_{\mathrm{aq}}\, \omega_b\, \omega_{\mathrm{sm}}\, (l_{\mathrm{ad}}\, l_{\mathrm{f1d}} - l_{\mathrm{ad}}\, l_{\mathrm{ffd}})}{l_{\mathrm{sm},d}} & \frac{\omega_b\, (i_{\mathrm{sm},q}\, (l_{\mathrm{aq}} + l_l) - i_{1\mathrm{q}}\, l_{\mathrm{aq}})\, (l_{\mathrm{ad}}\, l_{\mathrm{f1d}} - l_{\mathrm{ad}}\, l_{\mathrm{ffd}})}{l_{\mathrm{sm},d}} & -\frac{\omega_b\, \left(\hat{v}_{g,d}\, \cos(\delta\theta_{\mathrm{sm}}) + \hat{v}_{g,q}\, \sin(\delta\theta_{\mathrm{sm}})\right)\, (l_{\mathrm{ad}}\, l_{\mathrm{f1d}} - l_{\mathrm{ad}}\, l_{\mathrm{ffd}})}{l_{\mathrm{sm},d}} \\ \frac{l_{\mathrm{ad}}\, l_{\mathrm{aq}}\, \omega_b\, \omega_{\mathrm{sm}}}{l_{\mathrm{sm},q}} & -\frac{\omega_b\, r_{1\mathrm{q}}\, (l_{\mathrm{aq}} + l_l)}{l_{\mathrm{sm},q}} & \frac{l_{\mathrm{aq}}\, \omega_b\, \left(i_{1\mathrm{d}}\, l_{\mathrm{ad}} - i_{\mathrm{sm},d}\, (l_{\mathrm{ad}} + l_l) + i_{\mathrm{fd}}\, l_{\mathrm{ad}}\right)}{l_{\mathrm{sm},q}} & -\frac{l_{\mathrm{aq}}\, \omega_b\, \left(\hat{v}_{g,q}\, \cos(\delta\theta_{\mathrm{sm}}) - \hat{v}_{g,d}\, \sin(\delta\theta_{\mathrm{sm}})\right)}{l_{\mathrm{sm},q}} \\ -\frac{i_{\mathrm{sm},q}\, l_{\mathrm{ad}}}{T_{\mathrm{sm}}} & \frac{i_{\mathrm{sm},d}\, l_{\mathrm{aq}}}{T_{\mathrm{sm}}} & -\frac{k_{d,\mathrm{sm}}}{T_{\mathrm{sm}}} - \frac{p_{m,\mathrm{sm}}}{T_{\mathrm{sm}}\, {\omega_{\mathrm{sm}}}^2} & 0 \\ 0 & 0 & \omega_b & 0 \end{pmatrix} \tag{A.9}$$

$$\mathbf{B}_{\mathrm{sm},1} =$$

$$\begin{pmatrix}
\frac{\omega_b \sin(\delta\theta_{\mathrm{sm}}) \left(l_{11\mathrm{d}}\, l_{\mathrm{ffd}} - {l_{\mathrm{f1d}}}^2\right)}{l_{\mathrm{sm},d}} \\
-\frac{l_{11\mathrm{q}}\, \omega_b \cos(\delta\theta_{\mathrm{sm}})}{l_{\mathrm{sm},q}} \\
\frac{\omega_b \sin(\delta\theta_{\mathrm{sm}}) \left(l_{11\mathrm{d}}\, l_{\mathrm{ad}} - l_{\mathrm{ad}}\, l_{\mathrm{f1d}}\right)}{l_{\mathrm{sm},d}} \\
-\frac{\omega_b \sin(\delta\theta_{\mathrm{sm}}) \left(l_{\mathrm{ad}}\, l_{\mathrm{f1d}} - l_{\mathrm{ad}}\, l_{\mathrm{ffd}}\right)}{l_{\mathrm{sm},d}} \\
-\frac{l_{\mathrm{aq}}\, \omega_b \cos(\delta\theta_{\mathrm{sm}})}{l_{\mathrm{sm},q}} \\
0 \\
0 \\
0 \\
\omega_{f,\mathrm{sm}} \left(i_{\mathrm{sm},d} \cos\left(\delta\theta_{\mathrm{sm}}\right) - i_{\mathrm{sm},q} \sin\left(\delta\theta_{\mathrm{sm}}\right)\right) \\
-\frac{2\cos(\delta\theta_{\mathrm{sm}}) \left(\hat{v}_{g,d} \cos(\delta\theta_{\mathrm{sm}}) + \hat{v}_{g,q} \sin(\delta\theta_{\mathrm{sm}})\right) - 2\sin(\delta\theta_{\mathrm{sm}}) \left(\hat{v}_{g,q} \cos(\delta\theta_{\mathrm{sm}}) - \hat{v}_{g,d} \sin(\delta\theta_{\mathrm{sm}})\right)}{2\sqrt{\left(\hat{v}_{g,d} \cos(\delta\theta_{\mathrm{sm}}) + \hat{v}_{g,q} \sin(\delta\theta_{\mathrm{sm}})\right)^2 + \left(\hat{v}_{g,q} \cos(\delta\theta_{\mathrm{sm}}) - \hat{v}_{g,d} \sin(\delta\theta_{\mathrm{sm}})\right)^2}} \\
-\frac{k_{p,\mathrm{ex}} \left(2\cos(\delta\theta_{\mathrm{sm}}) \left(\hat{v}_{g,d} \cos(\delta\theta_{\mathrm{sm}}) + \hat{v}_{g,q} \sin(\delta\theta_{\mathrm{sm}})\right) - 2\sin(\delta\theta_{\mathrm{sm}}) \left(\hat{v}_{g,q} \cos(\delta\theta_{\mathrm{sm}}) - \hat{v}_{g,d} \sin(\delta\theta_{\mathrm{sm}})\right)\right)}{2\, T_{\mathrm{ex}} \sqrt{\left(\hat{v}_{g,d} \cos(\delta\theta_{\mathrm{sm}}) + \hat{v}_{g,q} \sin(\delta\theta_{\mathrm{sm}})\right)^2 + \left(\hat{v}_{g,q} \cos(\delta\theta_{\mathrm{sm}}) - \hat{v}_{g,d} \sin(\delta\theta_{\mathrm{sm}})\right)^2}}
\end{pmatrix} \tag{A.10}$$

$$\mathbf{B}_{\mathrm{sm},2} =$$

$$\begin{pmatrix}
-\frac{\omega_b \cos(\delta\theta_{\mathrm{sm}}) \left(l_{11\mathrm{d}}\, l_{\mathrm{ffd}} - {l_{\mathrm{f1d}}}^2\right)}{l_{\mathrm{sm},d}} \\
-\frac{l_{11\mathrm{q}}\, \omega_b \sin(\delta\theta_{\mathrm{sm}})}{l_{\mathrm{sm},q}} \\
-\frac{\omega_b \cos(\delta\theta_{\mathrm{sm}}) \left(l_{11\mathrm{d}}\, l_{\mathrm{ad}} - l_{\mathrm{ad}}\, l_{\mathrm{f1d}}\right)}{l_{\mathrm{sm},d}} \\
\frac{\omega_b \cos(\delta\theta_{\mathrm{sm}}) \left(l_{\mathrm{ad}}\, l_{\mathrm{f1d}} - l_{\mathrm{ad}}\, l_{\mathrm{ffd}}\right)}{l_{\mathrm{sm},d}} \\
-\frac{l_{\mathrm{aq}}\, \omega_b \sin(\delta\theta_{\mathrm{sm}})}{l_{\mathrm{sm},q}} \\
0 \\
0 \\
0 \\
\omega_{f,\mathrm{sm}} \left(i_{\mathrm{sm},q} \cos\left(\delta\theta_{\mathrm{sm}}\right) + i_{\mathrm{sm},d} \sin\left(\delta\theta_{\mathrm{sm}}\right)\right) \\
-\frac{2\cos(\delta\theta_{\mathrm{sm}}) \left(\hat{v}_{g,q} \cos(\delta\theta_{\mathrm{sm}}) - \hat{v}_{g,d} \sin(\delta\theta_{\mathrm{sm}})\right) + 2\sin(\delta\theta_{\mathrm{sm}}) \left(\hat{v}_{g,d} \cos(\delta\theta_{\mathrm{sm}}) + \hat{v}_{g,q} \sin(\delta\theta_{\mathrm{sm}})\right)}{2\sqrt{\left(\hat{v}_{g,d} \cos(\delta\theta_{\mathrm{sm}}) + \hat{v}_{g,q} \sin(\delta\theta_{\mathrm{sm}})\right)^2 + \left(\hat{v}_{g,q} \cos(\delta\theta_{\mathrm{sm}}) - \hat{v}_{g,d} \sin(\delta\theta_{\mathrm{sm}})\right)^2}} \\
-\frac{k_{p,\mathrm{ex}} \left(2\cos(\delta\theta_{\mathrm{sm}}) \left(\hat{v}_{g,q} \cos(\delta\theta_{\mathrm{sm}}) - \hat{v}_{g,d} \sin(\delta\theta_{\mathrm{sm}})\right) + 2\sin(\delta\theta_{\mathrm{sm}}) \left(\hat{v}_{g,d} \cos(\delta\theta_{\mathrm{sm}}) + \hat{v}_{g,q} \sin(\delta\theta_{\mathrm{sm}})\right)\right)}{2\, T_{\mathrm{ex}} \sqrt{\left(\hat{v}_{g,d} \cos(\delta\theta_{\mathrm{sm}}) + \hat{v}_{g,q} \sin(\delta\theta_{\mathrm{sm}})\right)^2 + \left(\hat{v}_{g,q} \cos(\delta\theta_{\mathrm{sm}}) - \hat{v}_{g,d} \sin(\delta\theta_{\mathrm{sm}})\right)^2}}
\end{pmatrix} \tag{A.11}$$

$$\mathbf{B}_{\mathrm{sm},3} = \begin{pmatrix}
0 \\ 0 \\ 0 \\ 0 \\ 0 \\ \frac{k_{d,\mathrm{sm}}}{T_{\mathrm{sm}}} \\ -\omega_b \\ 0 \\ 0 \\ 0 \\ 0
\end{pmatrix} \tag{A.12}$$

$$\mathbf{B}_{\mathrm{sm},4} = \begin{pmatrix} 0 \\ 0 \\ 0 \\ 0 \\ 0 \\ 0 \\ 0 \\ \frac{1}{T_{\mathrm{gt}}} \\ 0 \\ 0 \\ 0 \end{pmatrix} \tag{A.13}$$

$$\mathbf{B}_{\mathrm{sm},5} = \begin{pmatrix} 0 \\ 0 \\ 0 \\ 0 \\ 0 \\ 0 \\ 0 \\ 0 \\ 0 \\ k_{q,\mathrm{sm}} \\ \frac{k_{p,\mathrm{ex}}\, k_{q,\mathrm{sm}}}{T_{\mathrm{ex}}} \end{pmatrix} \tag{A.14}$$

$$\mathbf{B}_{\mathrm{sm},6} = \begin{pmatrix} 0 \\ 0 \\ 0 \\ 0 \\ 0 \\ 0 \\ 0 \\ \frac{k_{\omega,\mathrm{sm}}}{T_{\mathrm{gt}}} \\ 0 \\ 0 \\ 0 \end{pmatrix} \tag{A.15}$$

$$\mathbf{B}_{\mathrm{sm},7} = \begin{pmatrix} 0 \\ 0 \\ 0 \\ 0 \\ 0 \\ 0 \\ 0 \\ 0 \\ 0 \\ 1 \\ \frac{k_{p,\mathrm{ex}}}{T_{\mathrm{ex}}} \end{pmatrix} \tag{A.16}$$

Appendix B

Active load system mathematical model in grid-connected operation

B.1 Non-linear model

The nonlinear equations for the grid-connected active load is given by (B.1.1)-(B.1.14).

$$\begin{aligned}\frac{di_{cv,load,d}}{dt} =& i_{\text{cv,load},q}\,\omega_b - i_{\text{cv,load},q}\,\omega_b\,\omega_g - \frac{i_{\text{cv,load},d}\,\omega_b\,(k_{\text{pc,load}} + r_f)}{l_f} + \frac{k_{\text{ic,load}}\,\gamma_{\text{load},d}\,\omega_b}{l_f} \\ &+ \frac{k_{\text{pc,load}}\,i_{\text{cv,ref,load},d}\,\omega_b}{l_f} + \frac{k_{\text{ad,load}}\,\omega_b\,\phi_{\text{load},d}}{l_f} - \frac{\omega_b\,v_{o,\text{load},d}\,(k_{\text{ad,load}} - k_{\text{ffv}} + 1)}{l_f} \\ &+ k_{i,\text{pll,load}}\,i_{\text{cv,load},q}\,\omega_b\,\varepsilon_{\text{pll,load}}\end{aligned} \tag{B.1.1}$$

$$\begin{aligned}\frac{di_{cv,load,q}}{dt} =& i_{\text{cv,load},d}\,\omega_b - i_{\text{cv,load},d}\,\omega_b\,\omega_g - \frac{i_{\text{cv,load},q}\,\omega_b\,(k_{\text{pc,load}} + r_f)}{l_f} + \frac{k_{\text{ic,load}}\,\gamma_{\text{load},q}\,\omega_b}{l_f} \\ &+ \frac{k_{\text{pc,load}}\,i_{\text{cv,ref,load},q}\,\omega_b}{l_f} + \frac{k_{\text{ad,load}}\,\omega_b\,\phi_{\text{load},q}}{l_f} - \frac{\omega_b\,v_{o,\text{load},q}\,(k_{\text{ad,load}} - k_{\text{ffv}} + 1)}{l_f} \\ &+ k_{i,\text{pll,load}}\,i_{\text{cv,load},d}\,\omega_b\,\varepsilon_{\text{pll,load}}\end{aligned} \tag{B.1.2}$$

$$\frac{dv_{o,load,d}}{dt} = \omega_b\,\omega_g\,v_{o,\text{load},q} + \frac{i_{\text{cv,load},d}\,\omega_b}{c_f} - \frac{i_{o,\text{load},d}\,\omega_b}{c_f} \tag{B.1.3}$$

$$\frac{dv_{o,load,q}}{dt} = \frac{i_{\text{cv,load},q}\,\omega_b}{c_f} - \omega_b\,\omega_g\,v_{o,\text{load},d} - \frac{i_{o,\text{load},q}\,\omega_b}{c_f} \tag{B.1.4}$$

$$\begin{aligned}\frac{di_{o,load,d}}{dt} = \frac{\omega_b\,v_{o,\text{load},d}}{l_g} + i_{o,\text{load},q}\,\omega_b\,\omega_g - \frac{i_{o,\text{load},d}\,\omega_b\,r_g}{l_g} - \frac{\omega_b\,\hat{v}_{g,d}\,\cos(\delta\theta_{\text{pll,load}})}{l_g} \\ - \frac{\omega_b\,\hat{v}_{g,q}\,\sin(\delta\theta_{\text{pll,load}})}{l_g}\end{aligned} \tag{B.1.5}$$

$$\begin{aligned}\frac{di_{o,load,q}}{dt} = \frac{\omega_b\,v_{o,\text{load},q}}{l_g} - i_{o,\text{load},d}\,\omega_b\,\omega_g - \frac{i_{o,\text{load},q}\,\omega_b\,r_g}{l_g} - \frac{\omega_b\,\hat{v}_{g,q}\,\cos(\delta\theta_{\text{pll,load}})}{l_g} \\ + \frac{\omega_b\,\hat{v}_{g,d}\,\sin(\delta\theta_{\text{pll,load}})}{l_g}\end{aligned} \tag{B.1.6}$$

$$\frac{d\gamma_{load,d}}{dt} = i^*_{cv,load,d} - i_{cv,load,d} \tag{B.1.7}$$

$$\frac{d\gamma_{load,q}}{dt} = i^*_{\mathrm{cv,load},d} - i_{\mathrm{cv,load},d} \tag{B.1.8}$$

$$\frac{d\phi_{load,d}}{dt} = \omega_{\mathrm{load,ad}}\, v_{o,\mathrm{load},d} - \omega_{\mathrm{load,ad}}\, \phi_{\mathrm{load},d} \tag{B.1.9}$$

$$\frac{d\phi_{load,q}}{dt} = \omega_{\mathrm{load,ad}}\, v_{o,\mathrm{load},q} - \omega_{\mathrm{load,ad}}\, \phi_{\mathrm{load},q} \tag{B.1.10}$$

$$\frac{dv_{pll,load,d}}{dt} = \omega_{\mathrm{lp,pll}}\, v_{o,\mathrm{load},d} - \omega_{\mathrm{lp,pll}}\, v_{\mathrm{pll,load},d} \tag{B.1.11}$$

$$\frac{dv_{pll,load,q}}{dt} = \omega_{\mathrm{lp,pll}}\, v_{o,\mathrm{load},q} - \omega_{\mathrm{lp,pll}}\, v_{\mathrm{pll,load},q} \tag{B.1.12}$$

$$\frac{d\varepsilon_{pll,load}}{dt} = \tan^{-1}\left(\frac{v_{\mathrm{pll,load},q}}{v_{\mathrm{pll,load},d}}\right) \tag{B.1.13}$$

$$\frac{d\delta\theta_{pll,load}}{dt} = \omega_b\, k_{p,\mathrm{pll,load}}\, \tan^{-1}\left(\frac{v_{\mathrm{pll,load},q}}{v_{\mathrm{pll,load},d}}\right) + \omega_b\, k_{i,\mathrm{pll,load}}\, \varepsilon_{\mathrm{pll,load}} \tag{B.1.14}$$

B.2 Small-signal model

By linearization of the nonlinear model (B.1.1)-(B.1.14), the small-signal state-space model has been derived, with the form given by (B.15) where Δ indicates the small-signal deviations around the steady-state operating point. For convenience of notation, $\mathbf{A}_{\text{load}}$ is expressed through 4 sub-matrices (B.18)-(B.20) as shown in (B.16).

$$\boldsymbol{\Delta}\dot{\mathbf{x}}_{\text{load}} = \frac{\mathrm{d}}{\mathrm{d}t}\boldsymbol{\Delta}\mathbf{x}_{\text{load}} = \mathbf{A}_{\text{load}}\boldsymbol{\Delta}\mathbf{x}_{\text{load}} + \mathbf{B}_{\text{load}}\boldsymbol{\Delta}\mathbf{u}_{\text{load}} \tag{B.15}$$

$$\mathbf{A}_{\text{load}} = \begin{bmatrix} \mathbf{A}_{\text{load},1} & \mathbf{A}_{\text{load},2} \\ \mathbf{A}_{\text{load},3} & \mathbf{A}_{\text{load},4} \end{bmatrix} \tag{B.16}$$

$$\mathbf{B}_{\text{load}} = \begin{bmatrix} \frac{k_{\text{pc,load}}\,\omega_b}{l_f} & 0 & 0 & 0 & -i_{\text{cv,load},q}\,\omega_b \\ 0 & \frac{k_{\text{pc,load}}\,\omega_b}{l_f} & 0 & 0 & -i_{\text{cv,load},d}\,\omega_b \\ 0 & 0 & 0 & 0 & \omega_b\, v_{o,\text{load},q} \\ 0 & 0 & 0 & 0 & -\omega_b\, v_{o,\text{load},d} \\ 0 & 0 & -\frac{\omega_b\,\cos\left(\delta\theta_{\text{pll,load}}\right)}{l_g} & -\frac{\omega_b\,\sin\left(\delta\theta_{\text{pll,load}}\right)}{l_g} & i_{o,\text{load},q}\,\omega_b \\ 0 & 0 & \frac{\omega_b\,\sin\left(\delta\theta_{\text{pll,load}}\right)}{l_g} & -\frac{\omega_b\,\cos\left(\delta\theta_{\text{pll,load}}\right)}{l_g} & -i_{o,\text{load},d}\,\omega_b \\ 1 & 0 & 0 & 0 & 0 \\ 0 & 1 & 0 & 0 & 0 \\ 0 & 0 & 0 & 0 & 0 \\ 0 & 0 & 0 & 0 & 0 \\ 0 & 0 & 0 & 0 & 0 \\ 0 & 0 & 0 & 0 & 0 \\ 0 & 0 & 0 & 0 & 0 \\ 0 & 0 & 0 & 0 & 0 \end{bmatrix} \tag{B.17}$$

$$\mathbf{A}_{\text{load},3} = \begin{pmatrix} 0 & -1 & 0 & 0 & 0 & 0 & 0 \\ 0 & 0 & \omega_{\text{load,ad}} & 0 & 0 & 0 & 0 \\ 0 & 0 & 0 & \omega_{\text{load,ad}} & 0 & 0 & 0 \\ 0 & 0 & \omega_{\text{lp,pll}} & 0 & 0 & 0 & 0 \\ 0 & 0 & 0 & \omega_{\text{lp,pll}} & 0 & 0 & 0 \\ 0 & 0 & 0 & 0 & 0 & 0 & 0 \\ 0 & 0 & 0 & 0 & 0 & 0 & 0 \end{pmatrix} \tag{B.18}$$

$$\mathbf{A}_{\text{load},1} = \begin{pmatrix} -\frac{\omega_b\left(k_{\text{pc,load}}+r_f\right)}{l_f} & \omega_b - \omega_b\,\omega_g + k_{i,\text{pll,load}}\,\omega_b\,\varepsilon_{\text{pll,load}} & -\frac{\omega_b\left(k_{\text{ad,load}}-k_{\text{ffv}}+1\right)}{l_f} & 0 & 0 & 0 & \frac{k_{\text{ic,load}}\,\omega_b}{l_f} \\ \omega_b - \omega_b\,\omega_g + k_{i,\text{pll,load}}\,\omega_b\,\varepsilon_{\text{pll,load}} & -\frac{\omega_b\left(k_{\text{pc,load}}+r_f\right)}{l_f} & 0 & -\frac{\omega_b\left(k_{\text{ad,load}}-k_{\text{ffv}}+1\right)}{l_f} & 0 & 0 & 0 \\ \frac{\omega_b}{c_f} & 0 & 0 & \omega_b\,\omega_g & -\frac{\omega_b}{c_f} & 0 & 0 \\ 0 & \frac{\omega_b}{c_f} & -\omega_b\,\omega_g & 0 & 0 & -\frac{\omega_b}{c_f} & 0 \\ 0 & 0 & \frac{\omega_b}{l_g} & 0 & -\frac{\omega_b\,r_g}{l_g} & \omega_b\,\omega_g & 0 \\ 0 & 0 & 0 & \frac{\omega_b}{l_g} & -\omega_b\,\omega_g & -\frac{\omega_b\,r_g}{l_g} & 0 \\ -1 & 0 & 0 & 0 & 0 & 0 & 0 \end{pmatrix} \tag{B.19}$$

$$\mathbf{A}_{\text{load},2} = \begin{pmatrix} 0 & \frac{k_{\text{ad,load}}\,\omega_b}{l_f} & 0 & 0 & 0 & i_{\text{cv,load},q}\,k_{i,\text{pll,load}}\,\omega_b & 0 \\ \frac{k_{\text{ic,load}}\,\omega_b}{l_f} & 0 & \frac{k_{\text{ad,load}}\,\omega_b}{l_f} & 0 & 0 & i_{\text{cv,load},d}\,k_{i,\text{pll,load}}\,\omega_b & 0 \\ 0 & 0 & 0 & 0 & 0 & 0 & 0 \\ 0 & 0 & 0 & 0 & 0 & 0 & 0 \\ 0 & 0 & 0 & 0 & 0 & 0 & \frac{\hat{v}_{g,d}\,\omega_b\,\sin\left(\delta\theta_{\text{pll,load}}\right)}{l_g} - \frac{\hat{v}_{g,q}\,\omega_b\,\cos\left(\delta\theta_{\text{pll,load}}\right)}{l_g} \\ 0 & 0 & 0 & 0 & 0 & 0 & \frac{\hat{v}_{g,d}\,\omega_b\,\cos\left(\delta\theta_{\text{pll,load}}\right)}{l_g} + \frac{\hat{v}_{g,q}\,\omega_b\,\sin\left(\delta\theta_{\text{pll,load}}\right)}{l_g} \\ 0 & 0 & 0 & 0 & 0 & 0 & 0 \end{pmatrix} \tag{B.20}$$

$$\mathbf{A}_{\text{load},4} =$$

$$\begin{pmatrix}
0 & 0 & 0 & 0 & 0 & 0 & 0 \\
0 & -\omega_{\text{load,ad}} & 0 & 0 & 0 & 0 & 0 \\
0 & 0 & -\omega_{\text{load,ad}} & 0 & 0 & 0 & 0 \\
0 & 0 & 0 & -\omega_{\text{lp,pll}} & 0 & 0 & 0 \\
0 & 0 & 0 & 0 & -\omega_{\text{lp,pll}} & 0 & 0 \\
0 & 0 & 0 & -\frac{\text{imag}\left(v_{\text{pll,load},d}\right)+\text{real}\left(v_{\text{pll,load},q}\right)}{nu_{load}} & -\frac{\text{imag}\left(v_{\text{pll,load},q}\right)-\text{real}\left(v_{\text{pll,load},d}\right)}{nu_{load}} & 0 & 0 \\
0 & 0 & 0 & -\frac{k_{p,\text{pll,load}}\,\omega_b\left(\text{imag}\left(v_{\text{pll,load},d}\right)+\text{real}\left(v_{\text{pll,load},q}\right)\right)}{nu_{load}} & -\frac{k_{p,\text{pll,load}}\,\omega_b\left(\text{imag}\left(v_{\text{pll,load},q}\right)-\text{real}\left(v_{\text{pll,load},d}\right)\right)}{nu_{load}} & k_{i,\text{pll,load}}\,\omega_b & 0
\end{pmatrix} \tag{B.21}$$

$$nu_{load} = \left(\text{imag}\left(v_{\text{pll,load},d}\right) + \text{real}\left(v_{\text{pll,load},q}\right)\right)^2 + \left(\text{imag}\left(v_{\text{pll,load},q}\right) - \text{real}\left(v_{\text{pll,load},d}\right)\right)^2$$

Appendix C

Virtual synchronous machine system mathematical model in grid-connected operation

The nonlinear equations for the grid-connected VSM is given by (C.1.1)-(C.1.20).

C.1 Non-linear model

$$\begin{aligned}\frac{di_{cv,d}}{dt} =& -\frac{\omega_b\left(1-k_{ffv}+k_{ad}\right)}{l_f}v_{o,d,vsm}+\frac{\omega_b k_{pc}r_s\left(k_{ffe}-k_{pv}\right)}{l_f\left(r_s^2+\omega_{vsm}^2l_s^2\right)}\sqrt{v_{o,d,vsm}^2+v_{o,q,vsm}^2}\\ &-\frac{\omega_b\left(k_{pc}+r_f\right)}{l_f}i_{cv,d,vsm}+\frac{\omega_b k_{ic}}{l_f}\gamma_d-\frac{\omega_b k_{ad}}{l_f}\varphi_d+\frac{\omega_b k_{pc}k_{iv}r_s}{l_f\left(r_s^2+\omega_{vsm}^2l_s^2\right)}\xi\\ &-\frac{\omega_b k_{pc}k_{pv}r_s}{l_f\left(r_s^2+\omega_{vsm}^2l_s^2\right)}v_{m,d,vsm}-\frac{\omega_b k_{pc}l_s}{l_f\left(r_s^2+\omega_{vsm}^2l_s^2\right)}\omega_{vsm}v_{m,q,vsm}\\ &-\frac{\omega_b k_{pc}k_{pv}k_qr_s}{l_f\left(r_s^{2c}+\omega_{vsm}^2l_s^2\right)}q_m+\frac{\omega_b k_{pc}k_{pv}k_qr_s}{l_f\left(r_s^2+\omega_{vsm}^2l_s^2\right)}q_{vsm}^*+\frac{\omega_b k_{pc}k_{pv}r_s}{l_f\left(r_s^2+\omega_{vsm}^2l_s^2\right)}\hat{v}^*\end{aligned} \tag{C.1.1}$$

$$\begin{aligned}\frac{di_{cv,q}}{dt} =& -\frac{\omega_b\left(1-k_{fi}+k_{ad}\right)}{l_f}v_{o,q}-\frac{\omega_b k_{pc}l_s\left(k_{ffe}-k_{pv}\right)}{l_f\left(r_s^2+\omega_{vsm}^2l_s^2\right)}\omega_{vsm}\sqrt{v_{o,d}^2+v_{o,q}^2}\\ &-\frac{\omega_b\left(k_{pc}+r_f\right)}{l_f}i_{cv,q}+\frac{\omega_b k_{ic}}{l_f}\gamma_q-\frac{\omega_b k_{ad}}{l_f}\varphi_q-\frac{\omega_b k_{pc}k_{iv}l_s}{l_f\left(r_s^2+\omega_{vsm}^2l_s^2\right)}\omega_{vsm}\xi\\ &+\frac{\omega_b k_{pc}l_s}{l_f\left(r_s^2+\omega_{vsm}^2l_s^2\right)}\omega_{vsm}v_{m,d}-\frac{\omega_b k_{pc}r_s}{l_f\left(r_s^2+\omega_{vsm}^2l_s^2\right)}v_{m,q}+\frac{\omega_b k_{pc}k_{pv}k_ql_s}{l_f\left(r_s^2+\omega_{vsm}^2l_s^2\right)}\omega_{vsm}q_m\\ &-\frac{\omega_b k_{pc}k_{pv}k_ql_s}{l_f\left(r_s^2+\omega_{vsm}^2l_s^2\right)}\omega_{vsm}q^*-\frac{\omega_b k_{pc}k_{pv}l_s}{l_f\left(r_s^2+\omega_{vsm}^2l_s^2\right)}\omega_{vsm}\hat{v}^*\end{aligned} \tag{C.1.2}$$

$$\frac{dv_{o,vsm,d}}{dt} = \omega_b\omega_{vsm}v_{o,q}+\frac{\omega_b}{c_f}i_{cv,d}-\frac{\omega_b}{c_f}i_{o,d} \tag{C.1.3}$$

$$\frac{dv_{o,vsm,q}}{dt} = -\omega_b\omega_{vsm}v_{o,d}+\frac{\omega_b}{c_f}i_{cv,q}-\frac{\omega_b}{c_f}i_{o,q} \tag{C.1.4}$$

$$\frac{di_{o,vsm,d}}{dt} = \frac{\omega_b}{l_g}v_{o,vsm,d}-\frac{\omega_b r_g}{l_g}i_{o,vsm,d}+\omega_b\omega_{vsm}i_{o,vsm,q}-\frac{\omega_b}{l_g}\hat{v}_{g,d}\cos\left(\delta\theta_{vsm}\right)-\frac{\omega_b}{l_g}\hat{v}_{g,q}\sin\left(\delta\theta_{vsm}\right) \tag{C.1.5}$$

$$\frac{di_{o,vsm,q}}{dt} = \frac{\omega_b}{l_g} v_{o,vsm,q} - \frac{\omega_b r_g}{l_g} i_{o,vsm,q} - \omega_b \omega_{vsm} i_{o,vsm,d} - \frac{\omega_b}{l_g} \hat{v}_{g,q} \cos\left(\delta\theta_{vsm}\right) + \frac{\omega_b}{l_g} \hat{v}_{g,d} \sin\left(\delta\theta_{vsm}\right) \quad \text{(C.1.6)}$$

$$\begin{aligned}\frac{d\gamma_{vsm,d}}{dt} =& - i_{cv,d} + \frac{r_s\left(k_{ffe} - k_{pv}\right)}{r_s^2 + \omega_{VSM}^2 l_s^2}\sqrt{v_{o,d}^2 + v_{o,q}^2} + \frac{k_{iv} r_s}{r_s^2 + \omega_{VSM}^2 l_s^2}\xi - \frac{r_s}{r_s^2 + \omega_{VSM}^2 l_s^2} v_{m,d} \\ & - \frac{l_s}{r_s^2 + \omega_{VSM}^2 l_s^2}\omega_{VSM} v_{m,q} - \frac{k_{pv} k_q r_s}{r_s^2 + \omega_{VSM}^2 l_s^2} q_m + \frac{k_{pv} k_q r_s}{r_s^2 + \omega_{VSM}^2 l_s^2} q^* + \frac{k_{pv} r_s}{r_s^2 + \omega_{VSM}^2 l_s^2}\hat{v}^*\end{aligned} \quad \text{(C.1.7)}$$

$$\begin{aligned}\frac{d\gamma_{vsm,q}}{dt} =& - i_{cv,q} - \frac{l_s\left(k_{ffe} - k_{pv}\right)}{r_s^2 + \omega_{VSM}^2 l_s^2}\omega_{VSM}\sqrt{v_{o,d}^2 + v_{o,q}^2} - \frac{k_{iv} l_s}{r_s^2 + \omega_{VSM}^2 l_s^2}\omega_{VSM}\xi \\ & + \frac{l_s}{r_s^2 + \omega_{VSM}^2 l_s^2}\omega_{VSM} v_{m,d} - \frac{r_s}{r_s^2 + \omega_{VSM}^2 l_s^2} v_{m,q} + \frac{k_{pv} k_q l_s}{r_s^2 + \omega_{VSM}^2 l_s^2}\omega_{VSM} q_m \\ & - \frac{k_{pv} k_q l_s}{r_s^2 + \omega_{VSM}^2 l_s^2}\omega_{VSM} q^* - \frac{k_{pv} l_s}{r_s^2 + \omega_{VSM}^2 l_s^2}\omega_{VSM}\hat{v}^*\end{aligned} \quad \text{(C.1.8)}$$

$$\frac{d\varphi_d}{dt} = -\omega_{ad} v_{o,vsm,d} - \omega_{ad}\varphi_d \quad \text{(C.1.9)}$$

$$\frac{d\varphi_q}{dt} = -\omega_{ad} v_{o,vsm,q} - \omega_{ad}\varphi_q \quad \text{(C.1.10)}$$

$$\frac{dv_{m,d}}{dt} = \omega_{vf} v_{o,d} - \omega_{vf} v_{m,d} \quad \text{(C.1.11)}$$

$$\frac{dv_{m,q}}{dt} = \omega_{vf} v_{o,sq} - \omega_{vf} v_{m,q} \quad \text{(C.1.12)}$$

$$\begin{aligned}\frac{dv_{pll,vsm,d}}{dt} =& \omega_{lp,pll} v_{0,vsm,d} \cos\left(\delta\theta_{pll,vsm} - \delta\theta_{vsm}\right) \\ & + \omega_{lp,pll} v_{0,vsm,q} \sin\left(\delta\theta_{pll,vsm} - \delta\theta_{vsm}\right) - \omega_{lp,pll} v_{pll,vsm,d}\end{aligned} \quad \text{(C.1.13)}$$

$$\begin{aligned}\frac{dv_{pll,vsm,q}}{dt} =& - \omega_{lp,pll} v_{o,vsm,d} \sin\left(\delta\theta_{pll,vsm} - \delta\theta_{vsm}\right) \\ & + \omega_{lp,pll} v_{o,vsm,q} \cos\left(\delta\theta_{pll,vsm} - \delta\theta_{vsm}\right) - \omega_{lp,pll} v_{pll,vsm,q}\end{aligned} \quad \text{(C.1.14)}$$

$$\frac{d\varepsilon_{pll,vsm}}{dt} = \tan^{-1}\left(\frac{v_{pll,vsm,q}}{v_{pll,vsm,d}}\right) \quad \text{(C.1.15)}$$

$$\frac{d\xi}{dt} = \left(\hat{v}^* - \sqrt{v_{o,d}^2 v_{o,q}^2}\right) + \left(k_q q_{vsm}^* - k_q q_{m,vsm}\right) \quad \text{(C.1.16)}$$

$$\frac{dq_m}{dt} = -\omega_f i_{o,q} v_{o,d} + \omega_f i_{o,d} v_{o,q} - \omega_f q_{qf} \quad \text{(C.1.17)}$$

$$\begin{aligned}\frac{d\omega_{vsm}}{dt} =& - \frac{1}{T_a} i_{o,vsm,d} v_{o,vsm,d} - \frac{1}{T_a} i_{o,vsm,q} v_{o,vsm,q} - \frac{\left(k_d + k_\omega\right)}{T_a}\delta\omega_{vsm} \\ & + \frac{k_d k_{p,pll}}{T_a}\tan^{-1}\left(\frac{v_{pll,vsm,q}}{v_{pll,vsm,d}}\right) + \frac{k_d k_{i,pll}}{T_a}\varepsilon_{pll} + \frac{1}{T_a} p_{vsm}^* + \frac{k_\omega}{T_a}\omega_{vsm}^* - \frac{k_\omega}{T_a}\omega_g\end{aligned} \quad \text{(C.1.18)}$$

$$\frac{d\delta\theta_{pll,vsm}}{dt} = \omega_b k_{p,pll} \tan^{-1}\left(\frac{v_{pll,vsm,q}}{v_{pll,vsm,d}}\right) + \omega_b k_{i,pll}\varepsilon_{pll} \tag{C.1.19}$$

$$\frac{d\delta\theta_{vsm}}{dt} = \omega_b\omega_{vsm} - \omega_b\omega_g \tag{C.1.20}$$

C.2 Small-signal model

By linearization of the nonlinear model (C.1.1)-(C.1.20), the small-signal state-space model has been derived, with the form given by (C.21) where Δ indicates the small-signal deviations around the steady-state operating point. For convenience of notation, $\mathbf{A}_{\text{load}}$ is expressed through 4 sub-matrices (C.23)-(C.26) as shown in (C.22).

$$\boldsymbol{\Delta}\dot{\mathbf{x}}_{\text{vsm}} = \frac{\mathrm{d}}{\mathrm{d}t}\boldsymbol{\Delta}\mathbf{x}_{\text{vsm}} = \mathbf{A}_{\text{vsm}}\boldsymbol{\Delta}\mathbf{x}_{\text{vsm}} + \mathbf{B}_{\text{vsm}}\boldsymbol{\Delta}\mathbf{u}_{\text{vsm}} \tag{C.21}$$

$$\mathbf{A}_{\text{vsm}} = \begin{bmatrix} \mathbf{A}_{\text{vsm},1} & \mathbf{A}_{\text{vsm},2} \\ \mathbf{A}_{\text{vsm},3} & \mathbf{A}_{\text{vsm},4} \end{bmatrix} \tag{C.22}$$

$$\mathbf{A}_{\text{vsm},2} = \begin{pmatrix} 0 & \frac{k_{\text{ic,vsm}}\,\omega_b}{l_f} & 0 & -\frac{k_{\text{ad,vsm}}\,\omega_b}{l_f} & 0 \\ 0 & 0 & \frac{k_{\text{ic,vsm}}\,\omega_b}{l_f} & 0 & -\frac{k_{\text{ad,vsm}}\,\omega_b}{l_f} \\ 0 & 0 & 0 & 0 & 0 \\ -\frac{\omega_b}{c_f} & 0 & 0 & 0 & 0 \\ \omega_b\,\omega_{\text{vsm}} & 0 & 0 & 0 & 0 \end{pmatrix} \tag{C.23}$$

$$\mathbf{A}_{\text{vsm},4} = \begin{pmatrix} -\frac{\omega_b\,r_g}{l_g} & 0 & 0 & 0 & 0 \\ 0 & 0 & 0 & 0 & 0 \\ 0 & 0 & 0 & 0 & 0 \\ 0 & 0 & 0 & -\omega_{\text{ad,vsm}} & 0 \\ 0 & 0 & 0 & 0 & -\omega_{\text{ad,vsm}} \end{pmatrix} \tag{C.24}$$

$$\mathbf{A}_{\mathrm{vsm},1} = \begin{pmatrix} -\frac{\omega_b\left(k_{\mathrm{pc,vsm}}+r_f\right)}{l_f} & 0 & \frac{k_{\mathrm{pc,vsm}}\,\omega_b\,r_{s,\mathrm{vsm}}\,v_{o,\mathrm{vsm},d}\,(k_{\mathrm{ffe}}-k_{\mathrm{pv}})}{l_f\,\sqrt{{v_{o,\mathrm{vsm},d}}^2+{v_{o,\mathrm{vsm},q}}^2}\left({l_{s,\mathrm{vsm}}}^2\,{\omega_{\mathrm{vsm}}}^2+{r_{s,\mathrm{vsm}}}^2\right)} - \frac{\omega_b\left(k_{\mathrm{ad,vsm}}-k_{\mathrm{ffv}}+1\right)}{l_f} \\ 0 & -\frac{\omega_b\left(k_{\mathrm{pc,vsm}}+r_f\right)}{l_f} & -\frac{k_{\mathrm{pc,vsm}}\,l_{s,\mathrm{vsm}}\,\omega_b\,\omega_{\mathrm{vsm}}\,v_{o,\mathrm{vsm},d}\,(k_{\mathrm{ffe}}-k_{\mathrm{pv}})}{l_f\,\sqrt{{v_{o,\mathrm{vsm},d}}^2+{v_{o,\mathrm{vsm},q}}^2}\left({l_{s,\mathrm{vsm}}}^2\,{\omega_{\mathrm{vsm}}}^2+{r_{s,\mathrm{vsm}}}^2\right)} \\ \frac{\omega_b}{c_f} & 0 & 0 \\ 0 & \frac{\omega_b}{c_f} & -\omega_b\,\omega_{\mathrm{vsm}} \\ 0 & 0 & \frac{\omega_b}{l_g} \end{pmatrix} \tag{C.25}$$

$$\begin{pmatrix} \frac{k_{\mathrm{pc,vsm}}\,\omega_b\,r_{s,\mathrm{vsm}}\,v_{o,\mathrm{vsm},q}\,(k_{\mathrm{ffe}}-k_{\mathrm{pv}})}{l_f\,\sqrt{{v_{o,\mathrm{vsm},d}}^2+{v_{o,\mathrm{vsm},q}}^2}\left({l_{s,\mathrm{vsm}}}^2\,{\omega_{\mathrm{vsm}}}^2+{r_{s,\mathrm{vsm}}}^2\right)} & 0 \\ -\frac{\omega_b\left(k_{\mathrm{ad,vsm}}-k_{\mathrm{ffv}}+1\right)}{l_f} - \frac{k_{\mathrm{pc,vsm}}\,l_{s,\mathrm{vsm}}\,\omega_b\,\omega_{\mathrm{vsm}}\,v_{o,\mathrm{vsm},q}\,(k_{\mathrm{ffe}}-k_{\mathrm{pv}})}{l_f\,\sqrt{{v_{o,\mathrm{vsm},d}}^2+{v_{o,\mathrm{vsm},q}}^2}\left({l_{s,\mathrm{vsm}}}^2\,{\omega_{\mathrm{vsm}}}^2+{r_{s,\mathrm{vsm}}}^2\right)} & 0 \\ \omega_b\,\omega_{\mathrm{vsm}} & -\frac{\omega_b}{c_f} \\ 0 & 0 \\ 0 & -\frac{\omega_b\,r_g}{l_g} \end{pmatrix}$$

$$\mathbf{A}_{\mathrm{vsm},3} = \begin{pmatrix} 0 & 0 & 0 & \frac{\omega_b}{l_g} & -\omega_b\,\omega_{\mathrm{vsm}} \\ -1 & 0 & \frac{r_{s,\mathrm{vsm}}\,v_{o,\mathrm{vsm},d}\,(k_{\mathrm{ffe}}-k_{\mathrm{pv}})}{\sqrt{{v_{o,\mathrm{vsm},d}}^2+{v_{o,\mathrm{vsm},q}}^2}\left({l_{s,\mathrm{vsm}}}^2\,{\omega_{\mathrm{vsm}}}^2+{r_{s,\mathrm{vsm}}}^2\right)} & \frac{r_{s,\mathrm{vsm}}\,v_{o,\mathrm{vsm},q}\,(k_{\mathrm{ffe}}-k_{\mathrm{pv}})}{\sqrt{{v_{o,\mathrm{vsm},d}}^2+{v_{o,\mathrm{vsm},q}}^2}\left({l_{s,\mathrm{vsm}}}^2\,{\omega_{\mathrm{vsm}}}^2+{r_{s,\mathrm{vsm}}}^2\right)} & 0 \\ 0 & -1 & -\frac{l_{s,\mathrm{vsm}}\,\omega_{\mathrm{vsm}}\,v_{o,\mathrm{vsm},d}\,(k_{\mathrm{ffe}}-k_{\mathrm{pv}})}{\sqrt{{v_{o,\mathrm{vsm},d}}^2+{v_{o,\mathrm{vsm},q}}^2}\left({l_{s,\mathrm{vsm}}}^2\,{\omega_{\mathrm{vsm}}}^2+{r_{s,\mathrm{vsm}}}^2\right)} & -\frac{l_{s,\mathrm{vsm}}\,\omega_{\mathrm{vsm}}\,v_{o,\mathrm{vsm},q}\,(k_{\mathrm{ffe}}-k_{\mathrm{pv}})}{\sqrt{{v_{o,\mathrm{vsm},d}}^2+{v_{o,\mathrm{vsm},q}}^2}\left({l_{s,\mathrm{vsm}}}^2\,{\omega_{\mathrm{vsm}}}^2+{r_{s,\mathrm{vsm}}}^2\right)} & 0 \\ 0 & 0 & -\omega_{\mathrm{ad,vsm}} & 0 & 0 \\ 0 & 0 & 0 & -\omega_{\mathrm{ad,vsm}} & 0 \end{pmatrix} \tag{C.26}$$

$$\mathbf{B}_{\text{vsm}} = \begin{bmatrix} 0 & \frac{k_{q,\text{vsm}}\, k_{\text{pv}}\, k_{\text{pc,vsm}}\, \omega_b\, r_{s,\text{vsm}}}{l_f \left({l_{s,\text{vsm}}}^2\, {\omega_{\text{vsm}}}^2 + {r_{s,\text{vsm}}}^2 \right)} & 0 & 0 & \frac{k_{\text{pv}}\, k_{\text{pc,vsm}}\, \omega_b\, r_{s,\text{vsm}}}{l_f \left({l_{s,\text{vsm}}}^2\, {\omega_{\text{vsm}}}^2 + {r_{s,\text{vsm}}}^2 \right)} & 0 & 0 \\ 0 & -\frac{k_{q,\text{vsm}}\, k_{\text{pv}}\, k_{\text{pc,vsm}}\, l_{s,\text{vsm}}\, \omega_b\, \omega_{\text{vsm}}}{l_f \left({l_{s,\text{vsm}}}^2\, {\omega_{\text{vsm}}}^2 + {r_{s,\text{vsm}}}^2 \right)} & 0 & 0 & -\frac{k_{\text{pv}}\, k_{\text{pc,vsm}}\, l_{s,\text{vsm}}\, \omega_b\, \omega_{\text{vsm}}}{l_f \left({l_{s,\text{vsm}}}^2\, {\omega_{\text{vsm}}}^2 + {r_{s,\text{vsm}}}^2 \right)} & 0 & 0 \\ 0 & 0 & 0 & 0 & 0 & 0 & 0 \\ 0 & 0 & 0 & 0 & 0 & 0 & 0 \\ 0 & 0 & -\frac{\omega_b\, \cos(\delta\theta_{\text{vsm}})}{l_g} & -\frac{\omega_b\, \sin(\delta\theta_{\text{vsm}})}{l_g} & 0 & 0 & 0 \\ 0 & 0 & \frac{\omega_b\, \sin(\delta\theta_{\text{vsm}})}{l_g} & -\frac{\omega_b\, \cos(\delta\theta_{\text{vsm}})}{l_g} & 0 & 0 & 0 \\ 0 & \frac{k_{q,\text{vsm}}\, k_{\text{pv}}\, r_{s,\text{vsm}}}{{l_{s,\text{vsm}}}^2\, {\omega_{\text{vsm}}}^2 + {r_{s,\text{vsm}}}^2} & 0 & 0 & \frac{k_{\text{pv}}\, r_{s,\text{vsm}}}{{l_{s,\text{vsm}}}^2\, {\omega_{\text{vsm}}}^2 + {r_{s,\text{vsm}}}^2} & 0 & 0 \\ 0 & -\frac{k_{q,\text{vsm}}\, k_{\text{pv}}\, l_{s,\text{vsm}}\, \omega_{\text{vsm}}}{{l_{s,\text{vsm}}}^2\, {\omega_{\text{vsm}}}^2 + {r_{s,\text{vsm}}}^2} & 0 & 0 & -\frac{k_{\text{pv}}\, l_{s,\text{vsm}}\, \omega_{\text{vsm}}}{{l_{s,\text{vsm}}}^2\, {\omega_{\text{vsm}}}^2 + {r_{s,\text{vsm}}}^2} & 0 & 0 \\ 0 & 0 & 0 & 0 & 0 & 0 & 0 \\ 0 & 0 & 0 & 0 & 0 & 0 & 0 \\ 0 & 0 & 0 & 0 & 0 & 0 & 0 \\ 0 & 0 & 0 & 0 & 0 & 0 & 0 \\ 0 & 0 & 0 & 0 & 0 & 0 & 0 \\ 0 & 0 & 0 & 0 & 0 & 0 & 0 \\ 0 & 0 & 0 & 0 & 0 & 0 & 0 \\ 0 & 0 & 0 & 0 & 0 & 0 & 0 \\ 0 & k_{q,\text{vsm}} & 0 & 0 & 1 & 0 & 0 \\ 0 & 0 & 0 & 0 & 0 & 0 & 0 \\ \frac{1}{T_a} & 0 & 0 & 0 & 0 & \frac{k_\omega}{T_a} & 0 \\ 0 & 0 & 0 & 0 & 0 & 0 & -\omega_b \end{bmatrix} \tag{C.27}$$

Bibliography

[1] *About - SEAM.* URL: https://seam.no/about/.

[2] ABS. "Abs Advisory on Hybrid Electric Table of Contents." In: (2014), p. 44.

[3] Seon Ju Ahn et al. "Power-sharing method of multiple distributed generators considering control modes and configurations of a microgrid." In: *IEEE Transactions on Power Delivery* 25.3 (2010), pp. 2007–2016.

[4] *Battery and hybrid ships - DNV.* URL: https://www.dnv.com/maritime/advisory/battery-hybrid-ship-service.html.

[5] Hans Peter Beck and Ralf Hesse. "Virtual synchronous machine." In: *2007 9th International Conference on Electrical Power Quality and Utilisation, EPQU* (2007).

[6] Vladimir Blasko and Vikram Kaura. "A new mathematical model and control of a three-phase AC-DC voltage source converter." In: *IEEE Transactions on Power Electronics* 12.1 (1997), pp. 116–123.

[7] Nathaniel Bottrell, Milan Prodanovic, and Timothy C. Green. "Dynamic stability of a microgrid with an active load." In: *IEEE Transactions on Power Electronics* 28.11 (2013), pp. 5107–5119.

[8] Emir Çabukoglu et al. "Battery electric propulsion: an option for heavy-duty vehicles? Results from a Swiss case-study." In: *Transportation Research Part C: Emerging Technologies* 88.February (2018), pp. 107–123. URL: https://doi.org/10.1016/j.trc.2018.01.013.

[9] Juan Manuel Carrasco et al. "Power-electronic systems for the grid integration of renewable energy sources: A survey." In: *IEEE Transactions on Industrial Electronics* 53.4 (2006), pp. 1002–1016.

[10] Meng Chen, Dao Zhou, and Frede Blaabjerg. "Modelling, Implementation, and Assessment of Virtual Synchronous Generator in Power Systems." In: *Journal of Modern Power Systems and Clean Energy* 8.3 (2020), pp. 399–411.

[11] Yong Chen et al. "Improving the grid power quality using virtual synchronous machines." In: *International Conference on Power Engineering, Energy and Electrical Drives* May (2011), pp. 1–6.

[12] Yong Chen et al. "Investigation of the virtual synchronous machine in the island mode." In: *IEEE PES Innovative Smart Grid Technologies Conference Europe* (2012), pp. 1–6.

[13] Salvatore Daarco and Jon Are Suul. "Small-Signal analysis of an isolated power system controlled by a virtual synchronous machine." In: *Proceedings - 2016 IEEE International Power Electronics and Motion Control Conference, PEMC 2016* (2016), pp. 462–469.

[14] Salvatore D'Arco and Jon Are Suul. "Virtual synchronous machines - Classification of implementations and analysis of equivalence to droop controllers for microgrids." In: *2013 IEEE Grenoble Conference PowerTech, POWERTECH 2013* (2013).

[15] Salvatore D'Arco, Jon Are Suul, and Olav B. Fosso. "A Virtual Synchronous Machine implementation for distributed control of power converters in SmartGrids." In: *Electric Power Systems Research* 122 (May 2015), pp. 180–197.

[16] Salvatore D'Arco, Jon Are Suul, and Olav B. Fosso. "Small-signal modeling and parametric sensitivity of a virtual synchronous machine in islanded operation." In: *International Journal of Electrical Power and Energy Systems* 72 (2015), pp. 3–15. URL: http://dx.doi.org/10.1016/j.ijepes.2015.02.005.

[17] *Electric and hybrid propulsion systems for marine vessels - The Explorer*. URL: https://www.theexplorer.no/solutions/electric-and-hybrid-propulsion-systems-for-marine-vessels/.

[18] *Electric Ships Market Size, Share, Growth | Industry Report, 2027*. URL: https://www.fortunebusinessinsights.com/electric-ships-market-104444.

[19] *Electric Solutions | ABB Marine & Ports*. URL: https://new.abb.com/marine/systems-and-solutions/electric-solutions.

[20] Jingyang Fang et al. "On the Inertia of Future More-Electronics Power Systems." In: *IEEE Journal of Emerging and Selected Topics in Power Electronics* 7.4 (2019), pp. 2130–2146.

[21] R. D. Geertsma et al. "Design and control of hybrid power and propulsion systems for smart ships: A review of developments." In: *Applied Energy* 194 (2017), pp. 30–54. URL: http://dx.doi.org/10.1016/j.apenergy.2017.02.060.

[22] *Great hybrid solution for retrofitting | EST-Floattech*. URL: https://www.est-floattech.com/great-hybrid-solution-for-retrofitting/.

[23] Jan Fredrik Hansen, Alf Kåre Ådnanes, and Thor I. Fossen. "Mathematical Modelling of Diesel-Electric Propulsion Systems for Marine Vessels." In: *Mathematical and Computer Modelling of Dynamical Systems* 7.3 (2001), pp. 323–355.

[24] Ralf Hesse, Dirk Turschner, and Hans Peter Beck. "Micro grid stabilization using the virtual synchronous machine (VISMA)." In: *Renewable Energy and Power Quality Journal* 1.7 (2009), pp. 676–681.

[25] Yuko Hirase et al. "A grid-connected inverter with virtual synchronous generator model of algebraic type." In: *Electrical Engineering in Japan (English translation of Denki Gakkai Ronbunshi)* 184.4 (2013), pp. 10–21.

[26] Vikram Kaura and Vladimir Blasko. "Operation of a phase locked loop system under distorted utility conditions." In: *IEEE Transactions on Industry Applications* 33.1 (1997), pp. 58–63.

[27] Helge Kolstad. *Control of an adjustable speed hydro utilizing field programmable devices*. Trondheim, 2002.

[28] Paul Krause et al., eds. *Analysis of Electric Machinery and Drive Systems*. Hoboken, NJ, USA: John Wiley & Sons, Inc., June 2013. URL: http://doi.wiley.com/10.1002/9781118524336.

[29] Prabha Kundur et al. "Definition and classification of power system stability." In: *IEEE Transactions on Power Systems* 19.3 (2004), pp. 1387–1401.

[30] *Leading the charge - DNV*. URL: https://www.dnv.com/expert-story/maritime-impact/leading-the-charge.html.

[31] Janie Ling-Chin and Anthony P. Roskilly. "Investigating the implications of a new-build hybrid power system for Roll-on/Roll-off cargo ships from a sustainability perspective – A life cycle assessment case study." In: *Applied Energy* 181 (2016), pp. 416–434. URL: http://dx.doi.org/10.1016/j.apenergy.2016.08.065.

[32] J. A.Peças Lopes, C. L. Moreira, and A. G. Madureira. "Defining control strategies for analysing microgrids islanded operation." In: *2005 IEEE Russia Power Tech, PowerTech* 21.2 (2005), pp. 916–924.

[33] Jan Machowski, Janusz W Bialek, and James R Bumby. *POWER SYSTEM*.

[34] Olve Mo, Salvatore Darco, and Jon Are Suul. "Evaluation of Virtual Synchronous Machines with Dynamic or Quasi-Stationary Machine Models." In: *IEEE Transactions on Industrial Electronics* 64.7 (2017), pp. 5952–5962.

[35] Muhammad Umair Mutarraf et al. "Energy Storage Systems for Shipboard Microgrids-A Review." In: (). URL: www.mdpi.com/journal/energies.

[36] Jon O'Sullivan et al. "Studying the maximum instantaneous non-synchronous generation in an Island system-frequency stability challenges in Ireland." In: *IEEE Transactions on Power Systems* 29.6 (2014), pp. 2943–2951.

[37] Nagaraju Pogaku, Milan Prodanović, and Timothy C. Green. "Modeling, analysis and testing of autonomous operation of an inverter-based microgrid." In: *IEEE Transactions on Power Electronics* 22.2 (Mar. 2007), pp. 613–625.

[38] Kundur Prabha. *[Prabha Kundur] Power System Stability and Control.Pdf*. 1994.

[39] Three-phase Pwm et al. "New Simple Active Damping of Resonance." In: *2005 IEEE International Conference on Industrial Technology* (2005), pp. 861–865.

[40] D. Radan. *Integrated Control of Marine Electrical Power Systems*. 2008, p. 231. URL: https://pdfs.semanticscholar.org/b770/71c49cf7425e23a386e5d90b779cd21e242e.pdf%0Ahttp://folk.ntnu.no/assor/PhDThesis/Phd_Radan_NTNU.pdf.

[41] Oscar Saborío-Romano. "Small-signal modelling and stability anal-ysis of a traditional generation unit and a virtual synchronous machine in grid-connected operation European Wind Energy Master-EWEM-Electric Power Systems Track." In: (2015).

[42] Ken Ichi Sakimoto, Kazushige Sugimoto, and Yuji Shindo. "Low voltage ride through capability of a grid connected inverter based on the virtual synchronous genera-

tor." In: *Proceedings of the International Conference on Power Electronics and Drive Systems* (2013), pp. 1066–1071.

[43] P. W; M. Pai Sauer. ""Power system dynamics and stability," Urbana, vol. 51," in: (1997), pp. 34 –361.

[44] Espen Skjong et al. "Past, present, and future challenges of the marine vessel's electrical power system." In: *IEEE Transactions on Transportation Electrification* 2.4 (2016), pp. 522–537.

[45] Asgeir J. Sorensen et al. "Toward Safer, Smarter, and Greener Ships: Using Hybrid Marine Power Plants." In: *IEEE Electrification Magazine* 5.3 (2017), pp. 68–73.

[46] Pieter Tielens and Dirk Van Hertem. "The relevance of inertia in power systems." In: *Renewable and Sustainable Energy Reviews* 55.2016 (2016), pp. 999–1009. URL: http://dx.doi.org/10.1016/j.rser.2015.11.016.

[47] Tine L. Vandoorn et al. "Active load control in islanded microgrids based on the grid voltage." In: *IEEE Transactions on Smart Grid* 2.1 (2011), pp. 139–151.

[48] By Andrea Vicenzutti et al. "Controls in Modern All-Electrical Ships." In: (2015), pp. 49–65.

[49] K. Visscher and S. W.H. De Haan. "Virtual synchronous machines (VSG'S) for frequency stabilisation in future grids with a significant share of decentralized generation." In: *IET Seminar Digest* 2008.12380 (2008), pp. 23–24.

[50] Heng Wu et al. "Small-Signal Modeling and Parameters Design for Virtual Synchronous Generators." In: *IEEE Transactions on Industrial Electronics* 63.7 (2016), pp. 4292–4303.

[51] Mengran Yu et al. "Investigations of the Constraints relating to Penetration of Non-Synchronous Generation (NSG) in Future Power Systems." In: *2015 Protection, Automation and Control (PAC) World Conference* August (2015), pp. 29–44.

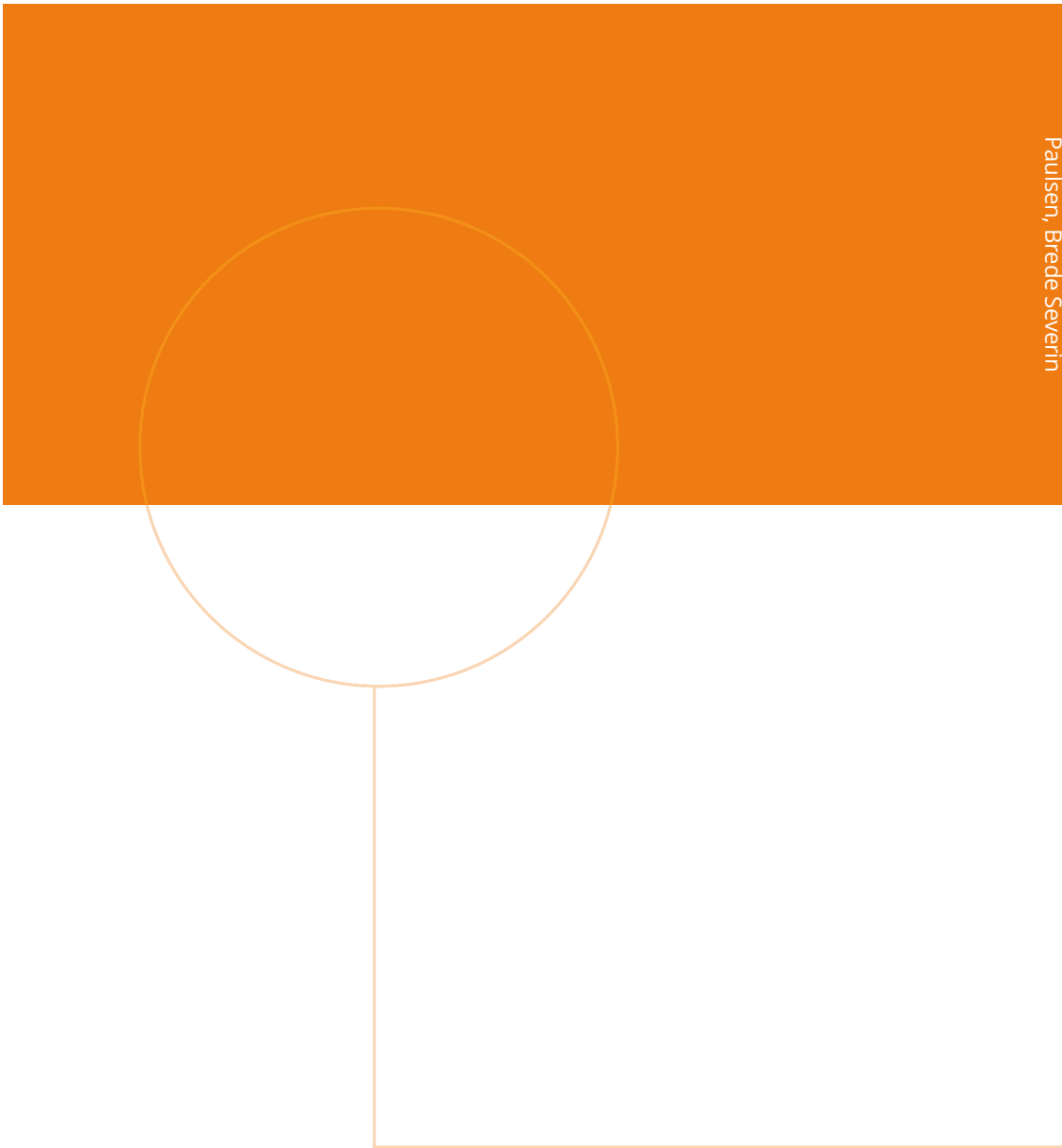

Paulsen, Brede Severin

NTNU
Norwegian University of
Science and Technology